



University  
of Glasgow

Heath, Robert M. (2015) *Nano-optical studies of superconducting nanowire devices for single-photon detection*. PhD thesis.

<http://theses.gla.ac.uk/6132/>

Copyright and moral rights for this thesis are retained by the author

A copy can be downloaded for personal non-commercial research or study, without prior permission or charge

This thesis cannot be reproduced or quoted extensively from without first obtaining permission in writing from the Author

The content must not be changed in any way or sold commercially in any format or medium without the formal permission of the Author

When referring to this work, full bibliographic details including the author, title, awarding institution and date of the thesis must be given



University  
of Glasgow

Nano-optical studies of  
superconducting nanowire devices  
for single-photon detection

Robert M. Heath

*A thesis presented for the degree of*  
Doctor of Philosophy

School of Engineering  
University of Glasgow  
Scotland  
February 2015

# Abstract

Superconducting nanowire single photon detectors (SNSPDs) are a rapidly maturing detector technology that offer superior performance relative to competing infrared photon counting technologies. The original experimental work presented here explores three novel methods of improving and analysing detector characteristics, employing low-temperature piezoelectric motors at temperatures below 4 K in a closed-cycle cryostat.

Utilizing the low-temperature piezoelectric nanopositioners in tandem with a miniature confocal microscope, this work specifically shows a spatially-separable parallel-wire SNSPDs demonstrating one- and two-pixel photon discrimination, with the detector responding more quickly when triggering two pixels. The work demonstrates nanoantenna-coupled SNSPDs, which are simulated, designed, and tested using the same nano-optical setup. In these an increased local absorption into the nanowire is seen at the antennas' resonant wavelengths, enhancing the efficiency of the detector by up to 130 %. Finally, a modified optical setup using a distributed Bragg reflector (DBR) fibre in place of the microscope to form a tunable cavity around two configurations of SNSPD is demonstrated, improving absorption of the incident light into the nanowire across the whole active area. For these, enhancement in the system detection efficiency of up to 40 % is seen.

# Contents

<b>Abstract</b>	<b>1</b>
<b>List of Tables</b>	<b>5</b>
<b>List of Figures</b>	<b>8</b>
<b>Acknowledgements</b>	<b>9</b>
<b>Author's Declaration</b>	<b>11</b>
<b>Definitions &amp; Abbreviations</b>	<b>12</b>
<b>1 Introduction</b>	<b>17</b>
1.1 Thesis outline . . . . .	18
<b>2 Background review</b>	<b>20</b>
2.1 Overview of photon counting technologies . . . . .	20
2.1.1 Photomultiplier tubes . . . . .	20
2.1.2 Single photon avalanche diodes . . . . .	22
2.1.3 Superconducting single photon detectors . . . . .	22
2.2 SNSPD background and device evolution . . . . .	26
2.3 Reaching cryogenic temperatures . . . . .	30
2.3.1 Helium dewar . . . . .	30
2.3.2 Closed-cycle refrigeration . . . . .	30
2.4 Vacuum technology . . . . .	34
2.4.1 Flow regimes . . . . .	34
2.4.2 Conductance . . . . .	35
2.4.3 Pump selection . . . . .	35
2.5 Plasmonics and nanoantennas . . . . .	36
2.5.1 Simulation of plasmonic behaviour . . . . .	37
2.6 Optical cavities . . . . .	39
<b>3 Experimental and analytical methods</b>	<b>42</b>

3.1	Parallel-wire SNSPD fabrication . . . . .	43
3.2	Nanoantenna-coupled SNSPD fabrication . . . . .	45
3.2.1	Gold lift-off method . . . . .	46
3.2.2	Silver etch method . . . . .	49
3.3	SNSPD-on-DBR fabrication process . . . . .	49
3.4	Closed-cycle cryostat layout and operation . . . . .	52
3.5	Screening detectors for functionality . . . . .	54
3.6	Basic electrical characterisation . . . . .	55
3.6.1	Noise analysis . . . . .	56
3.7	Parallel wire device operation . . . . .	57
3.8	Wire bonding and sample mounts . . . . .	57
3.8.1	Optical coherence tomography . . . . .	59
3.9	Kinetic inductance . . . . .	60
3.10	Detection efficiency . . . . .	61
3.10.1	Pulsed laser system detection efficiency . . . . .	62
3.10.2	Continuous-wave system detection efficiency . . . . .	63
3.11	Detector timing jitter . . . . .	64
3.12	Miniature confocal microscope configuration . . . . .	66
3.12.1	Spot-response convolution . . . . .	68
3.12.2	Minimising vibration . . . . .	68
3.12.3	Minimizing effect of thermal oscillations . . . . .	70
3.13	Tunable cavity configuration . . . . .	72
3.13.1	Distributed Bragg reflector design . . . . .	72
3.13.2	Cavity lengths from fringe spacing . . . . .	74
3.14	Wavelength scanning tests . . . . .	77
3.15	Programming and automation . . . . .	79
<b>4</b>	<b>Spatially-resolvable parallel-wire SNSPDs</b>	<b>81</b>
4.1	Multi-pixel triggering theory . . . . .	81
4.1.1	Markovian approximation . . . . .	82
4.1.2	Bayesian model . . . . .	85
4.2	Device layout & operation . . . . .	87
4.3	Results . . . . .	91
4.4	Conclusion . . . . .	94
<b>5</b>	<b>Nanoantenna-coupled SNSPDs</b>	<b>96</b>
5.1	Introduction . . . . .	96
5.2	Device layout & simulation . . . . .	97
5.3	Results . . . . .	103
5.4	Conclusion . . . . .	105

---

<b>6</b>	<b>Tunable-cavity embedded SNSPDs</b>	<b>106</b>
6.1	Introduction . . . . .	106
6.2	Device layout & operation . . . . .	107
6.2.1	Configuration I: gold reflector SNSPD . . . . .	107
6.2.2	Configuration II: DBR SNSPD . . . . .	109
6.3	Simulation . . . . .	109
6.4	Results . . . . .	113
6.4.1	Configuration I results . . . . .	113
6.4.2	Configuration II results . . . . .	114
6.5	Conclusion . . . . .	117
<b>7</b>	<b>Conclusions</b>	<b>119</b>
7.1	Summary and discussion of results . . . . .	119
7.1.1	Spatially-resolvable parallel-wire SNSPDs . . . . .	119
7.1.2	Nanoantenna-coupled SNSPDs . . . . .	120
7.1.3	Tunable-cavity embedded SNSPDs . . . . .	121
7.2	Parallel developments in group . . . . .	121
7.3	Outlook . . . . .	121
<b>A</b>	<b>List of Publications</b>	<b>123</b>
	<b>List of References</b>	<b>123</b>

# List of Tables

1	Author's contributions to the work . . . . .	11
2.1	Summary of single photon detector technologies' figures of note . . . . .	25
2.2	Flow regimes by Knudsen number . . . . .	35
6.1	Reported complex refractive indexes for NbTiN . . . . .	109

# List of Figures

1.1	Diagram of the electromagnetic spectrum . . . . .	18
2.1	Diagram illustrating the metrics for comparing photon detection technologies . . . . .	21
2.2	Diagram of the principles of superconductivity . . . . .	23
2.3	Diagram of nature of Cooper pairs . . . . .	24
2.4	Diagram of the SNSPD triggering method . . . . .	26
2.5	An SEM of a meander-type geometry SNSPD and a diagram of a meander-type geometry in a cavity . . . . .	27
2.6	A map across two devices, one with constriction . . . . .	28
2.7	SEM and circuit diagram of Divoichy’s photon-number-resolving parallel wire scheme . . . . .	29
2.8	SEM of Miki’s 64-pixel SNSPD array . . . . .	29
2.9	Operation of an ideal Stirling cycle . . . . .	31
2.10	Operation of the GM cycle . . . . .	32
2.11	Layout of a GM -cycle linear pulse tube . . . . .	33
2.12	Diagram of geometry and timing response of plasmon-enhanced single photon detector . . . . .	37
2.13	FDTD simulation results for comparison with literature . . . . .	38
2.14	Layout and behaviour of a half-cavity design . . . . .	39
3.1	Photograph of ‘Kelvinator’ testing setup . . . . .	42
3.2	SEM image of a completed parallel-wire SNSPD . . . . .	43
3.3	Process used at University of Cambridge to fabricate SNSPDs . . . . .	44
3.4	SEM image of a completed nanoantenna . . . . .	46
3.5	Diagram of initial process used at NICT to fabricate nanoantenna-coupled SNSPDs . . . . .	47
3.6	Diagram of final process used at NICT to fabricate nanoantenna-coupled SNSPDs . . . . .	48
3.7	scanning electron microscope (SEM) image of a completed SNSPD on a GaAs/Al <sub>0.8</sub> Ga <sub>0.2</sub> As DBR . . . . .	50

3.8	Process used to fabricate SNSPDs on a DBR substrate . . . . .	51
3.9	Diagram of the setup of the cryostat for nano-optical testing . . . . .	53
3.10	Diagram of the setup for an I-V measurement . . . . .	55
3.11	Graphs of typical output from the I-V measurement program . . . . .	56
3.12	Diagram of parallel-wire SNSPD device cascade switching principle . . . . .	57
3.13	Diagram of the standard detector sample mount layout . . . . .	58
3.14	Graph of typical output of the OCT setup. . . . .	59
3.15	A diagram of the circuit used to measure the kinetic inductance and a graph of typical output . . . . .	60
3.16	Diagram of the setup for a detection efficiency measurement . . . . .	61
3.17	Typical output from the pulsed-source detection efficiency fitting program . . . . .	63
3.18	Typical output from the CW detection efficiency fitting program . . . . .	64
3.19	Diagram of the setup for taking a detector jitter measurement . . . . .	65
3.20	Diagram of the confocal microscope configuration . . . . .	66
3.21	Checkerboard pattern imaged by miniature confocal microscope . . . . .	67
3.22	Convolution of square and Gaussian . . . . .	68
3.23	Diagram of device response when system vibrating . . . . .	69
3.24	Photoresponse of nanoantenna-coupled SNSPD when vibrating . . . . .	70
3.25	Effect of thermal oscillations on SNSPD count rate . . . . .	71
3.26	Photograph of DBR fibre and fibre mount . . . . .	71
3.27	Schematic of attaching the DBR layers to the fibre ferrule . . . . .	72
3.28	Dektak profile of microlens substrate . . . . .	73
3.29	Diagram of the two optical cavities formed with Configurations I and II . . . . .	73
3.30	Comparison of simulated and experimentally-observed cavity behaviour . . . . .	76
3.31	Graphs depicting the agreement between OCT and fringe spacing calculation. . . . .	77
3.32	Diagram of wavelength scanning test setup . . . . .	78
3.33	Graph of typical power profile of wavelength scanning system . . . . .	78
3.34	Example of custom convolution software written for analysing output . . . . .	80
4.1	Comparison of Markovian two-pixel triggering model with real data . . . . .	84
4.2	Comparison of Bayesian two-pixel triggering model with real data . . . . .	88
4.3	SEM image of the spatially-separable parallel-wire SNSPD . . . . .	89
4.4	Maps of the photoresponse with position of spatially-separable parallel-wire SNSPDs in two bias regimes. . . . .	90
4.5	Graph of the count rate as a function of photon flux entering the system when illuminating one- and two-pixels at fixed bias current . . . . .	91
4.6	The photon arrival time profiles when illuminating one or two elements of a multi-pixel SNSPD . . . . .	93

---

5.1	Schematic of the layout of the nanoantenna device . . . . .	97
5.2	SEM and simulation of the nanoantenna. . . . .	98
5.3	Simulation results of nanoantenna behaviour with wavelength and misalignment . . . . .	100
5.4	Graph of system detection efficiency of two nanoantennas as wavelength sweeps resonance . . . . .	102
5.5	Spatial maps of the photoresponse when illuminating a nanoantenna . .	104
6.1	Diagram of the two optical cavities formed with Configurations I and II	107
6.2	Cavity behaviour with increasing air gap length . . . . .	108
6.3	Simulation of the absorbed power in two optical cavities with and without DBR fibre . . . . .	110
6.4	Simulation of DBR behaviour with varying refractive indices and number of bilayers . . . . .	111
6.5	Room temperature reflectivity spectra of the DBR . . . . .	112
6.6	Tuning NICT back-side-coupled SNSPD cavity: simulation and experimental result . . . . .	114
6.7	Graphs of SDE tuning range of Configuration I and comparison with bare fibre . . . . .	115
6.8	Tuning front-side-coupled DBR SNSPD cavity: simulation and experimental result . . . . .	116
6.9	Graphs of SDE tuning range for Configuration II and comparison with bare fibre . . . . .	117

# Acknowledgements

I would like to thank Professor Robert Hadfield, my supervisor, for offering me the opportunity to perform the research contained herein under his careful guidance and assistance. I would like to thank the University of Glasgow for supporting my supervisor and the Quantum Sensors Group in our move here, a move which though unexpected has proven indubitably worthwhile. I would also like to thank Heriot-Watt University, where I first began my Ph.D. studies in Autumn 2010, and the Engineering and Physical Sciences Research Council for the funding that has supported me throughout my work.

I would like to thank Dr Mike Tanner, who was easily the researcher with whom I had the most daily interaction. Without his laboratory expertise and patience I would still be reading equipment manuals and trying to work out why my experiment wasn't working. His friendship enriched my time as a postgraduate student both during the long hours in the lab and socially. I would like to thank Dr Alessandro Casaburi for his limitless help with my understanding of the subtleties of superconductivity, and willingness to help proof-read journal papers. I would also like to thank Dr Chandra Mouli Natarajan for his knowledgeable aid both early on while I was familiarising myself with the group and laboratory, and more recently after returning to the group from the USA. Finally I would like to thank Robert Kirkwood for his friendship and his assistance with clean room activities, especially with patterning the detectors on distributed Bragg reflectors. All are great researchers and friends.

I would like to thank our group's collaborators both locally and further afield: Dr Tim Drysdale, my secondary supervisor, for his help with finite-difference time-domain simulations, especially with tracking down mysterious polarization behaviour in simulations of nanowires; Dr Zoe Barber and Dr Lara San Emeterio Alvarez at the University of Cambridge, for providing parallel-wire devices that form the basis of my first publication; Mark Webster at the University of Leeds for his assistance and expertise implementing Bayesian statistics; Professor Stefan Maier and Dr Vincenzo Giannini at Imperial College London for their help with initial simulations of nanoantennas; and Dr Shigehito Miki and the National Institute of Information and Communications Technology, Japan, for offering me a Research Internship Fellowship, looking after me

during my visit, and providing several devices used in this work and related publications. Thank you all.

I would like to thank my parents and family for their enthusiasm and support during my time in Scotland: despite living far away, they take every opportunity to visit. Aside from the obvious reasons, I couldn't have achieved this doctorate without them behind me.

Finally, for putting her through the trauma of four years of postgraduate research by proxy, I would like to dedicate half of this thesis to my partner and best friend Amber. The other half is dedicated to our beloved daughter Elspeth. Without Amber's love and support, there might not be a thesis; without Elspeth, it might have been submitted months ago.

# Author's Declaration

I declare that, except where explicit reference is made to the contribution of others, this thesis is the result of my own work and has not been submitted for any other degree at the University of Glasgow or any other institution.

For the avoidance of ambiguity, a full breakdown of my personal contributions is stated in table 1.

Chapter	Personal Contribution
1	Text and graphics
2	Finite difference time domain (FDTD) simulation; text and graphics except where stated
3	Nanoantenna design; cryostat vibration damping; continuous-wave system detection efficiency (SDE) fitting program; confocal microscope resolution tests; spot-response convolution program; minimising thermal oscillations; DBR-coupled fibre; wavelength scanning program and equipment; power profile of wavelength scanning system; assorted Python programming; text and graphics except where stated
4	Markovian approximation; contributed to development of Bayesian model; experimental work; fitting and analysis; conclusion; text and graphics except where stated
5	Detector design; FDTD simulation; experimental system development; experimental work; analysis; conclusion; text and graphics except where stated
6	DBR-coupled fibre; experimental system development; experimental work; matching simulation with result; analysis; conclusion; text and graphics except where stated
7	Text

Table 1: Author's contributions to the work

# Definitions & Abbreviations

## Acronyms

<b>BCS</b>	Bardeen, Cooper, and Schrieffer
<b>cps</b>	counts per second
<b>CW</b>	continuous wave
<b>DBR</b>	distributed Bragg reflector
<b>DC</b>	direct current
<b>ECR</b>	electron cyclotron resonance
<b>FDTD</b>	finite difference time domain
<b>FFT</b>	fast Fourier transform
<b>FWHM</b>	full-width at half-maximum
<b>GM</b>	Gifford-McMahon
<b>GPIB</b>	general purpose interface bus
<b>HSQ</b>	hydrogen silsesquioxane
<b>IPA</b>	isopropyl alcohol
<b>IR</b>	infra-red
<b>LIDAR</b>	light detection and ranging
<b>LSP</b>	localised surface plasmon
<b>MBE</b>	molecular beam epitaxy
<b>MCP</b>	microchannel plate
<b>MSM</b>	metal-semiconductor-metal
<b>NA</b>	numerical aperture

<b>OCT</b>	optical coherence tomography
<b>OFHC</b>	oxygen-free, high thermal conductivity
<b>PMT</b>	photomultiplier tube
<b>PNR</b>	photon number resolution
<b>QE</b>	quantum efficiency
<b>QKD</b>	quantum key distribution
<b>RF</b>	radio frequency
<b>RIE</b>	reactive ion etch
<b>rpm</b>	revolutions per minute
<b>SDE</b>	system detection efficiency
<b>SEM</b>	scanning electron microscope
<b>SFQ</b>	single flux quantum
<b>SMF</b>	single-mode fibre
<b>SNAP</b>	superconducting nanowire avalanche photodetector
<b>SNR</b>	signal-to-noise ratio
<b>SNSPD</b>	superconducting nanowire single photon detector
<b>SPAD</b>	single photon avalanche diode
<b>SPP</b>	surface plasmon polariton
<b>SQUID</b>	superconducting quantum interference device
<b>SSLD</b>	superconducting strip-line detector
<b>STJ</b>	superconducting tunnel junction
<b>TCSPC</b>	time-correlated single photon counting
<b>TES</b>	transition-edge sensor
<b>UV</b>	ultraviolet
<b>VNA</b>	vector network analyser

### Greek symbols

$\delta_{a,b}$	Kronecker delta
$\Delta$	superconducting energy gap

$\eta$	efficiency
$\eta_{absorption}$	absorption efficiency
$\eta_{coupling}$	coupling efficiency
$\eta_{triggering}$	triggering efficiency
$\gamma$	dark event probability
$\kappa$	extinction coefficient
$\lambda_0$	wavelength in vacuum
$\lambda$	wavelength
$\mu$	mean photon number per pulse
$\omega$	angular frequency
$\tau$	detector reset time
$\xi$	superconducting coherence length

### Roman symbols

$b$	number of pixels required to trigger parallel-wire detector
$C$	kinetic inductance fitting parameter
$c$	speed of light
$D$	dark count rate
$d$	total number of arming events
$d_{flow}$	flow channel diameter
$d_m$	molecular diameter
$E$	energy
$\mathcal{E}$	stored energy
$f_0$	resonant frequency
$g$	total number of dark events
$h$	Planck constant
$\hbar$	reduced Planck constant
$I$	current
$I_B$	bias current

---

$I_C$	critical current
$k_B$	Boltzmann constant
$K_n$	Knudsen number
$L$	length
$L_K$	kinetic inductance
$L_{K,0}$	initial kinetic inductance
$\bar{L}$	mean free path
$L_{cond}$	pipng conductance
$L_t$	thickness
$N$	number
$n$	refractive index
$n_{par}$	number of parallel pixels in parallel-wire detector
$P$	dissipated power
$p$	pressure
$\mathbb{P}$	probability of trigger event occurring
$P_H$	high pressure
$P_L$	low pressure
$\mathbb{P}_m$	single photon transition matrix
$Q$	quality factor
$Q_E$	absorbed heat
$Q_I$	released heat
$q_{pV}$	gas throughput
$Q_{RT}$	stored heat
$\mathcal{R}$	reflectance
$r$	radius
$R^2$	coefficient of determination
$R_{detected}$	detected photon flux
$R_{input}$	input photon flux

$R_{series}$	series resistance
$R_{shunt}$	shunt resistor
$S$	initial state of parallel-wire detector
$T$	temperature
$t$	time
$T_{boil}$	liquid-gas transition temperature
$T_C$	superconducting transition temperature
$T_E$	final temperature of heat cycle
$T_I$	initial temperature of heat cycle
$t_{meas}$	measurement time
$t_{osc}$	thermal oscillation time
$V$	voltage
$v_f$	Fermi velocity
$V_{out}$	output voltage
$V_{vol}$	volume
$X_E$	hot heat exchanger
$X_I$	cold heat exchanger

# Chapter 1

## Introduction

In 1905, Einstein applied the quantisation of energy to light[1] and the notion of light as being corporeal and discrete was formally codified. Each individual packet of light, called a photon, is intrinsically characterised by a certain amount of energy  $E$ , determined by its wavelength  $\lambda$ , Planck's constant  $h$ , and the speed of light  $c$ :  $E = hc/\lambda$ .

Humans, like many living organisms on Earth, come equipped as standard with photon detectors. In what we perceive as the visible range of the electromagnetic spectrum, the rods of the eye afford excellent photon sensitivity, responding to the simultaneous arrival of single-digit numbers of 510 nm (green) photons[2]. These photons have an individual energy of just  $3.89 \times 10^{-19}$  J. We are also able to macroscopically perceive ultraviolet (UV), visible, and infra-red (IR) photon absorption into our skin, as an increase in temperature[3].

The realisation of non-biological photon sensors has been fundamental in the history of recent human technological progress. Photons are a ubiquitous resource for understanding the cosmos[4, 5]. From agriculture[6] and medical imaging[7] to high-technology quantum information processing[8], they are a technologist's best friend. Underpinning this use is being able to detect photons in a quantifiable way. There are many approaches to this, because photons exist in a broad wavelength space, as shown in figure 1.1, and the detection technology used is highly dependent on this characteristic. This work looks specifically at single photon detection across the fibre-optic telecommunications bands, specifically from 1340 nm to 1650 nm.

Superconducting nanowire single photon detectors (SNSPDs) are the fastest single-photon-detecting and single-photon-counting technology available. They have been demonstrated with 93% detection efficiency[9] and 18 ps timing jitter[10–12] and have been used widely in experiments from cancer therapy and light detection and ranging (LIDAR) to large-scale quantum key distribution (QKD)[13–16].

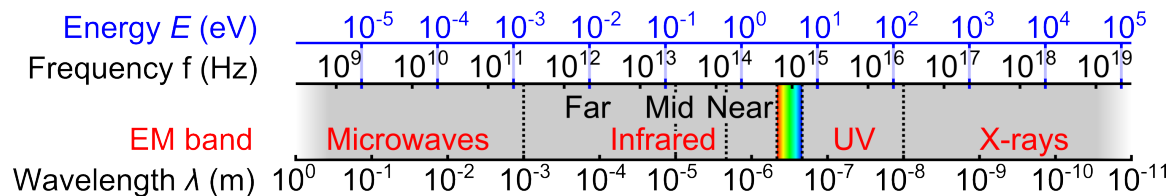


Figure 1.1: Diagram of the electromagnetic spectrum. Visible light stretches from 400 nm to 700 nm, shown as a band of colour, and is bound by less-energetic IR and more-energetic UV. IR is split into three sections: near, mid, and far. The energy of a photon in the near-IR is around 1 eV, which corresponds to  $1.6 \times 10^{-19}$  J. At higher wavelengths there are microwaves, then radio waves and long-wave. At lower wavelengths there are X-rays and then gamma rays.

In 2010 I began postgraduate study at Heriot-Watt University, Edinburgh, initially studying exciting next-generation SNSPD designs with a miniature confocal microscope mounted in a Gifford-McMahon (GM) cryostat[17]. During the course of my work, this nano-optical system was built upon and adapted. The first modification was for use in a low-vibration pulse-tube cryostat[18]. I then sourced and constructed and automated a system of three continuous wave (CW) lasers with polarisation control and a 340 nm tuning range around the IR telecommunications band for use with the nano-optical system. In 2011 I spent 3 months at the National Institute of Information and Communication Technology (NICT) in Japan designing and fabricating nanoantenna-coupled SNSPDs[19]. Following this the nano-optical system was adapted to allow mounting of a fibre with a distributed Bragg reflector (DBR)-coated end, to allow the creation of a tunable cavity[20]. In 2013 the research group was relocated to the University of Glasgow, which necessitated disassembly and reassembly of the full experimental system: happily, this went to plan, and within a few months of the move the system was functioning again. Further to experimental work, I have performed simulations and analysis where appropriate of the results obtained during the last four years.

## 1.1 Thesis outline

This thesis presents studies using a low-temperature, vibration-damped nano-optical system. This is employed to analyse the behaviour of three different types of superconducting nanowires: spatially-separate parallel-wire SNSPDs[18], nanoantenna-coupled SNSPDs[19], and meander-type SNSPDs in varying types of tunable cavity[20]. Chapter 2 contains information that will help the reader in understanding why the work contained in this thesis is important, and outlines the current state of the field. It offers a background of photon detection technologies, focusing in on superconductivity and SNSPDs. There is also an explanation of how to reach low temperatures and high vacuum.

Much of the work over the last four years was performed designing, building, and programming the experimental systems employed: for this reason, Chapter 3 outlines in rigorous detail the methods behind the work. Each of the detectors used came from separate collaborations: their varied fabrication processes are covered in detail. Experimental procedures are discussed, as is the closed-cycle cryostat and nano-optics. A description of the tunable cavity is also within this section.

The next chapters outline the results of the work. Chapter 4 looks specifically at the behaviour of spatially-separate parallel-wire SNSPDs, and using them to discriminate between one- and multi-pixel triggering regimes. Chapter 5 is concerned with observing enhanced photodetection in telecoms-wavelength-resonant nanoantenna-coupled SNSPDs. Chapter 6 discusses the behaviour of multiple SNSPDs in the tunable cavity. Finally, the conclusions of the work are presented in Chapter 7, alongside an outline of the shortcomings and future direction the work might be taken.

# Chapter 2

## Background review

This chapter begins presenting the background behind single photon detection technologies. This is followed by a more in-depth look at the superconducting nanowire single photon detector (SNSPD). Methods of reaching the low temperatures required to run SNSPDs are then discussed. Sections on plasmonics and nanoantennas, vacuum technology, and optical cavities are then presented.

### 2.1 Overview of photon counting technologies

There are numerous photon detection technologies that allow single-photon sensitivity[21]. Established detectors like photomultiplier tubes (PMTs) and single photon avalanche diodes (SPADs) sit alongside emerging detector technologies like SNSPDs. This section of the thesis will describe these competing technologies, and look at their relative strengths and weaknesses.

When comparing photon detection technologies there are several important metrics: the wavelength range over which the detector can function (the spectral range), the reset time of the detector (dead time), the number of false counts per second (dark count rate), the ratio of detected photons to input photons (detection efficiency), whether the detector can resolve multiple incident photons (photon number resolution) and the distribution of signal arrival times after the photon has struck the detector (timing jitter). These are visualised in figure 2.1.

#### 2.1.1 Photomultiplier tubes

First demonstrated in 1935[22, 23], the PMT combines the photoelectric effect, where electrons that absorb a photon with energy higher than their work function are ejected from a material, with secondary emission, where absorption of one energetic particle

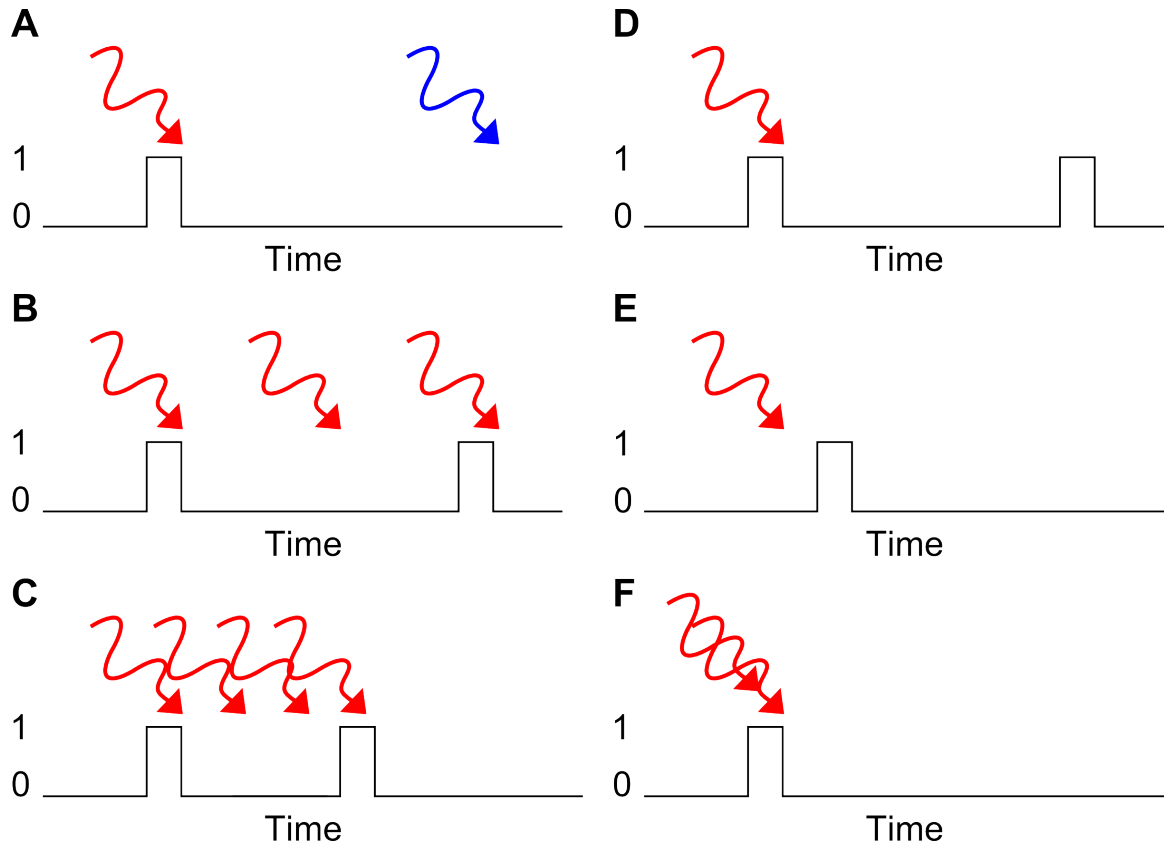


Figure 2.1: Diagram illustrating the metrics for comparing photon detection technologies. Photon arrival events are depicted pictorially, while the detector response is shown as a black line reporting a ‘0’ or ‘1’. **A** shows spectral range: photons outside of the spectral range, which are of the wrong colour, do not register on the detector. **B** shows detection efficiency: a photon arrival does not result in a pulse on the detector. **C** shows detector dead time: the detector is unable to respond to photon arrivals immediately after triggering. **D** shows dark count rate: the detector registers a pulse where there is no photon. **E** shows arrival time: the detector registers the detection a short while after the photon arrives. The uncertainty in this is the timing jitter. **F** shows photon number resolution: two photons arrive at the same time, but the detector only registers one.

may trigger release of multiple others. PMTs are now widely available and used in experiment: 13,000 PMTs were used in the Super Kamiokande observatory[24] detecting Čerenkov radiation from solar neutrinos. PMTs have large spectral ranges, but low efficiency[25].

The operating principle behind PMTs is relatively simple to describe. If the incident photon’s energy is greater than the work function of the material the photon strikes, the material releases photoelectrons. These electrons are accelerated by potentials applied between alternating cathodes, releasing orders of magnitude more electrons at each stage, and thus amplifying the signal. The end pulse of electrons is macroscopically detectable.

Microchannel plate (MCP) PMTs have lower jitter values[26] at around 30 ps full-width at half-maximum (FWHM) by reducing the effective path length of the system. The

MCPs, secondary multipliers made of millions of glass channels formed into a disc, enhance performance by enabling secondary emission, adding 30 dB to 70 dB of gain depending on the number of stages[27, 28]. Traditionally, PMTs are fragile, require high voltages to run, and are expensive[21].

### 2.1.2 Single photon avalanche diodes

Silicon SPADs were realised in 1980 as a method of using avalanche photodiodes to detect individual photons[29]. By operating the diode in ‘Geiger-mode’, where a bias voltage greater than the diode’s breakdown voltage is applied[30], the diode gives digital pulses when a photon is absorbed. This is caused by the released carriers, amplified by the avalanche, eventually causing the breakdown of the p-n junction, occurring because the device is being operated in an unstable mode[31]. It is then reset by quenching. Si SPADs were improved, and by 1989 were shown with FWHM timing jitter of 20 ps[32]. They have a spectral range of 400 nm to 1000 nm and a peak efficiency of 65 % at 650 nm[31].

At the main optical telecommunications wavelengths (1310 nm and 1550 nm[33]) the band gap of silicon (1.1  $\mu\text{m}$  or 1.11 eV[34]) prevents these Si SPADs from functioning, and thus InGaAs detectors (band gap 1.7  $\mu\text{m}$ ) were developed. SPADs typically have efficiencies of 20 % at 1550 nm. They run at high dark count rates and subsequently work best when used in a gated setup where the detector is armed only for a short period when a photon is likely to arrive[21]. In this mode they still suffer from an effect called afterpulsing, whereby trapped carriers can re-trigger an avalanche, further eroding performance[35].

### 2.1.3 Superconducting single photon detectors

There are several detectors that use superconductivity as the basis for their detection method. Superconducting tunnel junctions (STJs), transition-edge sensors (TESs), and SNSPDs will be described, the latter extensively. A brief overview of superconductivity will be presented first, as this is vital for discussion of detectors based on this phenomenon.

The classical model of resistance in a conductor was that resistance increases proportionally with temperature, which came from the idea that resistance was caused by collisions within the wire which would increase with increased temperature. It was noted as lower temperatures were probed that this model did not fit the observed behaviour: three suggestions for what happened as  $T \rightarrow 0\text{ K}$  were postulated. In 1911[36] after a method of liquefying helium was discovered, it was noted that the resistance

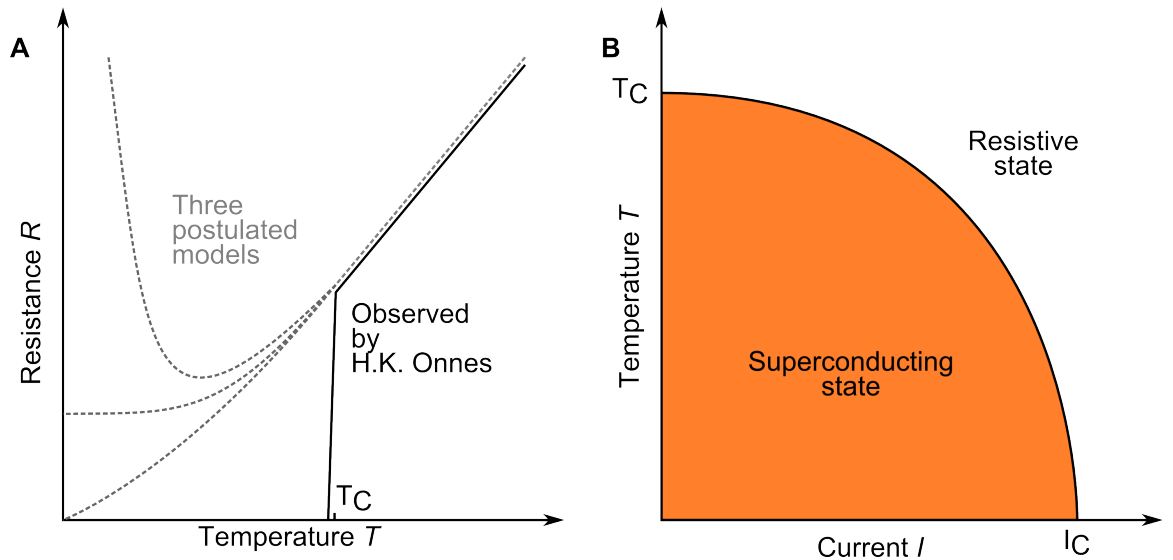


Figure 2.2: Diagram of the principles of superconductivity. Prior to the liquefaction of He, it had been noted that the linear relationship between temperature and resistance did not apply when the temperature became low. Three postulated models of what might happen as  $T \rightarrow 0$  K are shown as grey dashed lines in **A**. Onnes discovered that at a critical temperature  $T_C$  of 4.19 K mercury's resistance dropped to zero, shown as the black line. A superconductor can be forced resistive by heating it above its transition temperature  $T_C$ , or running more than its critical current  $I_C$  through it, creating a boundary range of current and temperatures. This is shown in **B**.

of mercury wire at a non-zero temperature dropped to zero, seen in figure 2.2**A**. This became known as superconductivity.

In 1950, a macroscopic model of superconductivity called Ginzburg-Landau theory[37] was put forward. While this description was sufficient for it to make valid predictions[38], it did not describe the microscopic behaviour in a superconductor. Superconductivity was more fully described phenomenologically by Bardeen, Cooper, and Schrieffer (BCS) theory[39] in 1957. In this description, electrons of opposite spins are bound together in Cooper pairs, so becoming bosons that share a single macroscopic wavefunction[40], which are able to travel freely through the material, and thus the material's resistance drops to  $0 \Omega$ . This is shown in figure 2.3. The length over which electrons form into Cooper pairs is called the superconducting coherence length  $\xi$ . According to BCS theory, this length is described by

$$\xi = \frac{2\hbar v_f}{\pi\Delta}, \quad (2.1)$$

where  $\hbar$  is the reduced Planck constant,  $v_f$  is the Fermi velocity, and  $\Delta$  is the superconducting energy gap. This is the minimum energy required to create a single electron excitation from the ground state, and is a function of temperature[41]. The binding energy of a Cooper pair is  $2\Delta$ . The energy gap at 0 K is

$$\Delta(0) = 1.76k_B T_C \quad (2.2)$$

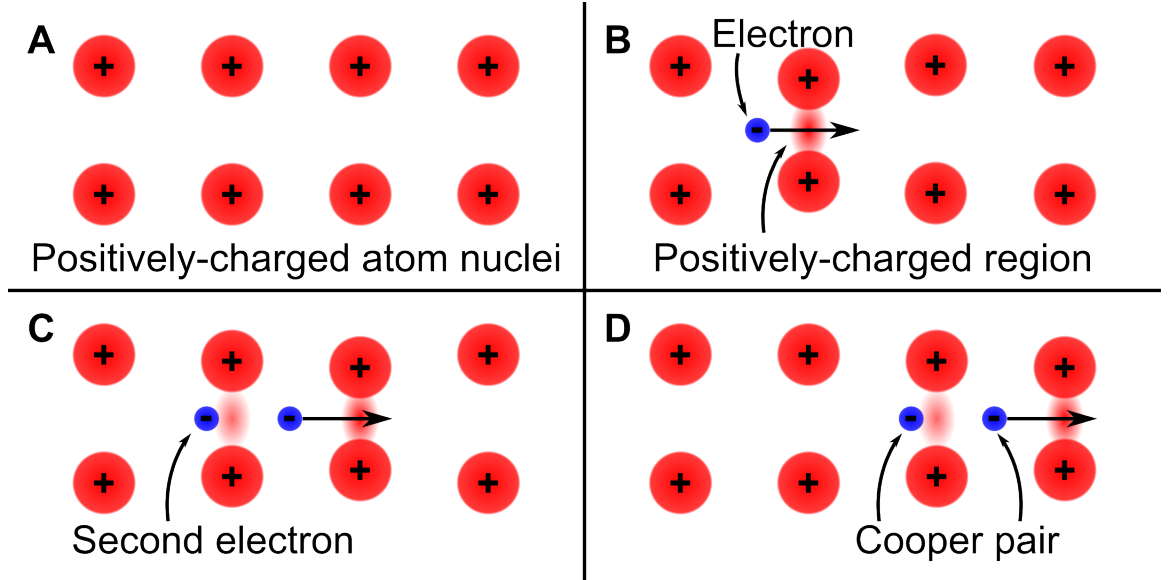


Figure 2.3: Diagram of nature of Cooper pairs. The superconducting material’s lattice of molecules is shown as red circles with a positive electric charge, and because the lattice is below  $T_C$  there are no lattice vibrations (phonons). This is shown in **A**. In **B**, the electrons are shown as blue circles and have a negative electric charge. The electron distorts the lattice by its presence, creating a virtual phonon and an area of net positive charge. In **C**, as the electron travels past, the lattice does not immediately relax back, leaving an area of charge behind it. This draws a second electron into it. In **D** we see that as this continues the effect is to create a pair of electrons, with what appears to be an attractive force between them that overcomes their Coulomb repulsion. Subsequently we see there is no collision with the lattice, and so no resistance. As the second electron pulls the molecules together again, it effectively becomes a new first electron, allowing an electron behind it to pass freely in the same way it did. Subsequently, there is no resistance in the material.

and near the critical temperature  $T \approx T_C$  is

$$\frac{\Delta(T)}{\Delta(0)} = 1.74 \left(1 - \frac{T}{T_C}\right)^{1/2}. \quad (2.3)$$

Subsequently, the energy gap varies continuously from zero at  $T_C$  to  $\Delta(0)$  at  $T = 0$ : so, below  $T_C$  the material is superconducting. A current induced in a perfect superconductor maintained below the transition temperature will persist indefinitely. In addition to the transition temperature, there is a critical current  $I_C$ , above which the material is resistive. These properties are depicted visually in figure 2.2B, and exploited by superconducting single photon detectors.

**Superconducting tunnel junction:** The STJ was one of the first single photon detection technologies based on superconductivity. Initially used to detect X-ray wavelength photons, they were demonstrated detecting optical photons in 1996[42]. The STJ operates using two superconducting films separated by a thin tunnel barrier layer with a thickness of order 1 nm. Applying a bias voltage  $V < 2\Delta/e$  across the su-

perconducting films allows tunnelling of the quasiparticles generated when a photon is absorbed into the top layer through the tunnel barrier, so generating a measurable electric current.

STJs require operating temperatures in the mK range to operate, to avoid thermal tunnelling, and have a FWHM timing jitter of  $10^6$  ps. Though having negligible dark count rates, their count rates are typically  $10^4$  Hz, and their efficiency is low[42].

**Superconducting transition-edge sensors:** A superconducting TES uses the steep temperature-dependence of the resistance of a superconductor on the cusp of the superconducting transition to detect photons[43]. By cooling a thin film of a superconducting material to just below its  $T_c$ , the energy of a photon is able to force the TES resistive. When biasing the device with a voltage, a current pulse is output upon absorption and is detected via a superconducting quantum interference device (SQUID). The TES is a bolometer, and as such the output pulse is proportional to the energy of the photon for a given wavelength[44]. Tungsten-based detectors enclosed in optical cavities have been reported with 95 % efficiency at 1550 nm, with jitter of 100 ns and dead times of 100 ns[21].

**Superconducting nanowire single-photon detectors:** First successfully fabricated by Gol'tsman[45] in 2001, and with a Gaussian response profile and jitter as low as 18 ps FWHM[10, 46], SNSPDs offer efficient detection of photons[9] over a spectral range from ultraviolet (UV) to mid-infra-red (IR)[47, 48]. SNSPDs use both the critical current and temperature of superconducting films to create measurable voltage pulses upon absorption of a photon. Their method of operation is covered in detail in the following section.

For reference, the best figures of note for each technology (spectral range, system detection efficiency (SDE) at telecoms wavelength, dark count rate, timing jitter, and peak count rate) are summarised in table 2.1.

Detector	Spectral range	SDE@1550 nm	Dark count rate	Timing jitter	Count rate
PMT	1.7 $\mu\text{m}$ [49]	2 % [49]	200 kHz [21]	30 ps [26]	10 MHz [21]
SPAD	1.7 $\mu\text{m}$ [50]	40 % [51]	58 kHz [52]	240 ps [52]	1 MHz [52]
STJ	500 nm [30]	-	-	10 $\mu\text{s}$	10 kHz [42]
TES	4 $\mu\text{m}$ [43]	95 % [53]	-	100 ns [54]	1 MHz [55]
SNSPD	5 $\mu\text{m}$ [48]	93 % [9]	variable	18 ps [12]	10 GHz [56]

Table 2.1: Summary of single photon detector technologies' figures of note

## 2.2 SNSPD background and device evolution

In an SNSPD, a thin film of a superconductor is biased just below its critical current (the bias current  $I_B$ ). Photons striking the superconductor deposit their energy  $\hbar\omega$  into the superconductor, creating an area of separated Cooper pairs out of equilibrium, with ‘cold’ Cooper pairs and ‘hot’ quasiparticles. This resistive island forces the bias current  $I_B$  around the still-superconducting regions either side of it, pushing the bias current density there above the critical current density of the film, and so turning the full strip of the film resistive. This results in a perceptible voltage pulse from the detector. This is shown visually in figure 2.4.

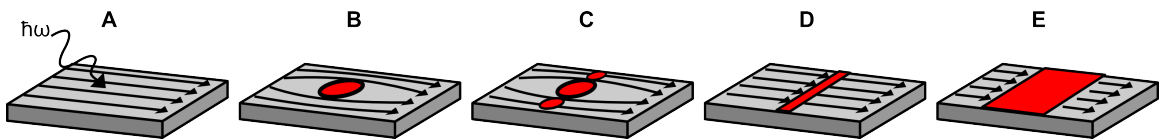


Figure 2.4: Diagram of the SNSPD triggering method, based on an illustration in the initial paper by Gol’tsman[45]. At stage **A**, an incident photon strikes the supercurrent-carrying detector with energy  $\hbar\omega$ . At stage **B**, a hotspot has formed, forcing the supercurrent around the resistive region. At stage **C**, if the bias is sufficiently high, the ‘sidewalks’ of the detector are pushed past their critical current and go resistive, leading to stage **D**, a fully-resistive spot in the detector. Stage **E** is based on an improved model by Yang[57] which shows that the resistive region then spreads along the wire by Joule heating, increasing the measured resistance.

Niobium nitride (NbN) was used by Gol’tsman in the first SNSPDs and has been used by many subsequent groups. NbN must be lattice-matched with the substrate to achieve good homogeneity, important for a good critical current and constriction-free operation. Wires were initially deposited on sapphire, with MgO following[58, 59] with a lower temperature fabrication technique. Subsequently, gallium arsenide[60] and quartz[61] have been successfully demonstrated as substrates. Work by the Quantum Sensors group has also demonstrated wires on lithium niobate[62]. Niobium titanium nitride (NbTiN) wires have been patterned on silicon and silicon oxide[63, 64] as well: this alloy, in roughly a 7:3 ratio of Nb:Ti, gives ten times less dark counts when compared with an identical NbN detector[63], offering a higher signal-to-noise ratio, which is desirable for applications sensitive to dark count rate, such as quantum key distribution (QKD).

Coupling to a device that may be micrometers long but only tens or hundreds of nanometres wide leads to low efficiency, as noted by Gol’tsman[45]. This is due to the spot size of the light source being significantly wider than the wire. A method of achieving better efficiency is to meander the nanowire across a larger area[65], giving improved optical coupling, and is shown in figure 2.5**A**.

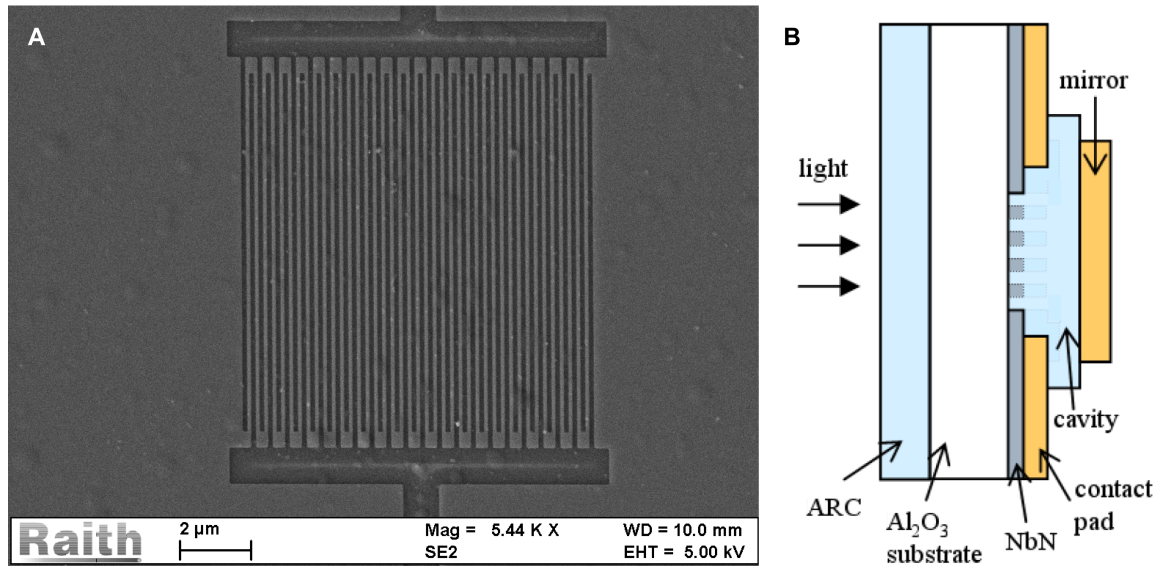


Figure 2.5: A scanning electron microscope (SEM) image of a meander-type geometry SNSPD and a diagram of a meander-type geometry in a cavity. SEM image shown in **A** shows a  $10\ \mu\text{m}$  by  $10\ \mu\text{m}$  meander wire device patterned on quartz. The ‘bubbling’ seen in the image is in the substrate and not a defect of the patterning. Image courtesy of Dr Michael Tanner. **B** is an illustration of the cavity setup used by Rosfjord[66]: the cavity is set up such that light that isn’t absorbed on the first pass of the NbN wire is reflected back by the mirror. It is set up such that the interference minimises reflectance on the surface of the NbN, leading to increased absorption. Image taken from Rosfjord[66].

Absorption can be improved by embedding the meander between reflectors, in an optical cavity. By back-side coupling into an optical cavity with an anti-reflection coating[66], Rosfjord achieved 57% detection efficiency at 1550 nm, reaching 67% at 1064 nm wavelength. This enhances the response by reflecting light not absorbed by the device back across it: classically, this can be thought of as giving the photon multiple chances to be absorbed. The setup is shown in figure 2.5B. Marsili has fabricated an SNSPD in a NbN film on a GaAs distributed Bragg reflector (DBR) substrate[60]. DBRs are formed of repeating alternating layers of material with a depth finely-tuned for a certain wavelength, which is reflected back such that there is constructive interference at a desired position, with the aim of increasing detection efficiency. This is described in more detail in section 2.6.

Tanner achieved, by front-side coupling into an optical cavity of silicon and silicon oxide, a detection efficiency for NbTiN wires of 23% at 1310 nm[64] with 60 ps timing jitter.

A by-product of the grating structure of a square meander is a polarisation dependence of the efficiency of the detector[67]: light striking the meander with the electric field polarised in the wire direction is absorbed more efficiently. Geometries with minimised polarisation dependence have been demonstrated by Dorenbos[68], running the mean-

der in a spiral such that it appears the same when approached from any rotation of the electric field polarisation.

The kinetic inductance of an SNSPD has been shown to have two functions. Firstly, it determines time constants for the rise and fall times of the pulses as it is proportional to them[69]. Secondly it can be used as a measure of uniformity[70] by measuring the kinetic inductance as the bias current is increased to near critical. Constrictions lead to a smaller coefficient in the equation fitted to the data: this coefficient is an indicator as to the uniformity of the device. This is discussed in more detail in section 3.9.

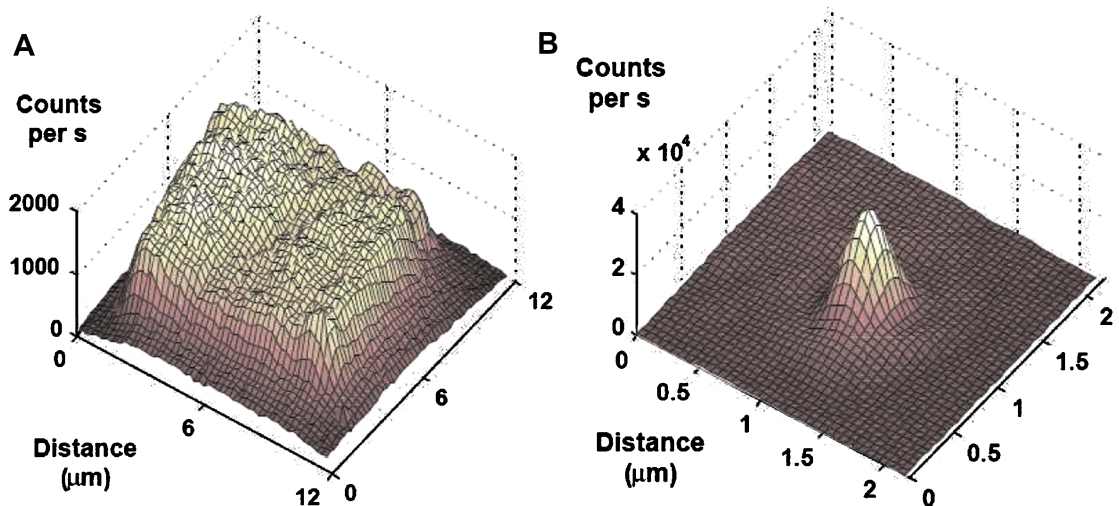


Figure 2.6: A map across two devices, one with constriction. Device **A** has no constriction and responds uniformly, where device **B** is constricted and only a small area is efficient. Image courtesy of Hadfield[71].

During fabrication of an SNSPD, constrictions arise[70] that lead to inefficient detection of photons by limiting the critical current to that of the constricted region. These were spatially mapped by Hadfield[71] (shown in figure 2.6) using a confocal microscope configuration described in detail later. A potential solution to these constricted regions is to pattern parallel-wire devices (sometimes called superconducting nanowire avalanche photodetectors (SNAPs) or cascade-switching detectors[72, 73]) that have multiple wires in parallel. These are biased at a current just below the critical current across all  $N$  parallel wires. When a photon is detected, the wire it strikes becomes resistive and the current is redistributed through the other wires, sending them into the resistive state in a cascade. Ejrnaes[73] found that, due to the reduced inductance, the addition of an inductor in series with the device was required to prevent unstable switches. By implementing SNAPs with ultra-narrow wires and low bias currents, it has been shown that high detection efficiencies are attainable with low constriction[74].

Published literature reports on several other novel SNSPD layouts that have been proposed or fabricated. Dauler created a multi-pixel scheme[76] in which multiple,

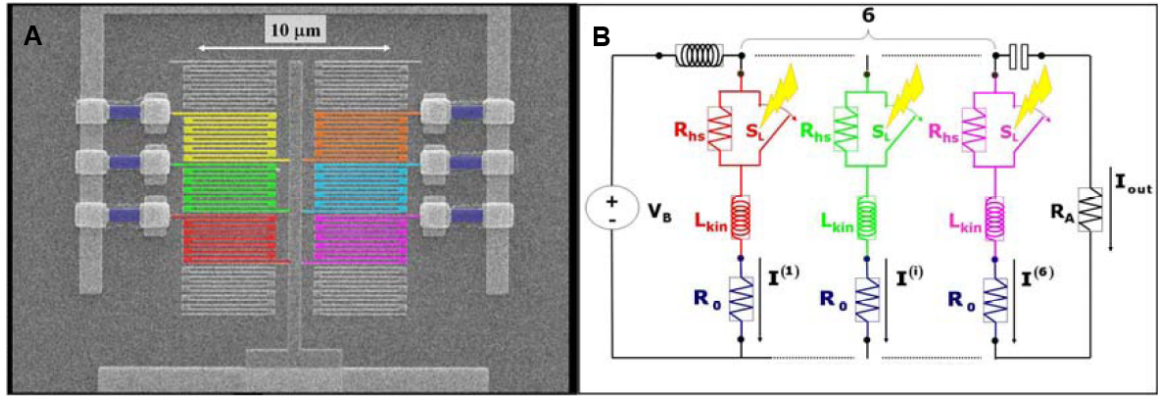


Figure 2.7: SEM and circuit diagram of Divoichy's photon-number-resolving parallel wire scheme. This example is an  $N = 6$  parallel wire detector. The device is a 4 nm-thick NbN film on MgO substrate, with 100 nm-wide wires and 40 % fill-factor. A shows in false-colour the individual wires of the parallel device, while B demonstrates the series resistance allowing photon-number resolution. Image taken from Divoichiy[75].

separately-connected meanders were patterned in a line, designed for spatial, spectral, or photon number resolution. This setup showed little interference between the two detectors, had a timing jitter of 50 ps FWHM, but ultimately requires a linear number of electrical connections with pixels, making many-pixel detectors burdensome. Divoichiy improved photon-number resolution detection[75] with a device capable of resolving up to four photons. This setup has  $N$  parallel wires with series resistances that output a pulse, the height of which is proportional to the number of photons detected. The setup of this device is shown in figure 2.7.

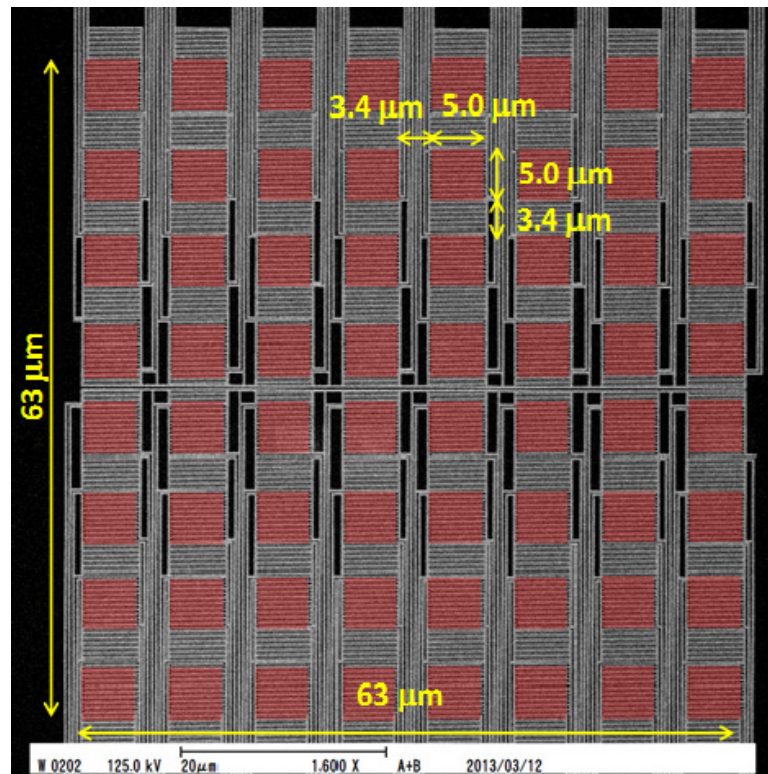


Figure 2.8: SEM of Miki's 64-pixel SNSPD array. Red areas represent the active detector regions. Image taken from Miki[77].

Miki has fabricated a 64-pixel array of  $5\ \mu\text{m}$  by  $5\ \mu\text{m}$  detectors with high uniformity[77], shown in figure 2.8. This system requires 64 output channels however, which is prohibitive. Verma demonstrated a readout scheme whereby an  $N \times N$  pixel array of SNSPDs could be electronically operated using  $2N$  channels[78], a significant improvement on the naive  $N^2$  readouts. Yamashita has proven single flux quantum (SFQ) circuits, a low-power superconducting electronic circuit technology, are able to multiplex multiple SNSPDs and allow readout via a single channel[79].

## 2.3 Reaching cryogenic temperatures

Making things very cold is non-trivial because of the asymptotic approach to absolute zero predicted by the third law of thermodynamics[80]. However, exploitation of superconducting phenomena relies on being able to cool the superconductor to below its transition temperature[36], and so is of importance to SNSPDs.

### 2.3.1 Helium dewar

From the end-user's perspective, the simplest and lowest-vibration method of using an SNSPD is to place it in a dewar of pre-liquefied helium  $^4\text{He}$ , also called LHe. LHe boils at 4.2 K[81], several degrees below the transition temperature of a typical NbN or NbTiN thin film[82], and is available from commercial suppliers. However, LHe is becoming increasingly rare, which has pushed the cost of operating a detector using this as refrigerant up. In addition to the running cost of the system, systems operating by LHe are limited to operation only when the refrigerant is available, which would be a constraint on the use of SNSPDs outside of a development environment. This refrigeration method was used in early work by our research group[71, 83].

### 2.3.2 Closed-cycle refrigeration

Use of a regenerative cryocooling system avoids the running cost of LHe, at the expense of the initial cost of a cold head and the design and construction of a cryostat. The idea began with the Stirling cycle, and lead through to the development of the Gifford-McMahon (GM) cryostat and pulse tubes, which are sufficient for SNSPD operation. These are similar principles to the operation of a domestic refrigerator. To allow the reader a better understanding of why the work presented in this thesis is built on a commercial pulse tube cryostat, qualitative descriptions of the operating principles of these cooling technologies follow.

**Stirling cycle:** The Stirling cycle, invented with the Stirling Engine in 1815 as a means to do work, can be reversed to refrigerate[84]. The system is simple to explain and operate, but operates at high frequencies (20 Hz to 60 Hz[85]) causing significant vibration. Subsequent refrigeration technologies are derived from this design. The operating principle is shown in figure 2.9.

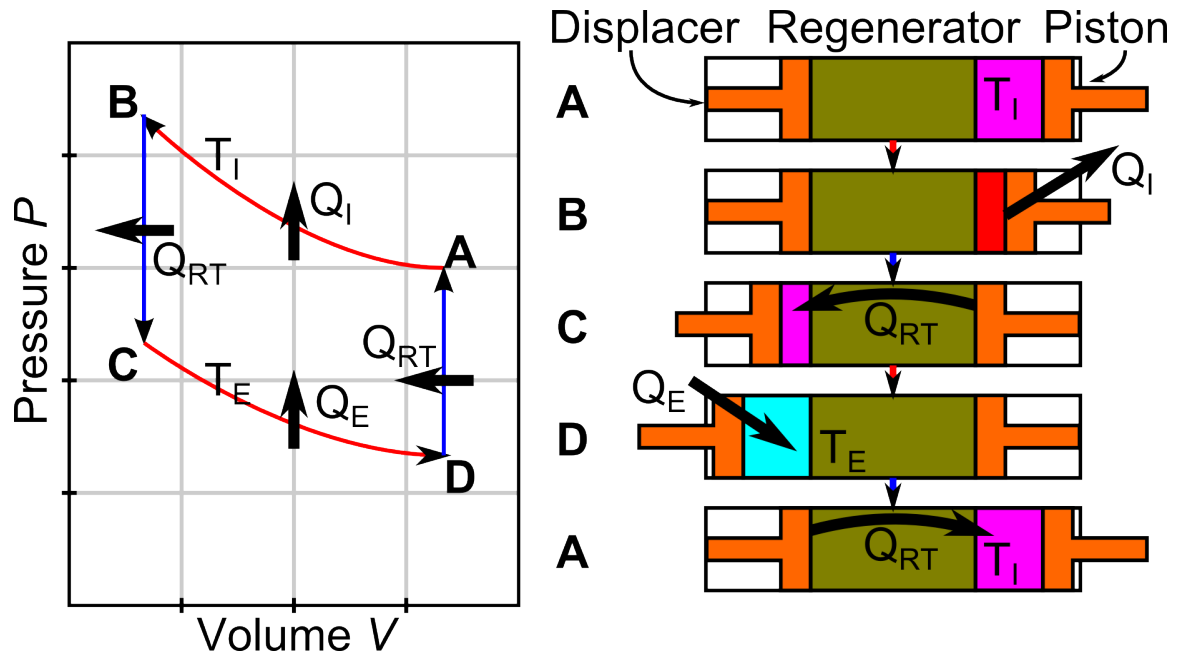


Figure 2.9: Operation of an ideal Stirling cycle[86, 87]. A system initially at temperature  $T_I$  (A) is isothermally compressed by a piston (A to B), releasing heat  $Q_I$  to the surroundings. The system undergoes regenerative cooling at constant volume (B to C), storing heat  $Q_{RT}$  in the regenerator and so reducing the pressure. The system undergoes expansion, with the displacer increasing the volume isothermally (C to D), drawing heat  $Q_E$  into the system. The system then undergoes regenerative heating as the volume is transferred from the displacer to the piston, forcing the gas through the regenerator (D to A). The process then repeats, typically at 20 Hz to 60 Hz[85].

This type of refrigerator operates efficiently, achieving the same coefficient of power as the Carnot cycle. However, it is important to minimize the internal volume of the system, to minimize the required piston sizes and swept volume. For this reason, in any practical realisation of the pump oil-free pistons and displacers must be used, which reduces the reliability. Additionally, it has high vibration due to the moving parts and high frequencies required to operate.

**Gifford-McMahon:** The GM cycle[88] improved on the reverse Stirling cycle by the introduction of a rotary element between the cold and hot sides of the system alternating connection between high- and low-pressure gas lines. The decoupling of the compressor and displacer allows operation of the cold head at much lower frequencies compared to the compressor (typically 1 Hz to 2 Hz, while the compressor runs at mains electric frequency), though the coefficient of power suffers thanks to

the irreversible expansion through the valves of the rotary element[87]. A corollary of this is that the volume bound by the compressor-side of the rotary element may be significantly higher in volume, allowing for oil-lubricated compressors and oil-removal equipment (purification traps), which increase reliability[85]. This makes the Gifford-McMahon cooler a common solution for obtaining the cryogenic temperatures required for SNSPD systems. The Quantum Sensors Group has several Sumitomo Heavy Industries GM cold heads in operation, which are sufficient for successful fibre-coupled SNSPD operation[14, 17, 83, 89]. The operating cycle of a GM cryostat is shown in figure 2.10.

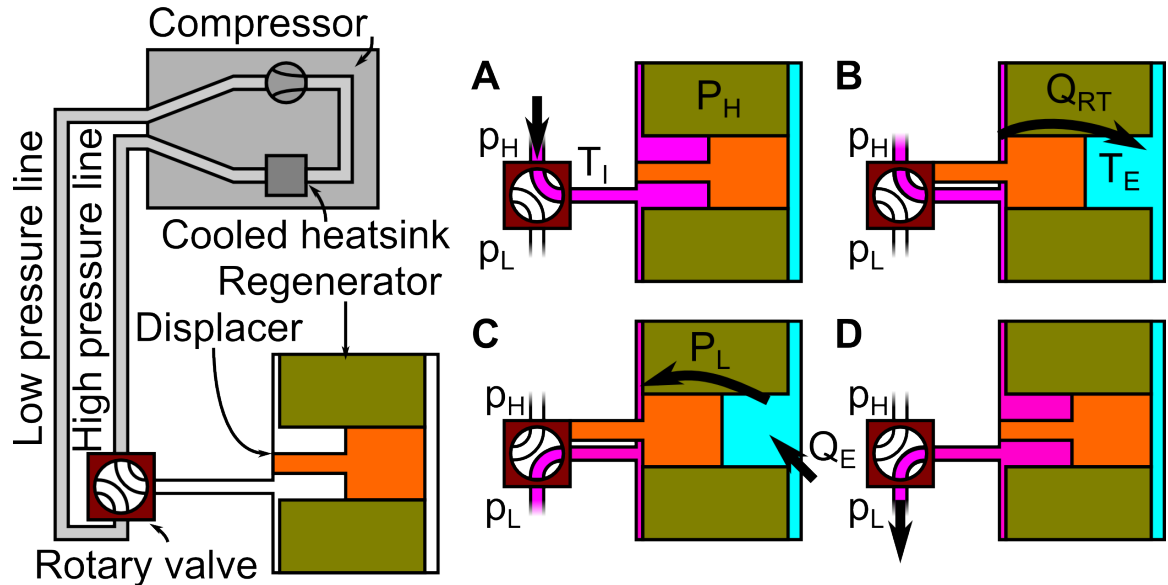


Figure 2.10: Operation of the GM cycle[87]. A system initially at temperature  $T_I$  (A) is connected to the high-pressure  $P_H$  gas line by a rotary valve. It undergoes regenerative cooling at constant volume (A to B) as the displacer moves, storing heat  $Q_{RT}$  in the regenerator. This reduces the pressure at the cold end, drawing further gas through the regenerator. The rotary valve connects the system to the low-pressure  $P_L$  line, causing the gas to undergo expansion isothermally (B to C), drawing heat  $Q_E$  into the system. The gas undergoes regenerative heating as it is transferred from the cold end to the low-pressure pipe by the displacer moving (C to D), forcing the remaining gas through the regenerator. The rotary valve then connects again to the high-pressure line (D to A), completing the cycle. The process repeats typically at 1 Hz to 2 Hz[85]. Heat is released in the cooled heatsink in the compressor.

**Pulse tube:** The GM cycle still suffers vibrational noise, and the displacer and often regenerator are prone to failure as they are mechanical. The pulse tube offers a solution with no moving parts in the cold head[85, 90]. Pulse tubes come in two general types: Stirling-type, which operate at 60 Hz and have high efficiency, but have a higher base temperature[91], and GM type, which operate at 1 Hz to 2 Hz, are less efficient but have low vibration, and can reach temperatures below 4 K[92]. We concern ourselves only with the GM-cycle pulse tube. The system layout is shown in figure 2.11. This is a linear pulse tube, where the cold spot is in the middle of the cooler.

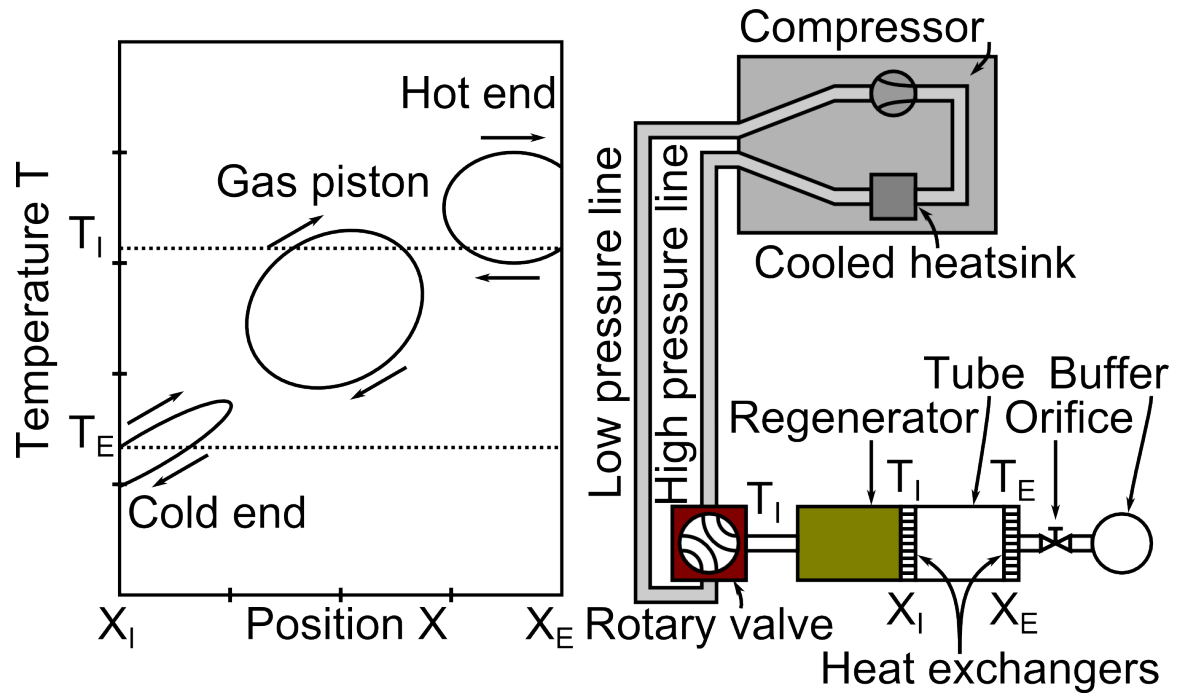


Figure 2.11: Layout of a GM-cycle linear pulse tube[91]. The only moving parts are in the compressor and in the rotary valve. The operating principle is as follows[87]: driven by the alternately-connected pressure lines, the pressure in the pulse tube varies smoothly. In the regenerator and heat exchangers the gas is in good thermal contact. The buffer is at a pressure which is effectively constant. In the pulse tube the gas has no thermal contact with the surroundings. Gas in the pulse tube can be categorized as gas which moves through the ambient temperature heat exchanger  $X_E$ , gas which moves through the cold heat exchanger at  $X_I$ , and gas which remains within the tube (the ‘gas piston’). The position and temperature of these categories during a single cycle is shown in the graph. At the hot end  $X_E$  gas flows in and out of the buffer via the orifice as the pressure in the tube oscillates. Thanks to the presence of the orifice, gas is drawn into the tube at a lower pressure and so temperature  $T_I$ , and is forced out at a higher pressure and temperature. This heat is released by the heat exchanger at  $X_E$  to the surroundings. At the cold end, the gas enters the tube with temperature  $T_I$  when the pressure is high, and returns when the pressure is low and the temperature below  $T_I$ , thereby cooling. The operating process repeats typically at 1 Hz to 2 Hz[85].

The Cryomech cryogenic refrigeration system used in this work exploits this closed-loop expansion cycle[93]. 99.999%-pure He gas is compressed by a water-cooled Cryomech CP830, the heat of compression being removed from the refrigerant by a heat exchanger in thermal contact with the cooling water. This high-pressure helium is pumped by flex line to a remote motor mounted near the PT403 pulse tube cold head. This minimizes vibration in the attached system. The remote motor is a rotary valve. Within the cold head, the refrigerant undergoes adiabatic expansion as described in figure 2.11, cooling to cryogenic temperatures. The refrigerant is then returned via the low-pressure helium flex line to the compressor.

The low vibration offered by no moving parts at cryogenic temperatures[85] makes a cryostat based on the pulse tube design ideally suited as the base on which to house vibration-sensitive nano-optical testing apparatus.

## 2.4 Vacuum technology

Vacuum technology is an important tool for reaching low temperature efficiently, as thermal energy can be transferred quickly by convection and conduction. A vacuum is defined as the state of a gas at which its pressure in a vessel and therefore its particle density is lower than that of the ambient surrounding atmosphere[94]. A vacuum is useful when operating at low temperature as it reduces the conduction and convection forms of heat transfer from room temperature to the cold head. Pressures are typically measured in mbar: atmospheric pressure at sea level is approximately  $10^3$  mbar. Pressures down to  $10^{-3}$  mbar are considered ‘low’ vacuum; pressures down to  $10^{-7}$  are considered ‘high’ vacuum.

### 2.4.1 Flow regimes

The mean free path  $\bar{L}$  gives a measure of how far gas molecules can travel before they collide, and is calculated for identical particles[94] as

$$\bar{L} = \frac{k_B T}{\sqrt{2} \pi p d_m^2} \quad (2.4)$$

where  $k_B$  is the Boltzmann constant and equals  $1.381 \times 10^{-23} \text{ J K}^{-1}$ ,  $T$  is the temperature of the gas,  $p$  is the pressure, and  $d_m$  is the molecular diameter. This can be used alongside the diameter of the flow channel  $d_{flow}$  that bounds the gas to determine the Knudsen number  $K_n$

$$K_n = \frac{\bar{L}}{d_{flow}} \quad (2.5)$$

which is a dimensionless measure that indicates which flow regime the gas is in. In the viscous flow regime most of the collisions of the gas are with other gas molecules. This is typically true down to  $10^{-1}$  mbar. In the molecular flow regime, the mean free path is greater than the diameter of the bounding container, and the gas collides almost exclusively with the walls and not other molecules. This is typically true from  $10^{-3}$  mbar down. In the Knudsen flow regime, the gas is transitioning from the viscous flow regime to the molecular flow regime, and collisions with other gas molecules are about as likely as collisions with the bounding walls. The boundary values are shown in table 2.2.

	Viscous flow	Knudsen flow	Molecular flow
Knudsen number	$K_n < 0.01$	$0.01 < K_n < 0.5$	$K_n > 0.5$

Table 2.2: Flow regimes by Knudsen number

## 2.4.2 Conductance

When evacuating a vacuum chamber to high vacuum, the vacuum pump is connected via piping. The conductance of this piping  $L_{cond}$  is defined as

$$L_{cond} = \frac{q_{pV}}{\Delta p} \quad (2.6)$$

where  $q_{pV}$  is the gas throughput and  $\Delta p$  is change in pressure across the length of pipe. The gas throughput  $q_{pV}$  is defined[95] as

$$q_{pV_{vol}} = \frac{d(V_{vol}p)}{dt} \quad (2.7)$$

where volume is denoted as  $V_{vol}$ . Conductances are additive when piping is connected in parallel, and the reciprocals are additive if piping is connected in series. In the viscous flow regime, the conductance is proportional to pressure: in the molecular flow regime, as there is no interaction between gas molecules, it is independent. From this we can determine that by doubling the length of piping between the vacuum chamber and the pump, a halving of the conductance occurs: for reasonable pumping times, a short pipe is vital.

## 2.4.3 Pump selection

The pump used in much of this work was an Adixen ATP80 turbo molecular pump[96] backed by an Adixen ACP15 Roots roughing pump[97]. These were chosen to get to a final pressure of order  $10^{-7}$  mbar, the roughing pump allowing access down to  $10^{-1}$  mbar and the turbo molecular pump operating from there onwards. It is worthy of note that the cold head itself operates as a cryopump when switched on and cold, adsorbing incident gas molecules.

A Roots vacuum pump operates using two synchronously counter-rotating rotors[94] and is useful for reaching a low vacuum. It is unable to function in the molecular flow regime, at which point the turbo molecular pump becomes useful: this is a set of rotors and stators (static rotors) which trap incident molecules and push them through the pump to the exhaust, which is the inlet of the Roots pump.

Any method of reducing the pressure in a vessel is ultimately vacuum technology. For this reason, the cryostat itself may be considered a vacuum pump: once at operating temperature (around 4K) most gases will readily adsorb onto the cryostat or its connected structures, so reducing the pressure in the vacuum chamber. Subsequently, small leak rates and out-gassing observed in any real vacuum system do not allow conduction to occur while the cryostat is in operation.

## 2.5 Plasmonics and nanoantennas

A material with free electrons, such as a metal, can be described classically by modelling the electrons as a freely-propagating gas in a grid of oppositely-charged atoms[98]. When an electromagnetic field impinges upon these electrons, their position begins to oscillate at that material's plasma frequency, ultimately being damped by collisions with the lattice. These oscillations of the plasma are formed of quasiparticles referred to as plasmons.

When light propagating through a dielectric interacts with a plasmonic material, at the boundary there is interaction between the plasma and the electric field of the light that creates surface plasmon polaritons (SPPs)[99]. These have a shorter wavelength than the photon, and travel perpendicularly along the boundary, which allows the field intensity to be confined to a volume smaller than the diffraction limit. If these are confined to a nanoparticle smaller than the wavelength of the light that excited the SPPs then they are referred to as localised surface plasmons (LSPs)[99]. Nanoantennas at visible and IR wavelengths exploit the LSP resonance, and are designed to couple incident photons into the local plasmon resonance of the antenna material[100], allowing strong localization of the optical field below the optical limit[101]. These are frequently exploited for use in sensing applications[102]: for example, nanoantennas exploiting surface plasmon resonance for photodetection have been successfully demonstrated in the near-IR on a germanium metal-semiconductor-metal (MSM) detector[103].

Some work has been carried out to enhance SNSPD performance by exploiting plasmonics: one approach has been to deposit a full layer of gold over the nanowires and couple in through the back side[104] creating a combined nanoantenna and cavity. This design is shown in figure 2.12, and its response simulated by myself in section 2.5.1. Another approach used nanocavities and reflectors rather than nanoantennas[105]. Perhaps most relevant for the work contained within this thesis, Heeres fabricated LSP-resonant gold monomer and dimer antennas on 100 nm-wide SNSPDs, showing a factor of 2 enhancement in the SDE at wavelengths from 656 nm to 1300 nm[106].

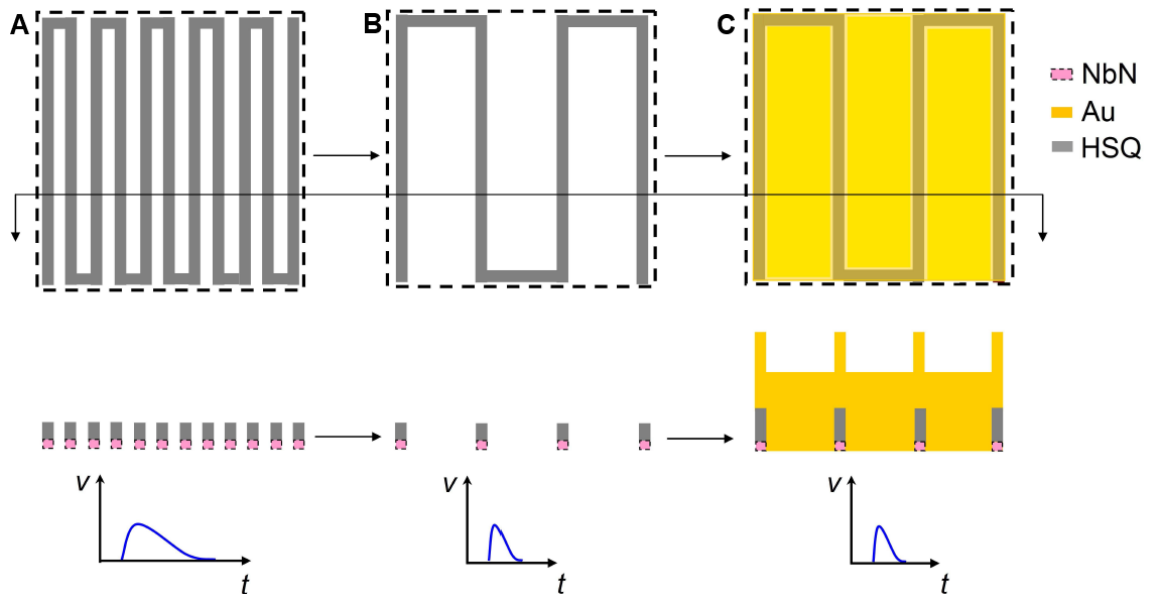


Figure 2.12: Diagram of geometry and timing response of plasmon-enhanced single photon detector. Images are top-down, cut-through, and a graph of the reset time of the pulse. **A** shows a typical SNSPD meander, only with a hydrogen silsesquioxane (HSQ) dielectric layer: the meander is densely-packed, and has a long relaxation time. **B** shows a sparse meander, with a correspondingly quick reset time. **C** shows the same as **B**, but with a layer of gold deposited across the active area. Image taken from Hu[104].

### 2.5.1 Simulation of plasmonic behaviour

It is possible to numerically implement Maxwell's equations and in doing so model the behaviour of plasmonic structures. There are various methods to perform this: I made use of the commercial package Lumerical finite difference time domain (FDTD) Solutions to this end. Operating within the time domain, FDTD simulations are able to simultaneously simulate a broad range of frequencies, of great interest when looking for plasmon resonances.

As the FDTD method numerically calculates an approximation of electromagnetic behaviour[107], the simulation is intrinsically approximate, and it is important to be careful in the handling of the result in light of this. For this reason, I have performed an example simulation of an accepted result from literature that has been verified experimentally.

Hu simulated and tested[104] an 80 nm-wide NbN nanowire with a 600 nm pitch illuminated from the back side, through a sapphire substrate. Atop this wire was HSQ resist 180 nm high. This design then had a 3 nm Ti adhesion layer and 300 nm Au deposited to form the nanoantenna. This is shown in figure 2.12C. Hu et al. performed their own finite-element analysis of the ideal system[104], obtaining a maximum enhancement in the absorption into the nanowire for an incident wavelength of 1550 nm of 8 times, and an absolute absorption of 47%, though these were both obtained with a

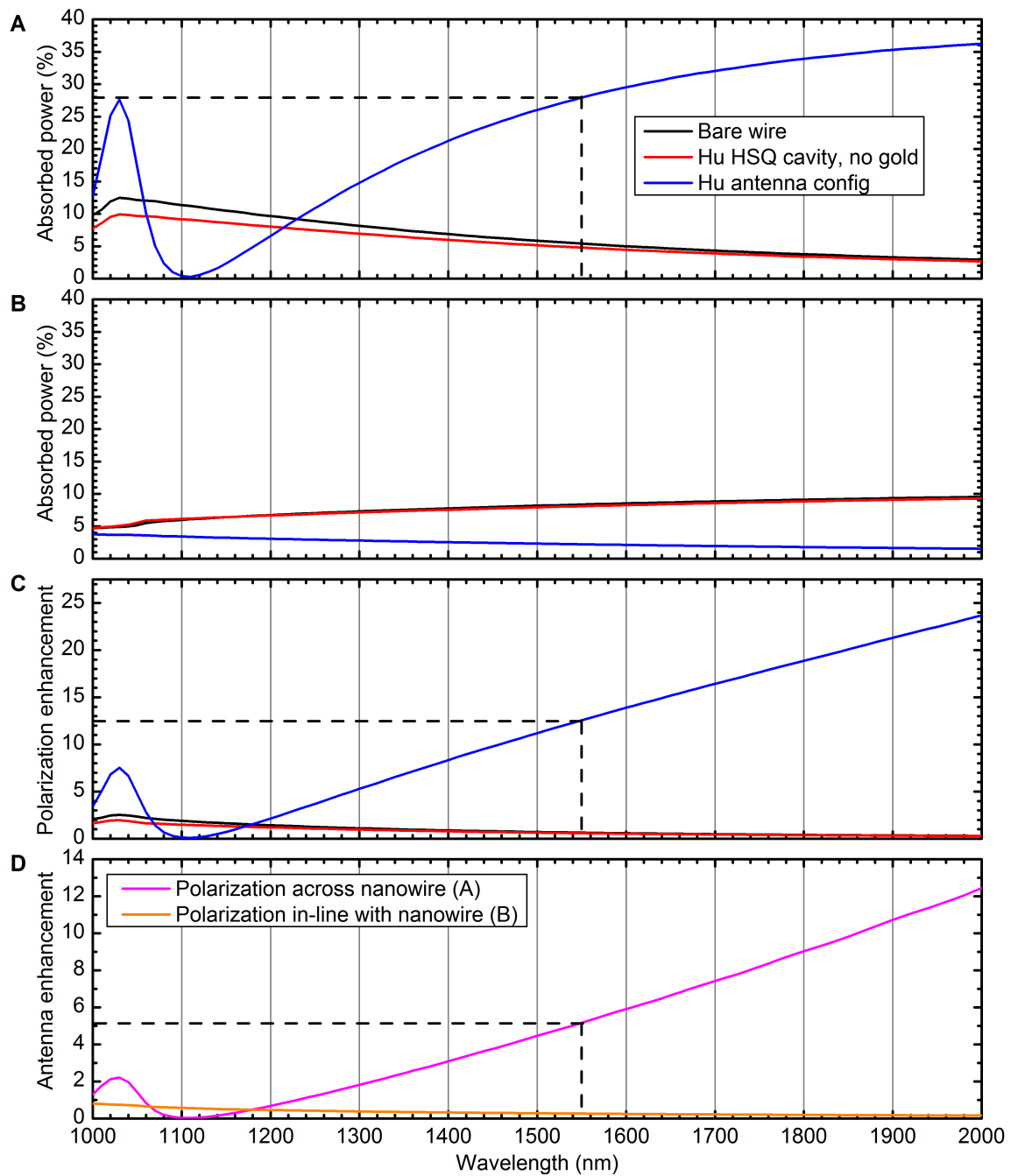


Figure 2.13: FDTD simulation results for comparison with literature. This presents results of a 3D simulation of the geometry fabricated in 2011 by Hu[104] carried out in Lumerical FDTD Solutions, a commercial simulation package. **A** and **B** shows the absorbed power for three cases: when illuminating a bare wire, when illuminating a wire with a HSQ cavity, and when illuminating the full antenna configuration as specified in the literature. In **A**, the electric field polarisation is linearly polarised across the nanowire. In **B**, the electric field polarisation is linearly polarised along the nanowire. **C** shows the enhancement in the photoresponse obtained by dividing the data in **A** by the data in **B**, and can be thought of as the enhancement with polarisation. **D** represents the enhancement at the two polarisations obtained by the addition of the Hu antenna to the bare wire (blue data divided by black data).

HSQ height of 150 nm, which was not what was ultimately fabricated. They note the experimentally-measured SDE varies with electric field polarisation, from a minima of 3.5 % to a maxima of 47 %, a polarisation sensitivity of 13.4 times.

Figure 2.13 presents the result of my own model in Lumerical FDTD Solutions of the system fabricated by Hu. Figures 2.13A and B are absorbed power into the nanowire as a function of illumination wavelength. Figure C demonstrates the polarisation sensitivity for each geometry, and figure D shows the enhancement in the absorbed power at the two extremes of linear polarisation. As shown with black dashed lines for an incident wavelength of 1550 nm, these simulations suggest an absolute absorption of 28 % (figure A). They suggest an enhancement in the absorbed power of 5 times when an antenna is present (figure D), and a polarisation sensitivity of 13 times (figure C). One reason for the slight disagreement regarding the absorbed power and enhancement factor between Hu’s simulated results and mine is that Hu simulates the best-case design, while I simulate Hu’s fabricated geometry; additionally, it is likely that there are differing complex refractive indices used in each model, especially for NbN. By obtaining agreement between my simulation and results from literature, I demonstrate the usefulness and validity of the FDTD method. This is utilized heavily in Chapter 5.

## 2.6 Optical cavities

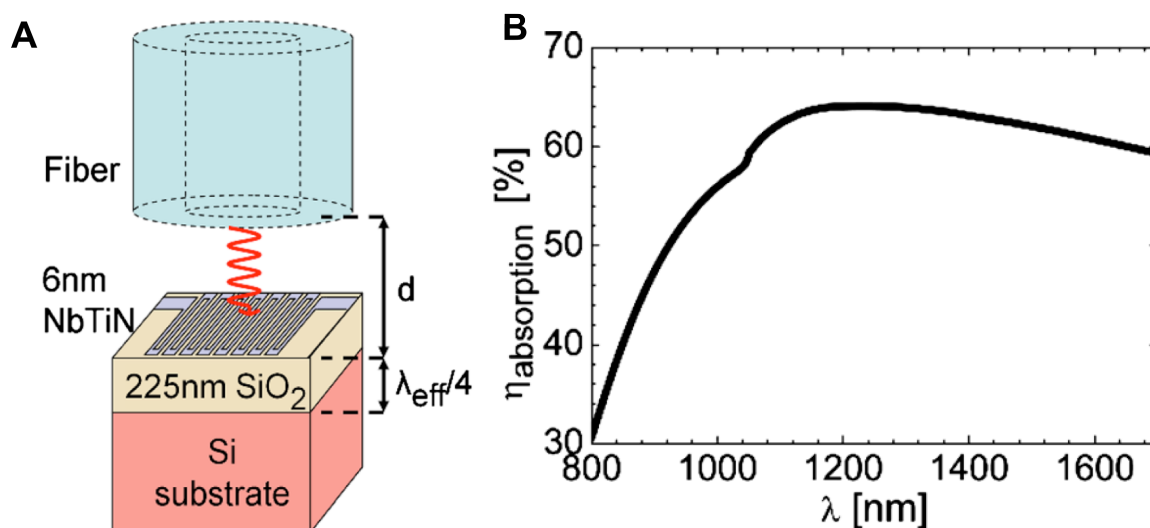


Figure 2.14: Layout and behaviour of a half-cavity design. A shows a schematic of the device layout: light is delivered by a front-side coupled optical fibre to an SNSPD fabricated from 6 nm NbTiN. A layer of SiO<sub>2</sub> separates this from the Si substrate. This creates a partial reflector, at a length of 225 nm. With  $n = 1.45$  for SiO<sub>2</sub> and  $n = 3.5$  for Si, the cavity is designed to enhance 1310 nm photon absorption. A simulation of the absorption coefficient with wavelength is shown in B, reaching 65 % at 1310 nm: without the reflective layer, the paper reports it is about 15 %. Images courtesy of Tanner[64].

An optical cavity is formed when reflective surfaces are positioned such that standing waves form between them. This constrains the resonant wavelength within the cavity. This is a key component of the operation of the tunable lasers described in section 3.14. The effect applied to SNSPDs allows photons trapped within the cavity what may be classically considered as ‘multiple passes’ of the detector, increasing absorption[64, 66].

A common figure of merit for a cavity is the Q-factor, a dimensionless value that represents the loss rate of the energy stored within the cavity. This is expressed numerically as

$$\begin{aligned} Q &= 2\pi \frac{\text{stored energy}}{\text{dissipated energy per cycle}} \\ &= \frac{2\pi f_0 \mathcal{E}}{P} \end{aligned} \quad (2.8)$$

where  $f_0$  is the resonant frequency,  $\mathcal{E}$  is the stored energy, and  $P$  is the dissipated power. A good cavity has a high  $Q$  value: however, when using a cavity to enhance absorption, the presence of the absorbing medium means that the  $Q$  value will be significantly lower than the empty cavity.

By fabricating an optical cavity with a DBR as the mirror, it is possible to achieve higher absorption. As seen in figure 2.14, a single  $\text{SiO}_2/\text{SiO}$  interface is able to reflect a sufficient portion of incident light to create a measurable increase in the absorption: if the incident light is linearly-polarised and is normal to the interface, the reflectance of normally-incident light  $\mathcal{R}$  can be calculated by the Fresnel equation[108]

$$\mathcal{R} = \left| \frac{n_1 - n_2}{n_1 + n_2} \right|^2. \quad (2.9)$$

where  $n_1$  and  $n_2$  are the refractive indices of the first and second materials respectively. For light in a DBR cavity, we assume that the beam waist approximates normal incidence. This equation can be approximated for a DBR with two other refractive indices[109]  $n_0$  and  $n_s$

$$\mathcal{R} = \left| \frac{n_0(n_1)^{2N} - n_s(n_2)^{2N}}{n_0(n_1)^{2N} + n_s(n_2)^{2N}} \right|^2. \quad (2.10)$$

where  $n_0$  is the refractive index of the originating medium and  $n_s$  is the refractive index of the substrate, and with  $N$  representing the number of repeated pairs. This approximation is valid for low-reflectivity stacks, which is acceptable for the DBRs used in this work. Using these equations we can see that the reflectance of the simple reflector with  $n_1 = 1.45$  for  $\text{SiO}_2$  and  $n_2 = 3.5$  for Si is  $\mathcal{R}_{simple} = 17.2\%$  at 1310 nm, while the reflectance of the DBR  $\mathcal{R}_{dbr}$  with  $n_0 = 1$  for vacuum,  $n_1 = 3.018$  for AlGaAs layers,  $n_s = n_2 = 3.37$  for GaAs layers and substrate and  $N = 30$  is  $R_{dbr} = 99.8\%$ .

Subsequently, the increased reflectivity of the DBR over the simple reflector is apparent. This is increased further if these reflectors bound a cavity, creating a standing wave.

As the first antinode occurs a distance of  $\lambda_0/4$  from the AlGaAs to GaAs boundary, and the irregular structure of AlGaAs is undesirable for depositing a thin film onto, a  $\lambda_0/2$ -length layer of GaAs may be deposited on the top of the optical stack. This ensures the second antinode of the standing wave will be within the film, a technique which has been used by other groups when fabricating GaAs/AlAs DBRs[110].

# Chapter 3

## Experimental and analytical methods

In this chapter the processes used to create superconducting nanowire single photon detectors (SNSPDs) and the experimental setup shown in figure 3.1, which was used to nano-optically test the detectors, is described. Procedures used in results presented in Chapter 4, 5, and 6 are discussed in detail, and derivations of important equations are performed.

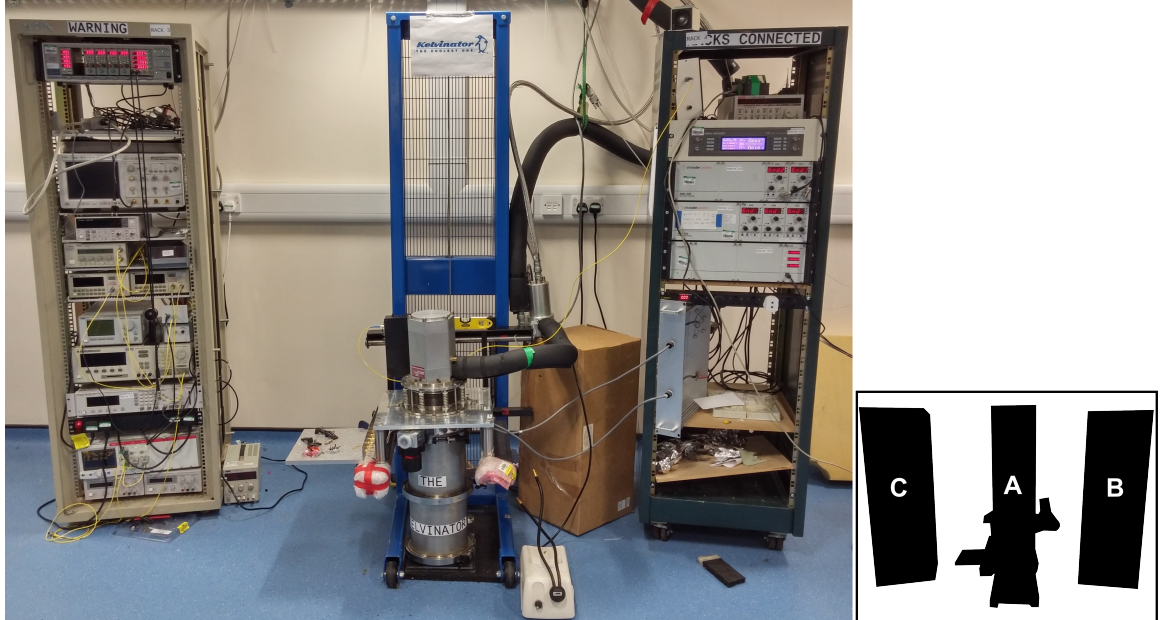


Figure 3.1: Photograph of ‘Kelvinator’ testing setup. **A** is the cryostat itself, with the vacuum can attached, on vibration-damped matting. The remote motor sits on a wooden box to its right. A breadboard for mounting amplifiers and electrically connecting to the system is attached to its left. **B** is a rack containing the equipment used to control the piezoelectric motors, read position, and read the reflection back from the optics. **C** is a rack containing the biasing circuitry, an oscilloscope used to check pulse shapes, tunable lasers, amplifier power supplies, the polarisation controller, optical attenuators, power meter, pulse-pattern generator, and counting electronics.

### 3.1 Parallel-wire SNSPD fabrication

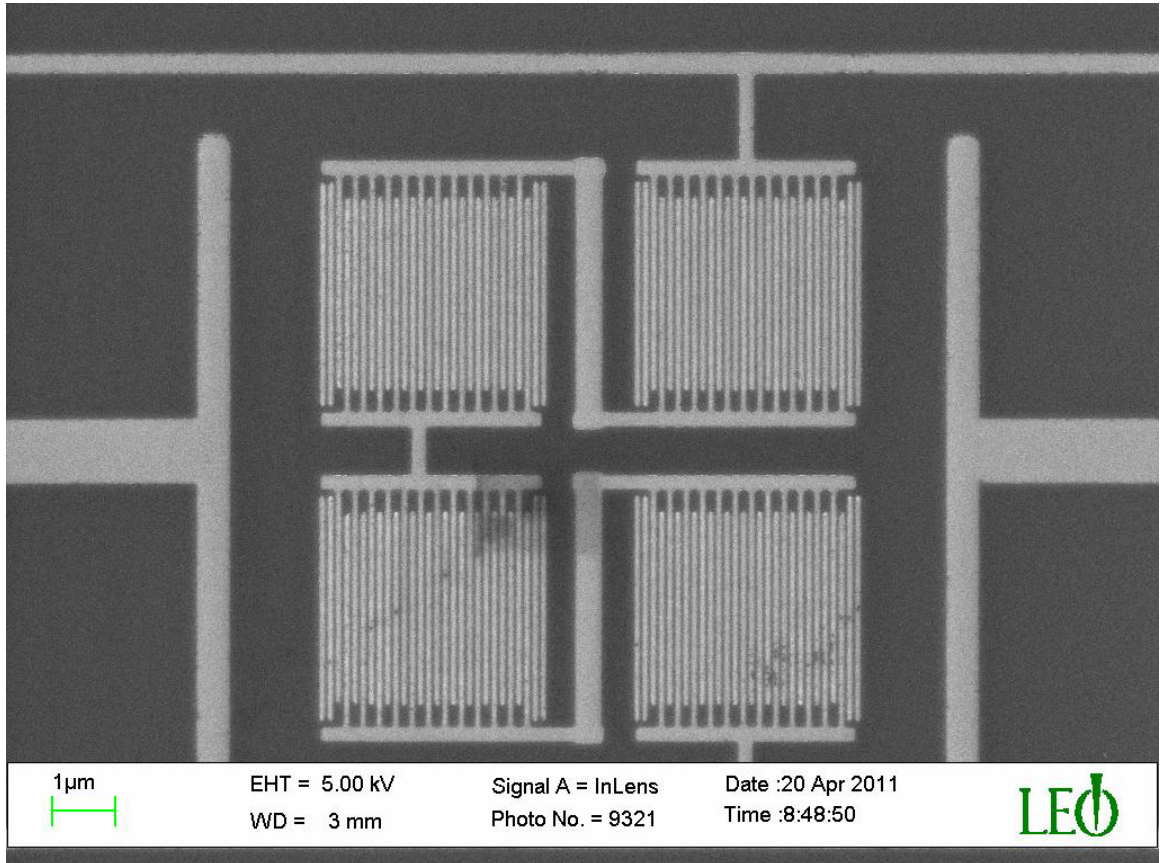


Figure 3.2: Scanning electron microscope (SEM) image of a completed parallel-wire SNSPD. The four spatially-separated pixels are clearly visible. Image courtesy of Dr Lara San Emeterio Alvarez, University of Cambridge, UK.

A method of fabrication for NbN SNSPDs was devised that used the facilities at the University of Cambridge. Our collaborators Dr Lara San Emeterio-Alvarez, Weitao Jiang, and Dr Zoe Barber used the following process to make NbN spatially-separated parallel-wire devices. An SEM image of a completed detector is shown in figure 3.2.

The process is as follows. Firstly, the substrate was cleaned and diced (shown completed in figure 3.3A), then an NbN film was sputtered onto the substrate using reactive sputtering, using a niobium target in a gas of argon and nitrogen as in figure 3.3B. After this, the critical temperature  $T_c$  was measured with a resistive measurement—noting that contacting the film via ultrasonic wirebonding may have left aluminium on the NbN—and the film thickness was measured with grating incidence X-ray diffraction.

To pattern the film, PMMA 950 A4 was spun at 5000 revolutions per minute (rpm) onto the NbN, then spun at 1000 rpm for 30 s, followed by being heated to 110 °C for two minutes, figure 3.3C. The meander design was then written by e-beam lithography onto the PMMA as in figure 3.3D. This was followed by developing the PMMA with isopropyl alcohol (IPA):H<sub>2</sub>O in a 3:7 ratio, removing the exposed lithographed parts (figure 3.3E), then performing a reactive ion etch (RIE) with CF<sub>4</sub> for one minute,

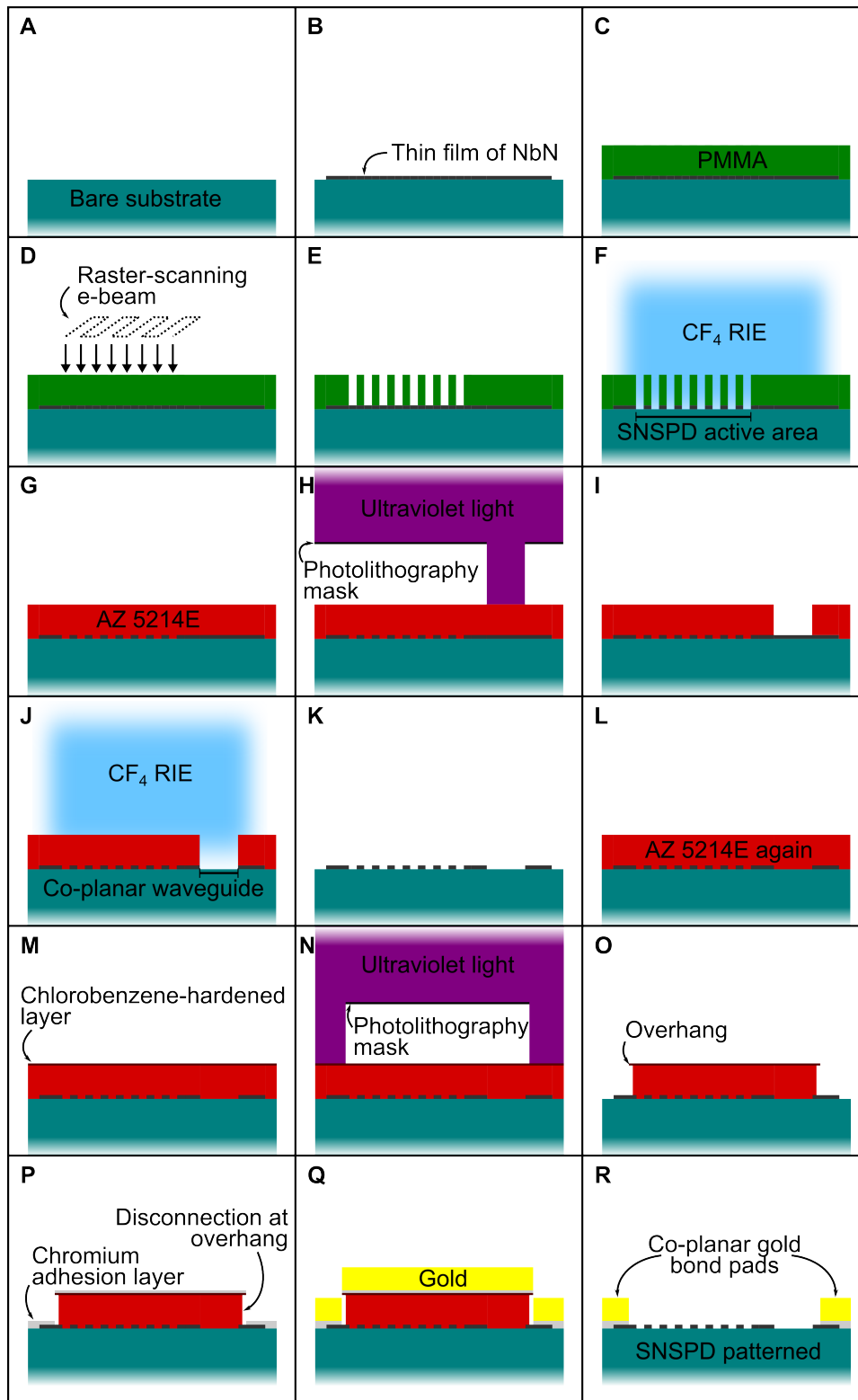


Figure 3.3: Process used at University of Cambridge to fabricate SNSPDs. Substrate cleaned and diced: thin layer of NbN sputtered on. Layer of PMMA spun on top, e-beam raster-scanned over PMMA (A–D). Exposed PMMA removed with developer and NbN removed with  $\text{CF}_4$  RIE. Optical resist applied and substrate exposed to UV light through a photolithography mask, weakening resist which is removed with developer (E–I). RIE removes NbN and remaining resist removed. Resist applied: chlorobenzene applied to this (J–M) hardening the top. Resist exposed to ultraviolet (UV) light through photolithography mask with overhang after developing. Thin layer of chromium and thicker layer of gold evaporated on, overhang preventing connection between layers on the NbN and the resist. Resist then removed (N–R) forming co-planar bond pads, and fabrication is complete.

shown in figure 3.3F to remove the NbN. Next, the PMMA resist was stripped from substrate by being submerged for half an hour in acetone, followed by half an hour in IPA to clean the acetone off. This completes patterning of the photosensitive active area of the SNSPD.

Photolithography was used to remove larger areas of NbN, separating the photosensitive area from the rest of the NbN with AZ 5214E resist. This was deposited by spinning the resist at 8000 rpm for 30 seconds then heating to 120 °C for one minute. Patterning with ultraviolet (UV) light and developing with AZ 531:H<sub>2</sub>O in 1:4 ratio was then performed (shown in figures 3.3G–I), followed by RIE with CF<sub>4</sub> again, to remove bulk areas of NbN (figure 3.3J).

Chromium (for good adhesion) and gold (used as contact pads) were then deposited as follows. The previous AZ resist was stripped off (figure 3.3K), and photolithography with AZ 5214E resist happens a second time. A pattern is placed, the open areas are exposed to UV, and then immersed in chlorobenzene, and developed as before (figures 3.3L–O), the chlorobenzene hardening the top part of the resist and creating an overhang. A thin 5 nm film of chromium then a thick layer of gold is evaporated on the patterned resist, the overhang preventing contact between the material deposited in the patterned area and material on top of the resist (figures 3.3P and Q). Lift-off of the unconnected gold pattern then occurs and the device is completed, shown in figure 3.3R.

## 3.2 Nanoantenna-coupled SNSPD fabrication

Fabrication of nanoantenna-coupled SNSPDs is fundamentally more challenging than fabricating either individual component, because good alignment between the two layers (SNSPD and nanoantenna) is vital. The initial method devised and carried out in 2011 to fabricate nanoantenna-coupled SNSPDs used a lift-off process, whereby the nanoantennas were fabricated by deposition onto a positive e-beam resist pattern. This is detailed in figure 3.5. This suffered from low yield, as to allow the best resonance no adhesion layer was used, so the lift-off process often stripped the nanoantennas off. Additionally, owing to an oversight in the number of alignment markers deposited, the e-beam pattern writer had to be aligned manually, resulting in poor alignment. A revised patterning procedure was developed for later fabrication runs which used negative e-beam resist pattern and etching rather than lift-off, and included 27 alignment markers—two for rough alignment and one for each chip, of which there were 25. The result of this revised scheme can be seen in the SEM in figure 3.4: two halves of a square dipole nanoantenna with a design length of  $L_{des} = 210$  nm lie a design separation of 60 nm apart. Nano-optical testing has confirmed there is good alignment between the

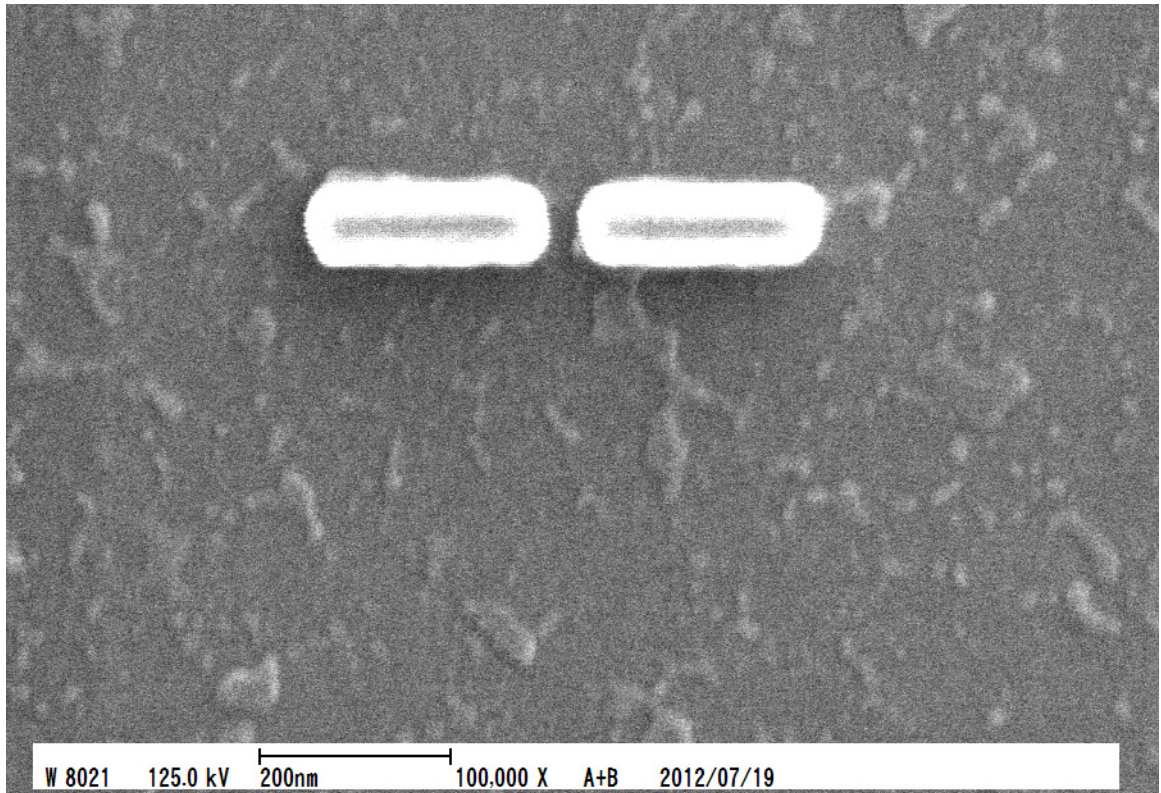


Figure 3.4: SEM image of a completed nanoantenna. The nanowire is embedded under  $\text{SiO}_x$  and so is below the depth resolution of the SEM. Image courtesy of Dr Shigehito Miki, NICT, Japan.

nanoantennas and nanowires with this fabrication process. The nanoantenna-coupled SNSPD fabrication was carried out by Dr Shigehito Miki at NICT, Japan.

### 3.2.1 Gold lift-off method

The initial process was as follows. An MgO substrate had a 4 nm thick film of NbN deposited by reactive direct current (DC) magnetron sputtering at room temperature[58, 111]. A layer of ZEP positive e-beam resist was spun onto the film and an e-beam was raster-scanned over this (figures 3.5A–C). The ZEP was developed and given an RIE, fabricating a single wire (seen in D). Following this AZ 5206E photosensitive resist was deposited. The device was loaded and aligned with a photolithography mask and exposed with UV light. This was inverted by heating for one minute and developed. 30 nm  $\text{SiO}_x$  was then evaporated onto the detector, creating the  $\text{SiO}_x$  spacer, shown in E and F.

To fabricate the nanoantennas, ZEP resist was again deposited, and capped with a layer of S-ZEP (figure G). This was exposed to an e-beam raster pattern and developed (H). A layer of gold was then evaporated onto the detector, and the lift-off procedure was carried out (I and J). This stage also lifted off around 90 % of the nanoantennas, which

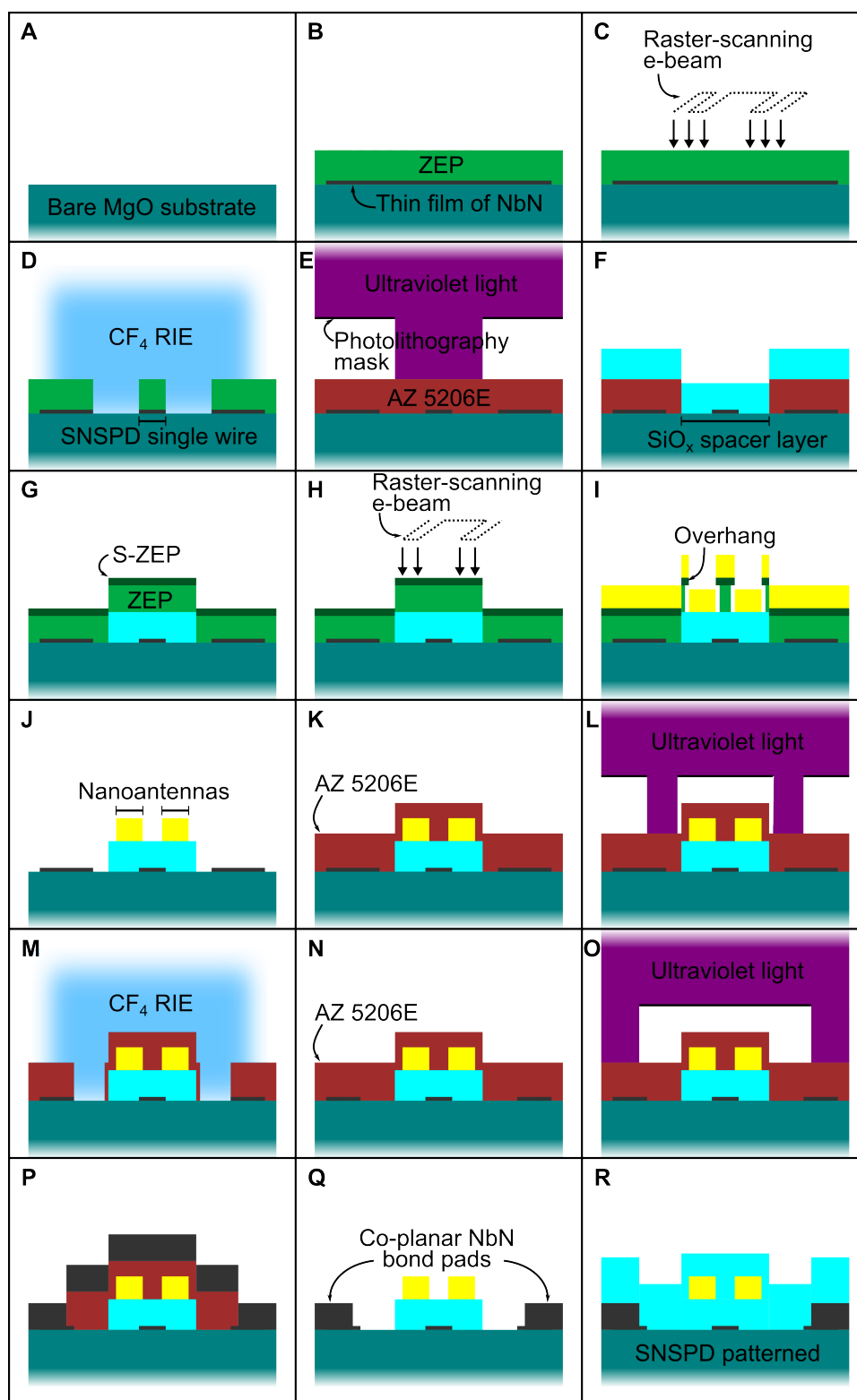


Figure 3.5: Diagram of initial process used at National Institute of Information and Communications Technology to fabricate nanoantenna-coupled SNSPDs. **A–D** show deposition of the thin film, e-beam resist, patterning, and etching of the nanowire area. **E–J** shows the ‘lift off’ method of creating nanoantennas, with deposition of photosensitive resist, photolithography, deposition of an SiO spacer and lift-off, deposition of two layers of e-beam resist, positive patterning, deposition of gold, and lift-off. **K–M** shows patterning the wide meanders at the end of the nanowire by photolithography and etching, and **N–R** shows deposition of thick NbN for use as bond pads, plus the final step depositing a capping layer of 85 nm of SiO.

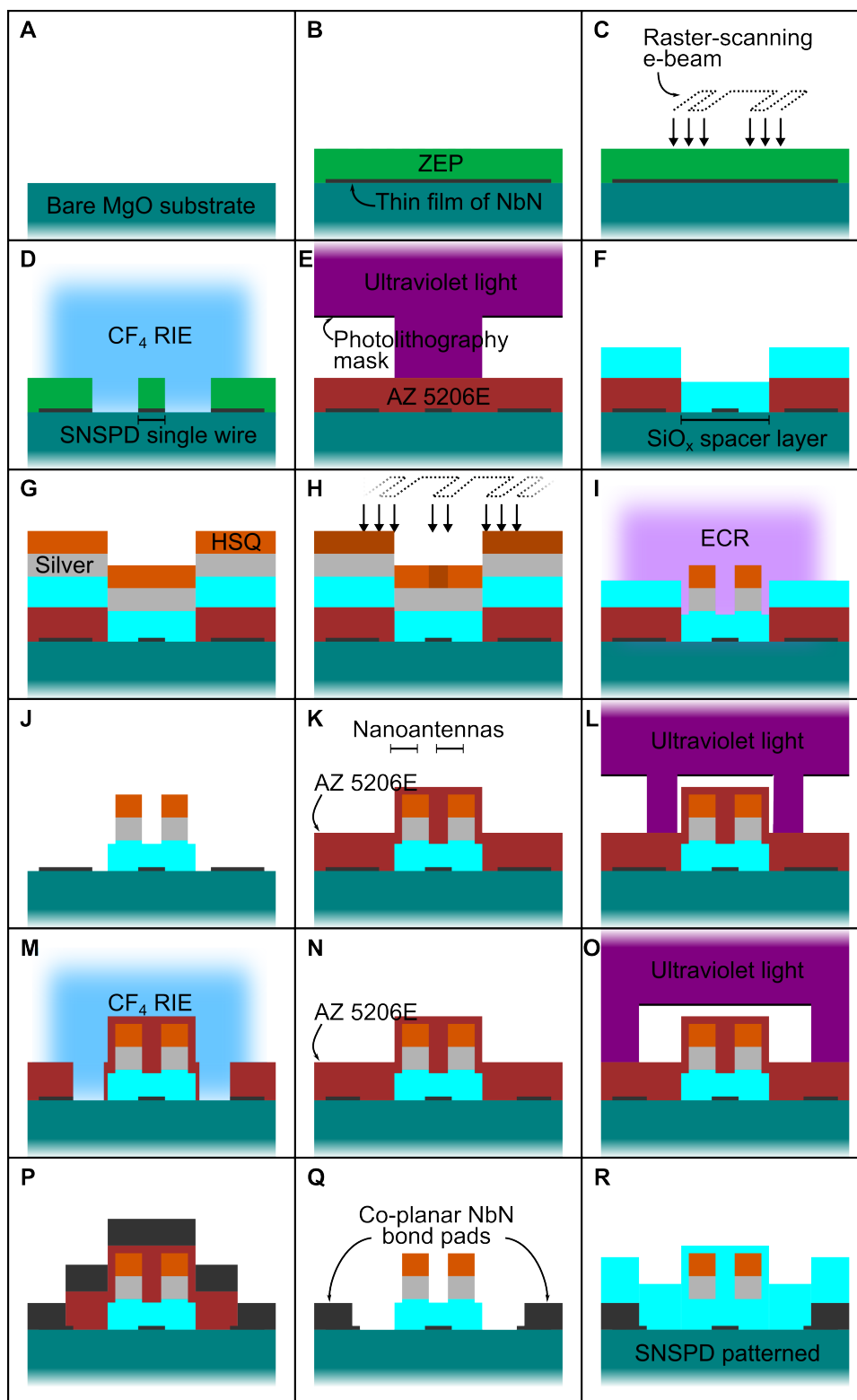


Figure 3.6: Diagram of final process used at NICT to fabricate nanoantenna-coupled SNSPDs. As with the initial method shown in figure 3.5, **A–D** show deposition of the thin film, e-beam resist, patterning, and etching of the nanowire area. **E–J** shows the ‘etch’ method of creating nanoantennas, using silver instead of gold: photoresist is spun and patterned by photolithography creating the spacer layer, silver and e-beam resist are deposited and the resist negatively patterned, lifted-off, and then the antennas etched. Finally, as before, **K–M** shows patterning the wide meanders at the end of the nanowire by photolithography and etching, and **N–R** shows deposition of thick NbN for use as bond pads, plus the final step depositing a capping layer of 85 nm of  $\text{SiO}_2$ .

was somewhat undesirable an outcome, and might be considered a serious flaw with the lift-off process.

Following the nanoantennas, another layer of AZ 5206E photosensitive resist was spun and the device was exposed to UV light through a mask, to pattern the co-planar waveguides. The developed device was exposed to  $\text{CF}_4$  RIE, removing the NbN (**K–M**). A third layer of photoresist was deposited and the detector was exposed again, this time to deposit the bond pads. A thick layer of NbN was then sputtered, and the device underwent lift-off (**N–Q**). Finally, the full detector was coated in thin 75 nm layer of  $\text{SiO}_x$  to protect it (**R**).

### 3.2.2 Silver etch method

After initial testing using the gold lift-off process, a new process was devised. The move to silver for the nanoantennas was made as gold was considered too easy to accidentally remove and silver’s properties are comparable: simulation of the antenna resonances shift only tens of nanometres with this change, keeping antennas that would be telecoms-wavelength-resonant when made of gold within the telecoms band when made of silver.

The nanowire is patterned as before (figures 3.6**A–D**). Diversion from the lift-off process occurs for fabrication of the nanoantennas: for making the spacer layer and antenna (**E–J**)  $\text{SiO}$  and Ag is deposited across the whole substrate. A layer of hydrogen silsesquioxane (HSQ) is deposited, and the film undergoes negative e-beam lithography, so patterning the area around the antennas. This is developed and removed, leaving HSQ over the nanoantennas. This is then etched with an electron cyclotron resonance (ECR) etch to remove the silver film. The remainder of the fabrication then proceeds as with the lift-off process, shown in figures **K–R**.

## 3.3 SNSPD-on-DBR fabrication process

The fabrication process for SNSPDs on a  $\text{GaAs}/\text{Al}_{0.8}\text{Ga}_{0.2}\text{As}$  DBR is different from previous fabrications in that a commercial company, STAR Cryoelectronics, New Mexico, USA, deposited the thin film. The DBR was fabricated by collaborators at the University of Sheffield. The detector was fabricated by group member Robert Kirkwood at the University of Glasgow.

Epitaxial growth of GaAs DBRs commonly leads to artefacts called oval defects[112], which depend on a variety of environmental factors as well as the Al content of  $\text{AlGaAs}$ [113]. Several of these defects occurred on the DBRs fabricated, as seen in

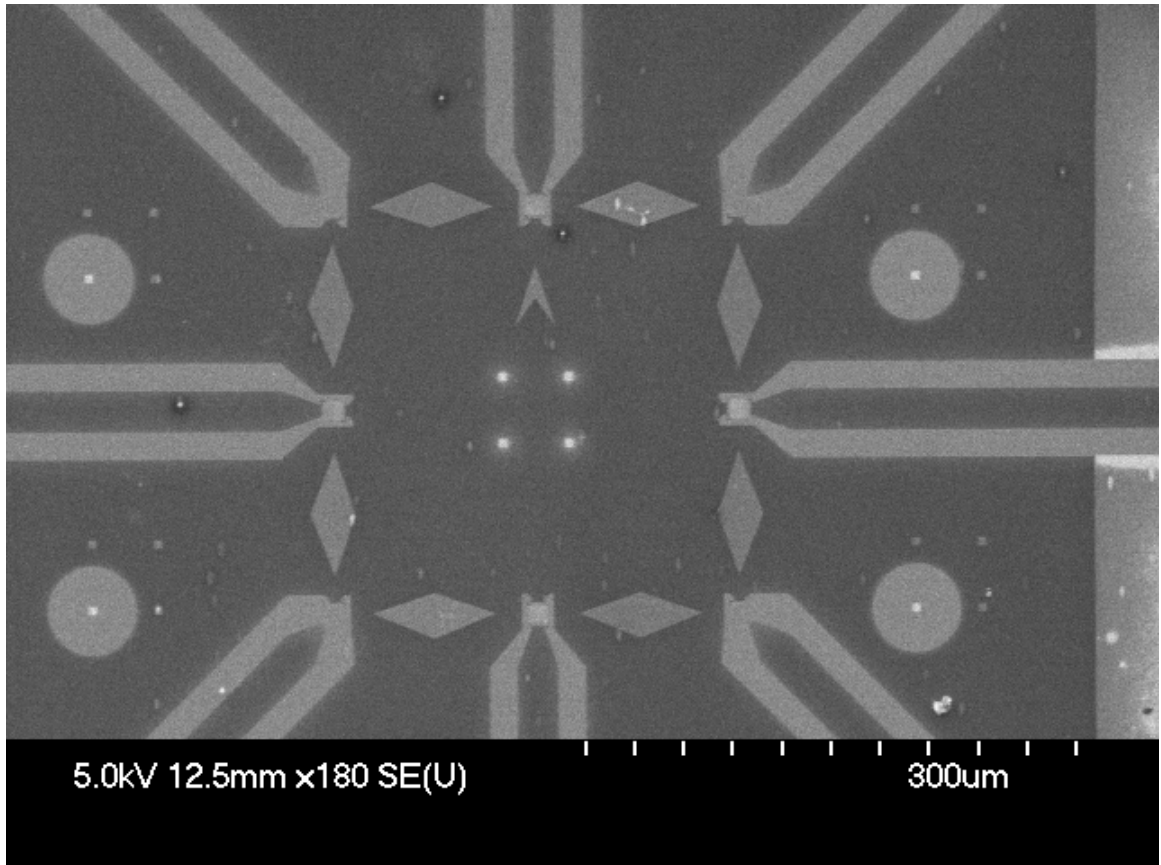


Figure 3.7: SEM image of a completed SNSPD on a GaAs/Al<sub>0.8</sub>Ga<sub>0.2</sub>As distributed Bragg reflector (DBR). Oval defects are clearly visible in the co-planar waveguide to the left, and to the top of the image. Image courtesy of Robert Kirkwood, University of Glasgow.

an SEM of one of the completely-patterned SNSPDs, shown in figure 3.7, where they appear as white spots surrounded by a dark region.

The procedure for patterning the film is as follows. Firstly, the substrate is cleaned, to minimize oval defects as in figure 3.8A, then 30 GaAs/Al<sub>0.8</sub>Ga<sub>0.2</sub>As pairs are grown by MBE, shown in B. The thickness of each layer is determined by equation  $L_t = \lambda_0/4n$ , where  $L_t$  is the thickness,  $\lambda_0$  is the wavelength in vacuum of the wavelength intended to achieve highest reflection, and  $n$  is the refractive index of the material being deposited. The DBRs were designed for  $\lambda_0 = 1550$  nm, so for GaAs  $L_t = 114.9$  nm and for Al<sub>0.8</sub>Ga<sub>0.2</sub>As  $L_t = 128.4$  nm. Once these layers were grown, a  $L_t = \lambda_0/2n$  layer was grown, to allow the NbTiN film to be deposited at the node. This was then performed by STAR Cryoelectronics, where 8 nm NbTiN films were sputtered, shown in C.

To pattern the gold features (bond pads and alignment marks) 110 nm ZEP 520 A positive-tone e-beam resist is deposited, D. The e-beam, from a 100 keV Vistec VB6 UHR EWF, is raster-scanned across the resist, shown in E. This is developed with 100 % o-Xylene for 60 s at 23 °C; the device is then rinsed in IPA for 60 s. 10 nm of titanium and 70 nm gold are then evaporated on by e-beam evaporation in figures 3.8F-G, and the remaining resist and deposited metals undergo lift-off using Shipley Microposit

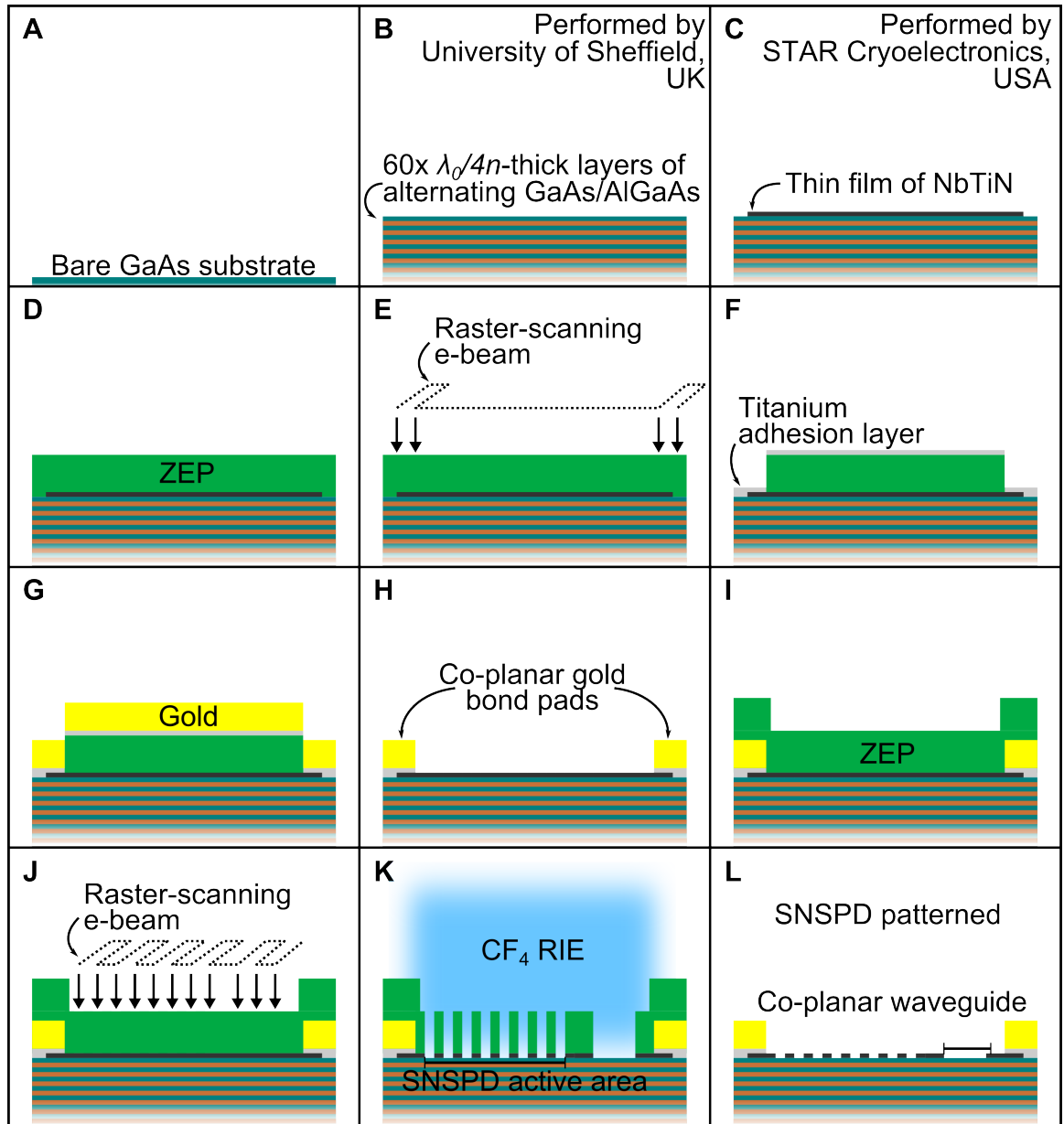


Figure 3.8: Process used to fabricate SNSPDs on a DBR substrate. The substrate was cleaned (A) and sent to the University of Sheffield for DBR deposition. 30 pairs of GaAs/Al<sub>0.8</sub>Ga<sub>0.2</sub>As layers were grown by molecular beam epitaxy (MBE) (B). These have a thickness of  $\lambda_0/4n$ , where  $\lambda_0$  is the design wavelength and  $n$  is the refractive index of the material. As the DBRs are designed for  $\lambda_0 = 1550$  nm the thicknesses are 114.9 nm for GaAs and 128.4 nm for Al<sub>0.8</sub>Ga<sub>0.2</sub>As. Finally, two half-wavelength layers were deposited, to ensure there is a node where the SNSPD will be fabricated. The films were then sent to STAR Cryoelectronics for NbTiN thin film deposition (C) and returned to the University of Glasgow. A layer of ZEP was deposited (D) and an e-beam was raster-scanned across, patterning the alignment marks and bond pads (E). The resist was developed and a Ti adhesion layer was deposited (F) followed by 70 nm Au (G) so completing the co-planar bond pads (H). A second layer of ZEP resist was applied (I) and this was patterned by e-beam (J), developed and placed in a CF<sub>4</sub> RIE (K) so patterning the nanowire and co-planar waveguides (L), thus completing the detector fabrication.

remover 1165 by soaking overnight at 50 °C, followed by 30 s in an ultrasonic bath, and an acetone rinse, followed by a final rinse in IPA. The final result is shown in **H**.

To pattern the SNSPD, another 110 nm layer of ZEP 520 A is deposited, exposed, and developed, figures 3.8**I-J**. Once prepared, the patterned chip is put in a CF<sub>4</sub> RIE for 50 s at 80 W, so patterning the SNSPD and coplanar waveguide into the NbTiN, seen in **K**. The remaining resist is stripped off with the lift-off procedure used before, and the SNSPD on DBR is complete and ready for testing, as in **L**.

### 3.4 Closed-cycle cryostat layout and operation

Superconducting devices must be cooled to below their transition temperature in order to function. As covered in section 2.3, liquid helium ( $T_{boil} = 4.2$  K) would seem an obvious cryogenic solution: low vibration (no moving parts) and 4 K to 10 K below the transition temperature of NbN thin films[82]. However, liquid helium is expensive and finite: running certain experimental procedures, such as high-resolution spatial maps of the system detection efficiency (SDE), can take a full day. Subsequently, closed-cycle cryostats, though more mechanically noisy, are more useful.

As described in detail in section 2.3, operating on the same principle as a domestic refrigerator, a closed-cycle cryocooler is a heat pump theoretically capable of reaching (in the case of the CryoMech PT403[92] used in the setup shown in figure 3.9) 2.8 K. A water-cooled compressor cycles high-purity helium at a high pressure through a heatsink within a vacuum chamber. Thermal energy from the heatsink flows into the cooler gas, the gas is pumped out, raised to high pressure again, and the excess heat is transferred to water at room temperature, before the gas is cycled back through. This system has the advantage of only requiring electricity and water, the helium itself being contained internally, and requires no handling of cryogenics, and thus can be run for long periods of time uninterrupted.

The internal structures within the cryostat are, where good thermal conduction is required, made from oxygen-free, high thermal conductivity (OFHC) copper. This is coated with a thin layer of gold, to improve reflectivity and in turn reduce absorption of black-body radiation from the higher-temperature stages.

Such a setup has the potential to be highly vibrational, however: there is a motor that alternates which gas line is connected to the heatsink, and the compressor is very mechanically noisy. Previous Gifford-McMahon (GM) refrigerators used by the group, though giving good results with the microscope, suffer extra noise when running sensitive optical scans because of this vibration. The effect of this mechanical noise and justification for the need to suppress it is described in detail in section 3.12.2. To

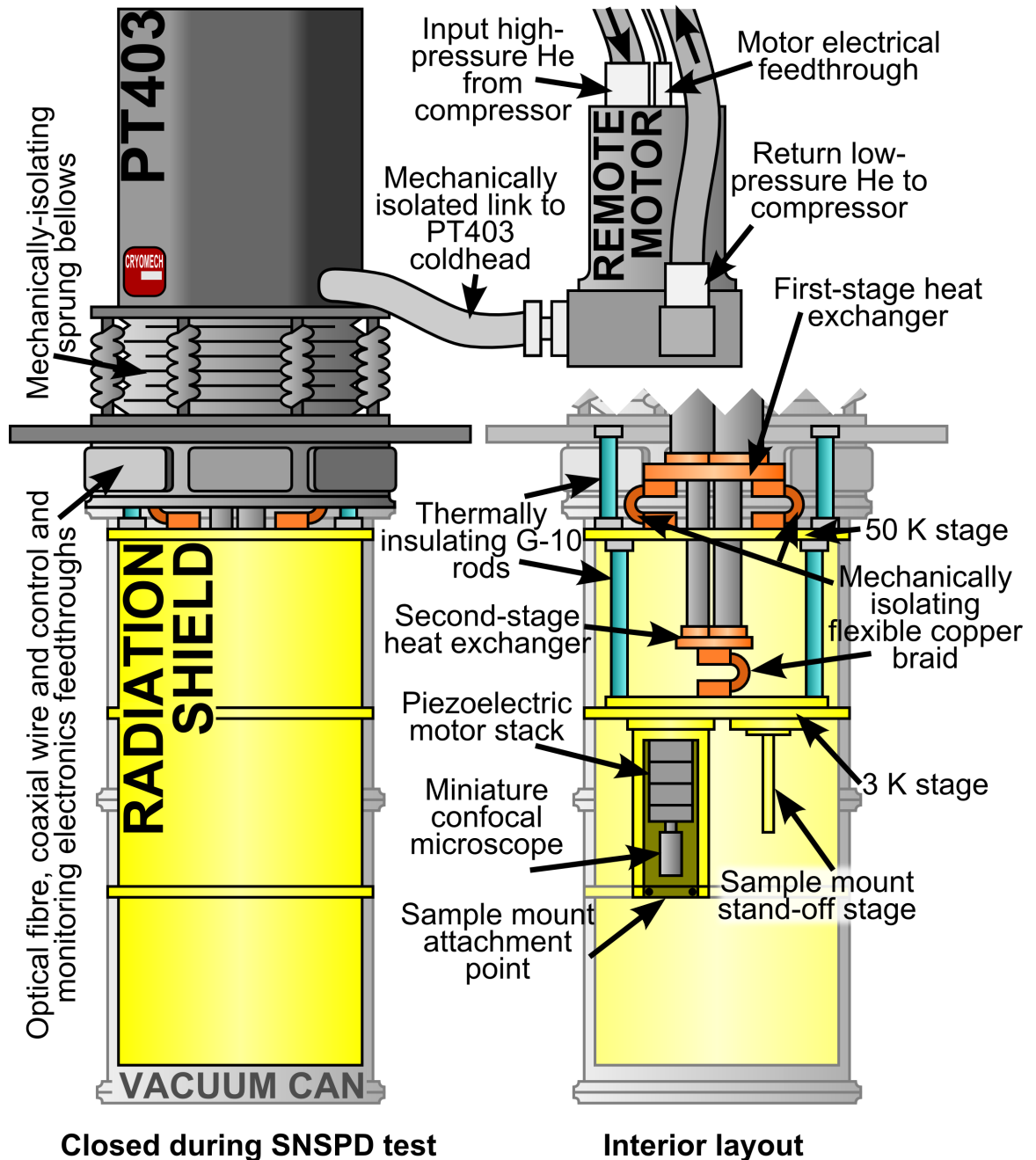


Figure 3.9: Diagram of the setup of the cryostat for nano-optical testing: high-pressure, 99.999%-purity He arrives at the remote motor from the compressor. This is inserted through a flexible linking gas line to the PT403-RM cold head, which is mounted on sprung bellows, damping its vibration. The gas is pumped through the copper heat exchangers, the first with a measured base temperature of about 50 K, and the second with a measured base temperature of around 3 K. The specific base temperatures are dependent on the heat load and vary with experiment. The gas is then returned through the remote motor and out down the low-pressure gas line back to the compressor. The heat exchangers are connected thermally to the interior structure of the refrigerator by flexible copper braids, preventing vibration from the cold head transferring to the miniature confocal microscope setup. Rods of G-10 polymer thermally isolate the stages from each other and the outside, while a gold-coated aluminium radiation shield reflects incoming black-body radiation. Fibre and electrical input to the cryostat occurs through hermetically-sealed feedthroughs built into panels at the top of the vacuum can. Internal electrical cabling for SNSPD readout, temperature monitoring, and piezoelectric motor control is thermally anchored to the 50 K stage and the 3 K stage, the two anchor points being separated by a length of wire to limit the heat load at 3 K.

isolate this, in the system shown in figure 3.9, the motor is separated and connected by a short high-pressure line, meaning the PT403 is isolated from it, and the vacuum chamber is seated on anti-vibration matting. Additionally, the PT403 itself has no moving parts to cause vibrations itself, and has dampeners to lessen any transferred to it.

The system used has two internal stages, one at 50 K, the other at around 4 K. The vacuum chamber and radiation shield prevent conduction and black-body radiation from the outside from heating the internal stages.

### 3.5 Screening detectors for functionality

In order to determine which detectors would not work and narrow the number to be optically tested down, which has a significant time cost, most devices were subject to a screening process. This approach was applied to detectors from all collaborations, but was used most extensively on samples from Cambridge, which were fabricated frequently, in a tight feedback loop. On the order of a thousand separate SNSPDs were eligible for testing during the course of my work, so it was important to have a streamlined process. This procedure went as follows.

1. Devices' resistances were tested at room temperature. This was scaled to an area calculated by squaring the width of device, to give a measure known as the 'square resistance'.
2. Devices with too high a square resistances, suggesting an incomplete circuit, or too low a square resistance, suggesting a short, were rejected. The remainder were placed in a closed-cycle cryostat and cooled to around 3.5 K (depending on the thermal load) in the closed-cycle cryostat 'Kelvinator', and their critical currents were determined.
3. Devices with poor critical currents (I-V characteristics suggesting a series resistance, or offering too low a signal-to-noise ratio) were filtered out. The remainder were connected up to an oscilloscope and biased just below their critical current see whether dark counts could be observed.
4. Devices that showed no measurable pulse were filtered out.
5. The best devices for pulses were taken out of the closed-cycle cryostat and either fibre-coupled or more often placed in the miniature microscope setup. These could be optically tested, and have efficiency and jitter measurements taken.
6. Devices that functioned well electrically and optically were used in the experiments described in later chapters.

### 3.6 Basic electrical characterisation

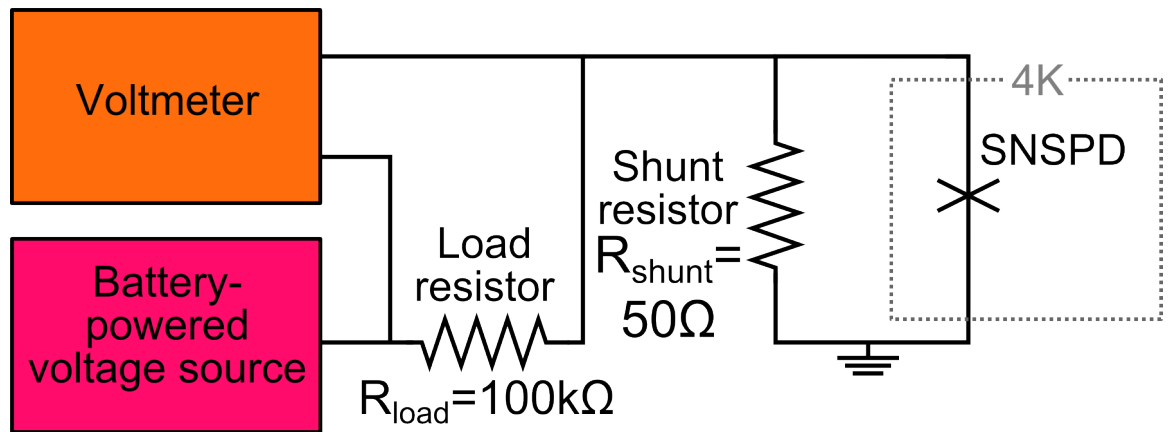


Figure 3.10: Diagram of the setup for an I-V measurement with shunt resistor: a voltmeter records the output and measured voltage of the circuit. The shunt resistor allows the SNSPD to reset after triggering, leading to higher critical currents. If the device has a high resistance even when superconducting, the shunt may be disconnected to prevent it shorting the SNSPD, at the expense of having to computationally reset the detector once triggered.

A key property of an SNSPD is its critical current  $I_C$ , which is the current the detector can support before the superconducting nanowire becomes resistive. This can be measured quickly and instructively using basic electronic components: a voltage source, voltmeter, and two resistors, as seen in figure 3.10. Though ultimately connected to a computer system for measurement automation, alternately-charging batteries are used as the voltage source  $V_B$  to ensure a steady, noise-free output. This is delivered from a Stanford Research Systems Simple Instrumentation Module SIM 900 mainframe with SIM 928 Isolated Voltage Source module. A load resistor  $R_{load}$  defines the current supplied to the SNSPD by equation  $I_B = V_B/R_{load}$ : typically  $100\text{ k}\Omega$  is used. The voltage  $V_B$  is swept by computer program across a range of bias voltages such that its maximum bias value  $I_{B,max} > I_C$ . From this, the critical current  $I_C$  can be determined by measuring the output voltage  $V_{out}$ , as shown in figure 3.11.

In order to allow an SNSPD device to relax back to its superconducting state once triggered, it is (when any intrinsic resistance is sufficiently small such that  $R_{series} \ll 50\ \Omega$ ) set up in parallel with a  $50\ \Omega$  ‘shunt’ resistor as shown in figure 3.10, with a resistance greater than the device when superconducting, but less than the device when resistive. When the device is triggered its resistance  $R \gg 50\ \Omega$ . Subsequently, the majority of the current is redirected through the shunt resistor, the heat in the nanowire dissipates as the resistive region is no longer being heated by current flow, and the device returns to its superconducting state and can detect again.

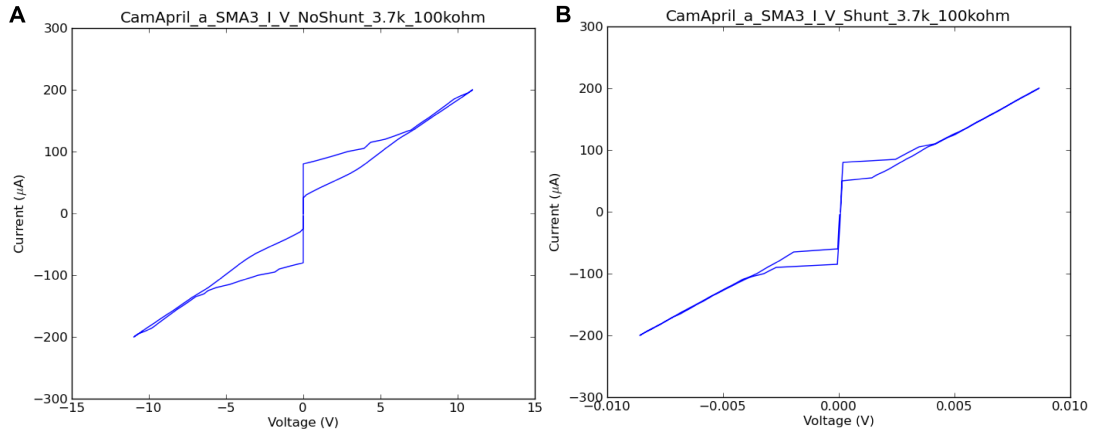


Figure 3.11: Graphs of typical output from the I-V measurement program. **A** shows the current-voltage characteristic when there is no shunt resistor. **B** shows the same detector when a  $50\ \Omega$  resistor is connected in parallel. The detector becomes resistive at the point where the applied current results in a measurable voltage output.

### 3.6.1 Noise analysis

Noise sources in a sensitive electronic system such as the bias and readout circuitry are important to understand and minimize. Noise in the load resistor will lead to a noisy bias current, which would lead to a variable dark count rate as this is dependent on bias. Looking at Johnson-Nyquist noise[114] in the bias circuit, we have a noise current  $I_{B,noise}$  of

$$I_{B,noise} = \frac{V}{R_{load}} = \sqrt{\frac{4k_B T \Delta f}{R_{load}}} \quad (3.1)$$

where  $k_B$  is the Boltzmann constant,  $T$  is the absolute temperature,  $\Delta f$  is the bandwidth, and  $R_{load}$  is the load resistance. At room temperature and across the pass band of the amplifiers typically used (RF Bay LNA-580), the noise current  $I_{B,noise} \approx 10\ \text{nA}$ . For typical detector systems tested,  $I_B$  was in the range  $5\ \mu\text{A} \leq I_B \leq 30\ \mu\text{A}$ : so we see that Johnson-Nyquist noise contributes to a 0.2% to 0.03% variation in the applied  $I_B$ .

With regards to noise introduced from the amplifier chain, the typical amplifiers used, RF-Bay LNA-580 and LNA-1000, have a noise figure of 0.7 dB on an amplification of 23 dB and a noise figure of 2 dB on an amplification of 33 dB respectively. The noise figure represents the noise added to the system by the component, and is calculated as the ratio of two signal-to-noise ratios (SNRs):  $NF = 10 \log_{10}(\text{input SNR}/\text{output SNR})$ . As such, the SNR across the LNA-580 would typically reduce by 15%, and across the LNA-1000 by 37%.

As discussed in detail in section 3.12.3, because the critical current  $I_C$  is dependent on temperature, the thermal oscillations of the cryostat (around 10% of the base temperature) result in a variation in the dark count rate. This can vary by 10 dB over

the course of a single pulse of the cryostat. For this reason, for the detection circuitry used with the ‘Kelvinator’ closed-cycle cryostat, lower-noise amplification technologies such as low-temperature amplifiers and bias circuitry are not the bottleneck in this system, as thermal oscillations and dark count rate are significantly more limiting.

### 3.7 Parallel wire device operation

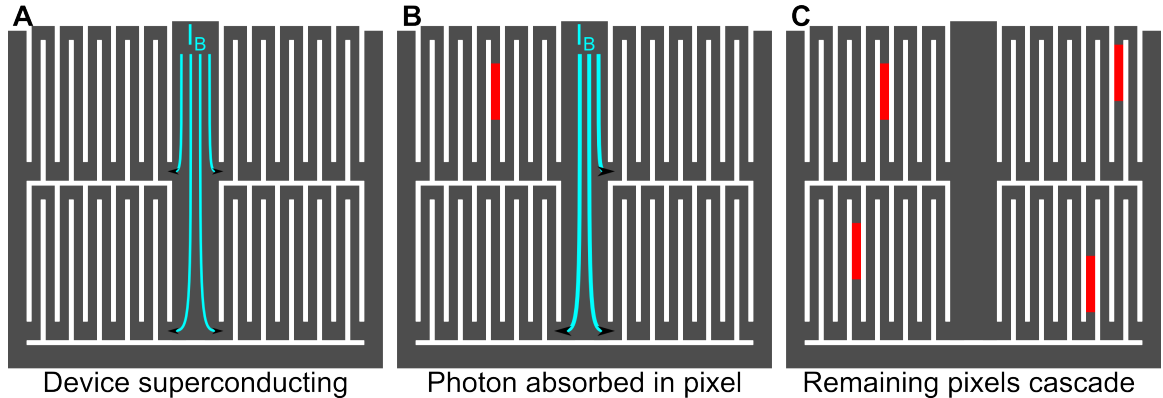


Figure 3.12: Diagram of parallel-wire SNSPD device cascade switching principle. The device splits into four individual pixels, each with a share of the total bias current  $I_B$  (A). When a photon hits one pixel, a resistive region is created that increases the current density around it to above the critical level, rapidly creating a resistance across the whole wire (B), as in meander SNSPD operation. This diverts more of the initial bias current  $I_B$  through the other wires, pushing them above their respective critical currents  $I_C$  and rapidly cascading them into resistive states (C). The current is then diverted through the shunt resistor and the detector relaxes and resets.

Devices were fabricated following the parallel-wire fabrication process detailed in section 3.1. These detectors are geometrically different to the simple meander shown in figure 2.5A, as can be seen in figure 3.2, and have a different operating principle. This geometry allows multi-photon discrimination, and a larger SNR. Figure 3.12 depicts diagrammatically the method of operation. As the pixels are in parallel, the total bias current  $I_B$  is the sum of the individual bias currents through each pixel, leading to increased output pulse heights (since  $V_{out} = I_B \cdot 50 \Omega$ ).

### 3.8 Wire bonding and sample mounts

In order to cool a device in the closed-cycle cryogenic refrigerator, the devices must be mounted to something. A sample mount was designed alongside the cryostat for easy mounting of devices both simply within the system and when fibre-coupled.

The sample mounts consist of a gold-coated OFHC copper base, four electrically isolated bond pads, a central adhesion area, and a cap. Devices are attached to the central

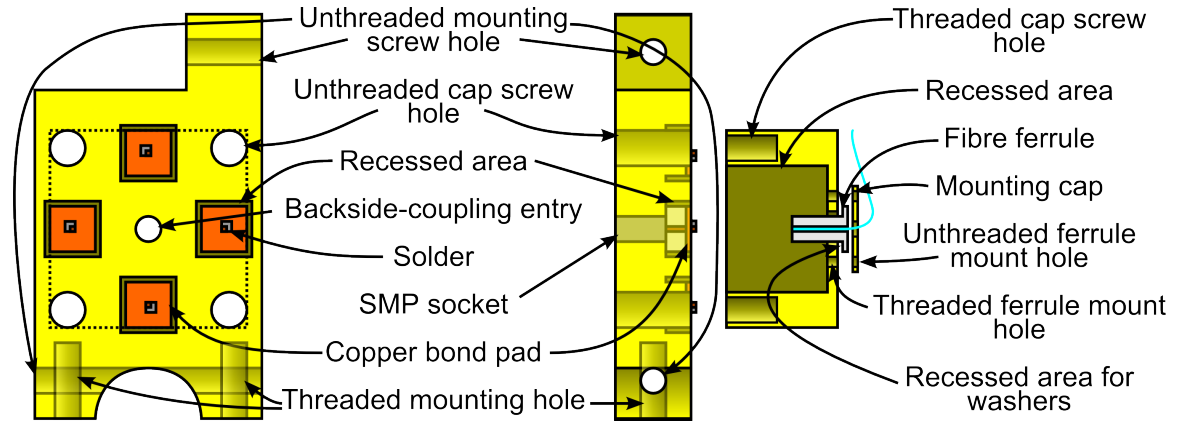


Figure 3.13: Diagram of the standard detector sample mount layout, viewed from above and from the side, with profile of fibre-ferrule cap. The sample mount may be attached through top and bottom unthreaded mounting screw holes to the miniature confocal microscope, or through the threaded mounting holes at the bottom to a stand-off stage. Four copper bond pads mounted on an insulating layer act as wire-bond-friendly electrical inputs to the detector, and connect by solder to a pin sticking out from an SMP socket. The cryostat's SMP plugs are able to be easily attached to these sockets from the backside of the mount. A hole beneath the mounting area allows backside-coupling of the detector should this be desired. The unthreaded cap screw holes allow screws to attach the cap to the sample mount base, affixing to the threaded cap screw holes. This allows accurate fibre-coupling of SNSPDs in a neatly packaged format. Washers are used to set the spacing between the end of the ferrule and the SNSPD.

adhesion area using varnish, which is sufficient to survive a small number of thermal cycles. The adhered device then has wires attached from the gold on its surface to copper bond pads, which are soldered to macroscopically-accessible SMP sockets. This setup is shown in figure 3.13.

A Kulicke & Soffa model 4123 Al wedge wire bonder was used to connect the devices to the bond pads.

To protect the device in the sample mount, a cap, which may also be used to mount a fibre ferrule, may be screwed over it. The height of the fibre ferrule relative to the detector can be adjusted using 25  $\mu\text{m}$  steel washers. Optical coherence tomography (OCT) measurements described in section 3.8.1 allow the distance between the end of the ferrule and the device to be measured. The majority of detectors were optically tested in the miniature microscope setup however, as because the optical spot may move it is capable of testing up to four detectors per chip in a single cycle of the cryostat.

A modified, thinned sample mount was used when optically testing backside-coupled detectors with a fibre, as the reduced focal length would make alignment through the standard mount's backside-coupling entry impossible. This was only used when testing Configuration I detectors in a tunable cavity, described in Chapter 6.

### 3.8.1 Optical coherence tomography

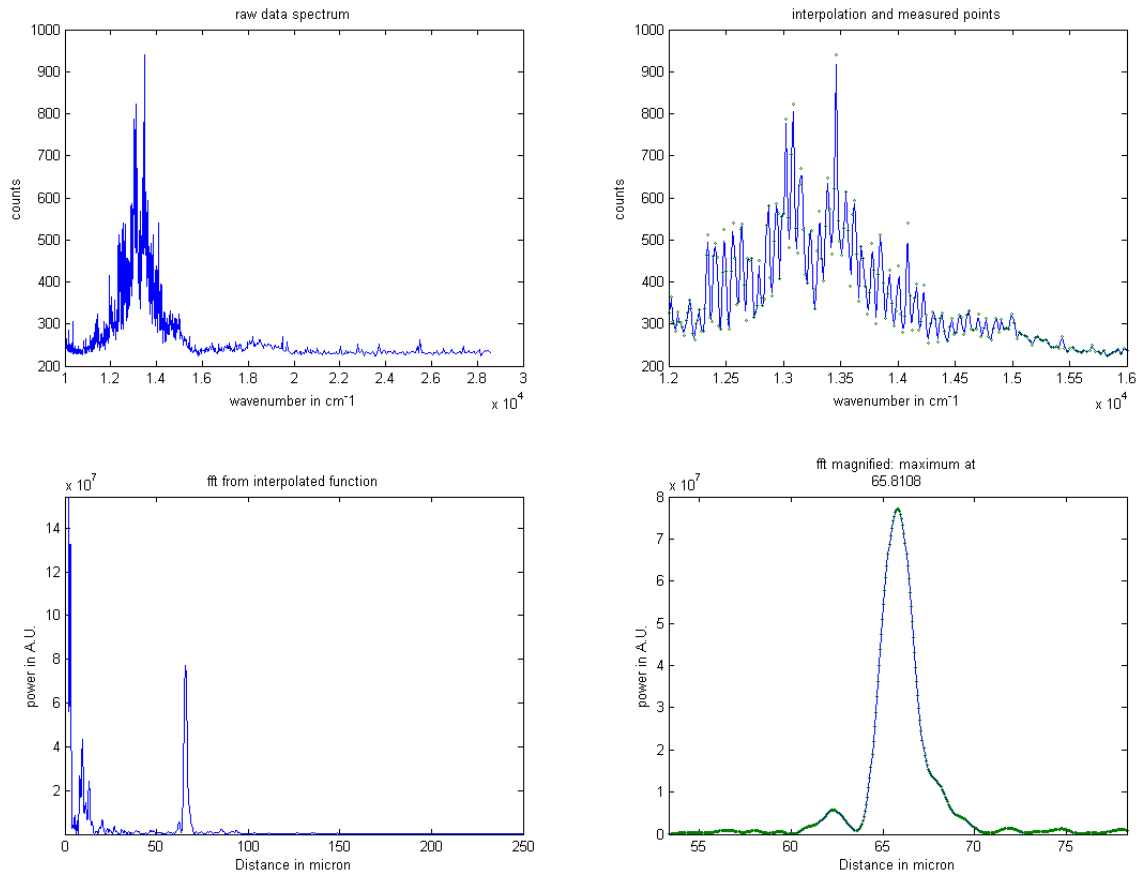


Figure 3.14: Graph of typical output of the OCT setup. Top-left is the raw data from the spectrometer. Top-right is a subset of the raw data, interpolated. The fast Fourier transform (FFT) is shown bottom-left: there is a clear peak at 66  $\mu\text{m}$ . This peak is selected and magnified bottom-right.

In order to position a fibre ferrule sufficiently near to an SNSPD it is useful to have some method of measuring the distance between the end of the fibre ferrule and the detector itself, to prevent collision. OCT can be used for this purpose. The system used in the Quantum Sensors group, designed by Martin Härtig[115], pairing an Ocean Optics Red Tide USB-650 spectrometer (range 350 nm to 1000 nm) with a white light source. Frequency-domain OCT is performed by taking a FFT of spectrum of the reflected signal: it becomes possible to tell which frequencies are constructively interfering at that distance, and so determine the cavity length. This is determined using the equation

$$d_{gap} = \frac{c}{2n\Delta f} \quad (3.2)$$

where  $c$  is the speed of light,  $d_{gap}$  is the gap distance between the end of the fibre and the surface of the detector,  $n$  is the refractive index of the medium (generally air or vacuum), and  $\Delta f$  is the change in frequency between constructive interference peaks in the frequency. This was used when fibre-coupling detectors in the above system to

ensure good coupling efficiency. It was also used to confirm cavity lengths when tuning a cavity.

### 3.9 Kinetic inductance

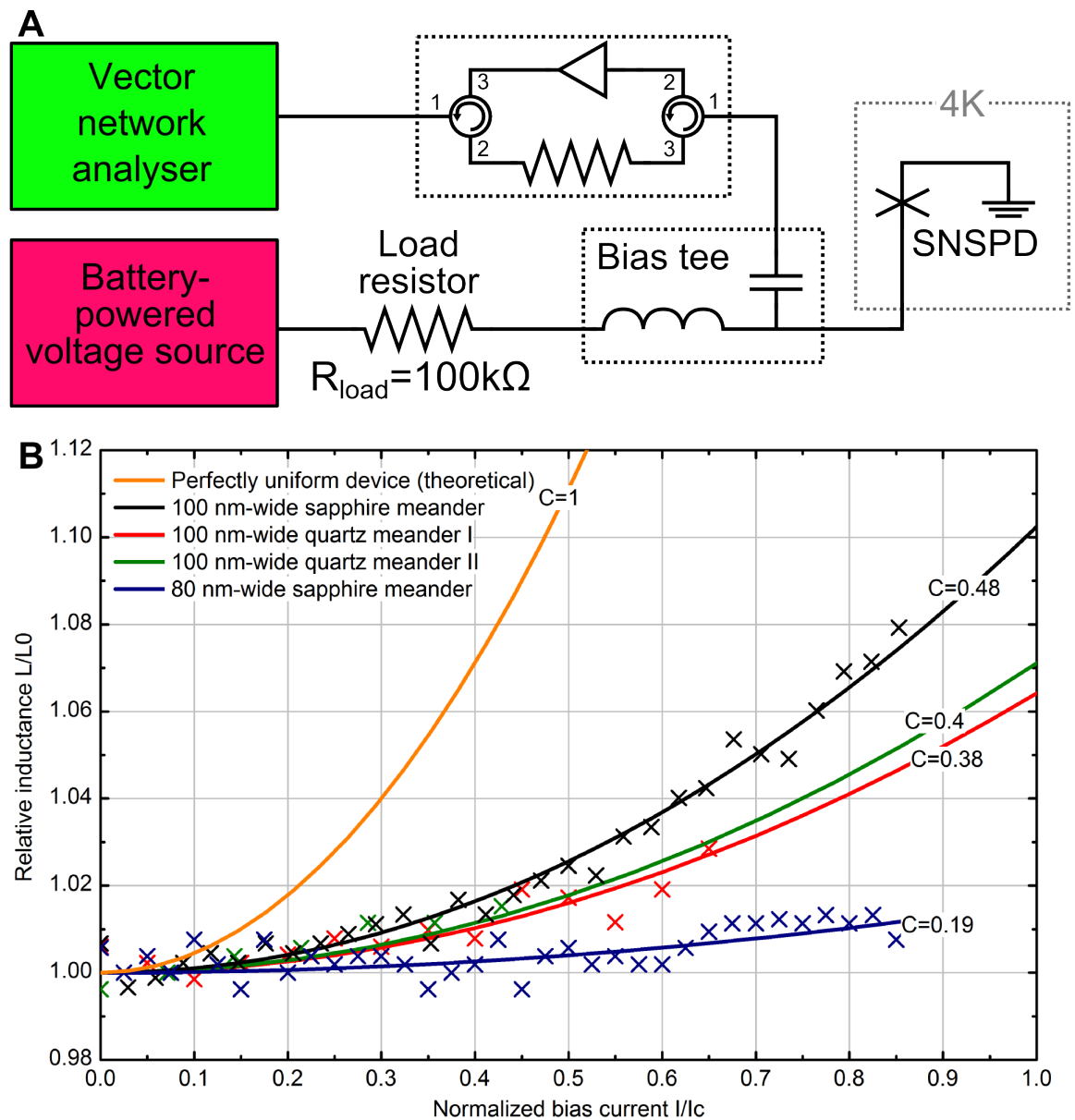


Figure 3.15: A diagram of the circuit used to measure the kinetic inductance and a graph of typical output. **A** shows a diagram of the system required to test the kinetic inductance of an SNSPD. Circuitry was used to allow a single-port vector network analyser (VNA) to operate as though it were two-port. This was optimised to reduce error. The circuitry attenuates VNA output to a level that will not overwhelm an SNSPD and re-amplifies the signal on the return. **B** shows a theoretically perfect device ( $C = 1$ ) shown alongside several experimental results, from the best Cambridge meander device tested ( $C = 0.48$ ) to the worst ( $C = 0.19$ ). These detectors were tested as part of a feedback loop prior to fabrication of the parallel-wire SNSPDs fabricated at Cambridge.

Measurement of the kinetic inductance has been shown to yield a measure of the uniformity of a device[69]. Further to this, the kinetic inductance determines the relaxation time of detection event pulses in an SNSPD. Measurements of the inductance of superconducting devices were carried out using a computer-controlled vector network analyser (an AEA VIA Bravo), the circuit setup shown in figure 3.15A, with frequencies of 0.1 MHz to 50 MHz. By changing the bias and applying across the device the sum of the output of the analyser and bias, it is possible to record what happens to the inductance as the device approaches its critical current.

$$\frac{L_K}{L_{K,0}} = 1 + \frac{4}{9}C^2 \left( \frac{I}{I_C} \right)^2 \quad (3.3)$$

These data can be normalised and a curve following equation 3.3 can be fitted, with inductance  $L_K$  at a given  $\frac{I}{I_C}$ . In this, the parameter  $0 \leq C \leq 1$  used to adjust the fit. This  $C$  value is the measure of uniformity: a completely uniform device has  $C = 1$ , as shown in figure 3.15B.

### 3.10 Detection efficiency

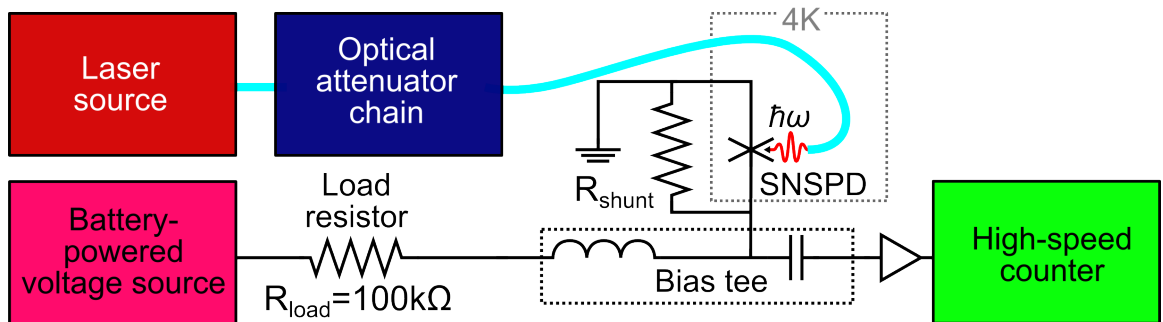


Figure 3.16: Diagram of the setup for a detection efficiency measurement. The laser source may be a pulsed 1550 nm laser diode with a pulse duration  $\approx 1$  ns, or the continuous wave (CW) 1340 nm to 1650 nm tunable laser setup described later. This laser source is fed through an optical attenuator chain comprised of two calibrated programmable optical attenuators in series, with 130 dB total applicable attenuation.

The detection efficiency is measured by comparing input power with the number of counts per second registering on the detector. The energy of a photon is  $E = \hbar c/\lambda$  and the wavelength of the input light is known, and the input power is measured using a power meter at the input to the cryostat when no attenuation is applied: divided by the energy of a single photon, this gives the number of photons per second entering the cryostat. To obtain a better profile of the system, the detector's bias current is varied from  $I_B > I_C$  to  $I_B \ll I_C$ , and a large range of input photon fluxes are measured. There are a given number of dark counts for any bias current: for single-wire SNSPDs,

and if the number of dark counts is much less than the detector count rate, these may be approximately accounted for by simply subtracting them. Subsequently, the ratio of input photons to number counted is the efficiency. The setup for this is shown in figure 3.16.

In literature, quoted efficiencies are sometimes corrected for the area illuminated by the light spot, the fill-factor of the meander, and other factors, and called the quantum efficiency (QE). Efficiencies quoted in this document are generally the SDE, which is the efficiency of the detector as experienced by the end-user, including losses from the system.

To calculate the SDE  $\eta$  from the system in figure 3.16, fitting to each dataset taken is performed. The fitting performed depends on whether the input laser is pulsed or CW[21], but is broadly defined as the detected count rate divided by the input count rate,

$$\eta = \frac{R_{detected}}{R_{input}}. \quad (3.4)$$

### 3.10.1 Pulsed laser system detection efficiency

By looking for the probability of at least one successful event on a detector of efficiency  $\eta$  for a mean number of  $\mu$  input photons, we can define  $R_{detected}$  for a single-wire detector illuminated by a pulsed source as being

$$R_{detected} = f (1 - (1 - \eta)^\mu) \approx f (1 - e^{-\mu\eta}), \quad (3.5)$$

where  $f$  scales the result by the laser pulse frequency. Operation in this regime requires that the input pulse period is significantly longer than the reset time of the detector  $\tau$ :  $f \ll 1/\tau$ . This allows the detector to relax back to the superconducting state between detection events, preventing the arrival of a photon during the detector dead time. Helpfully,  $\tau$  is generally on the order of nanoseconds for SNSPDs, so a 1 MHz frequency laser allows 100 to 1000 times the detector reset time.

Consideration of the dark count rate  $D$  of the detector is important.  $D$  can be determined by looking at the count rate of the detector when  $R_{input} = 0$ . If  $D$  is sufficiently low compared with  $R_{detected}$  and  $\tau$  there will be very little interaction between actual detection events and dark counts, so  $D$  can simply be subtracted from  $R_{detected}$  in equation 3.5. Since we know that the input photon flux will be

$$R_{input} = \mu f \quad (3.6)$$

then we are able to obtain the efficiency  $\eta$  by equation 3.4. A typical plot using pulsed-laser fitting code is shown in figure 3.17.

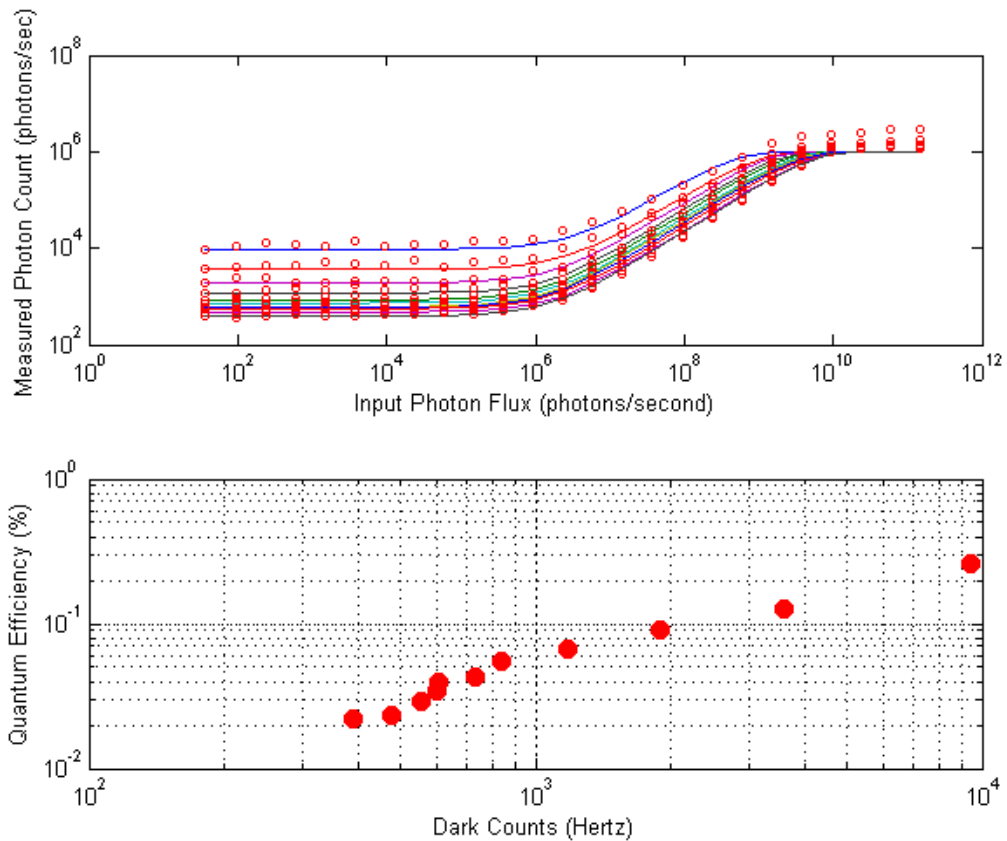


Figure 3.17: Typical output from the pulsed-source detection efficiency fitting program, written in Matlab by Chandra Mouli Natarajan. The top plot shows  $R_{input}$  against  $R_{detected}$ . Fitting theory to the data points with a least-squares fit, the efficiency  $\eta$  and dark count rate  $D$  is determined at each bias point. The bottom plot shows  $D$  against  $\eta$ .

### 3.10.2 Continuous-wave system detection efficiency

For a CW laser source illuminating a single wire, the ceiling for  $R_{detected}$  is limited by the detector reset time rather than the pulse frequency. The mean photon number  $\mu$  per time interval  $\tau$  is then  $\mu = R_{input}\tau$ . For a Poissonian light source where  $\mu\eta \ll 1$ :

$$R_{detected} = \frac{1}{\tau} (1 - (1 - \eta)^\mu) \approx \frac{1}{\tau} (1 - e^{-\mu\eta}) \quad (3.7)$$

The likelihood of dark counts  $D$  interfering with photon detection is higher in this case as the detector does not have tightly-focused photon pulses. We can define the corrected count rate[21] as

$$R'_{detected} = \left( \frac{R_{detected}}{1 - R_{detected}\tau} - \frac{D}{1 - D\tau} \right). \quad (3.8)$$

By using this as  $R_{detected}$  in equation 3.4 and fitting the resultant equations to measured data with a least-squares fit we can obtain a value for the detection efficiency. A typical example of this output is shown in figure 3.18.

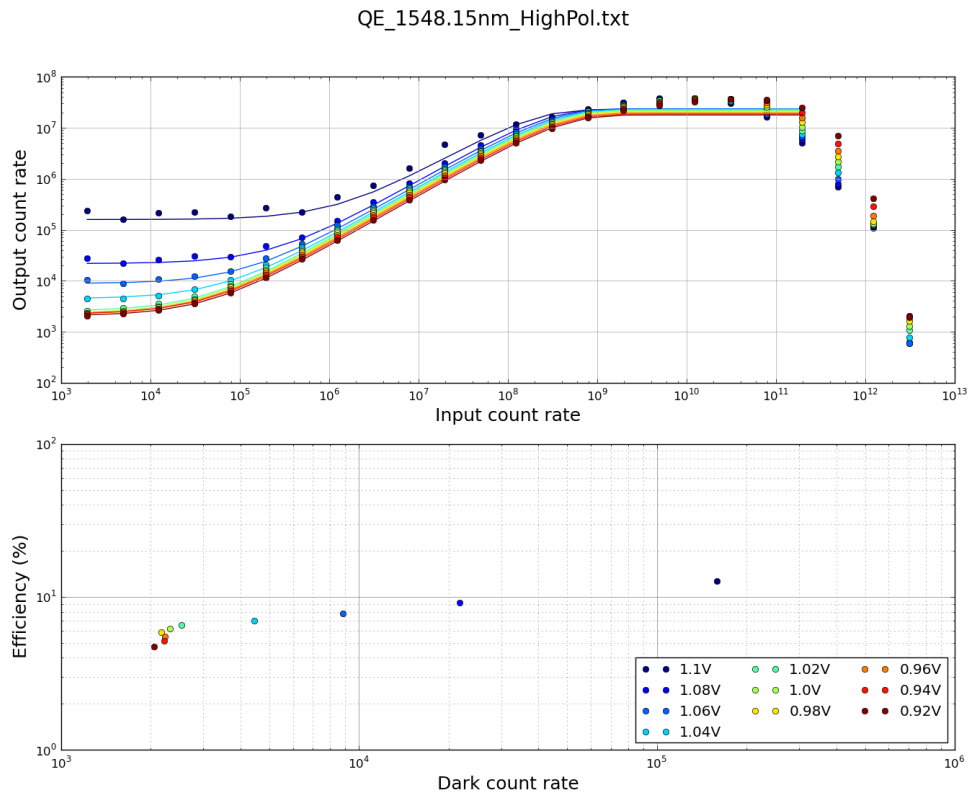


Figure 3.18: Typical output from the CW detection efficiency fitting program written in Python. The top plot shows  $R_{input}$  against  $R_{detected}$ . Fitting the theory to the data-points with a least-squares fit (and taking logarithms of both to ensure even weighting of fit at high and low  $R_{input}$ ), the efficiency  $\eta$  and dark count rate  $D$  is determined at each bias point. The bottom plot shows  $D$  against  $\eta$ . Unlike figure 3.17 at high  $R_{input}$  the detector can be totally saturated, so instead of capping off at source pulse frequency  $f$  is driven to the point it is unable to reset. This maximum frequency of operation is determined by the reciprocal of the reset time of the detector  $\tau$ . Subsequently, the final points are disregarded by the fitting algorithm, as the mathematical model it is fitting to does not describe this.

### 3.11 Detector timing jitter

The PicoQuant PicoHarp 300[118] and PicoQuant HydraHarp 400[119] are TCSPC electronics which perform gated detection of photons. By using a mode-locked 55 mW 980 nm laser to drive a Kphotonics CNT-1550-TK erbium-doped fiber laser (centre wavelength 1560 nm, spectral bandwidth 8 nm)[120] at 50 MHz, and splitting the output with a 50:50 beamsplitter, one may make a measurement of the timing jitter of an SNSPD. One output is used to trigger the TCSPC gating and the other runs to the detector, the output from this returning to the signal line of the TCSPC electronics. The setup for this is shown in figure 3.19.

SNSPD timing jitter, which is the variation in the arrival time of the pulse from the photodetector, can be measured using a TCSPC card. When used in combination with the miniature confocal microscope configuration, this can be used to create 2D maps

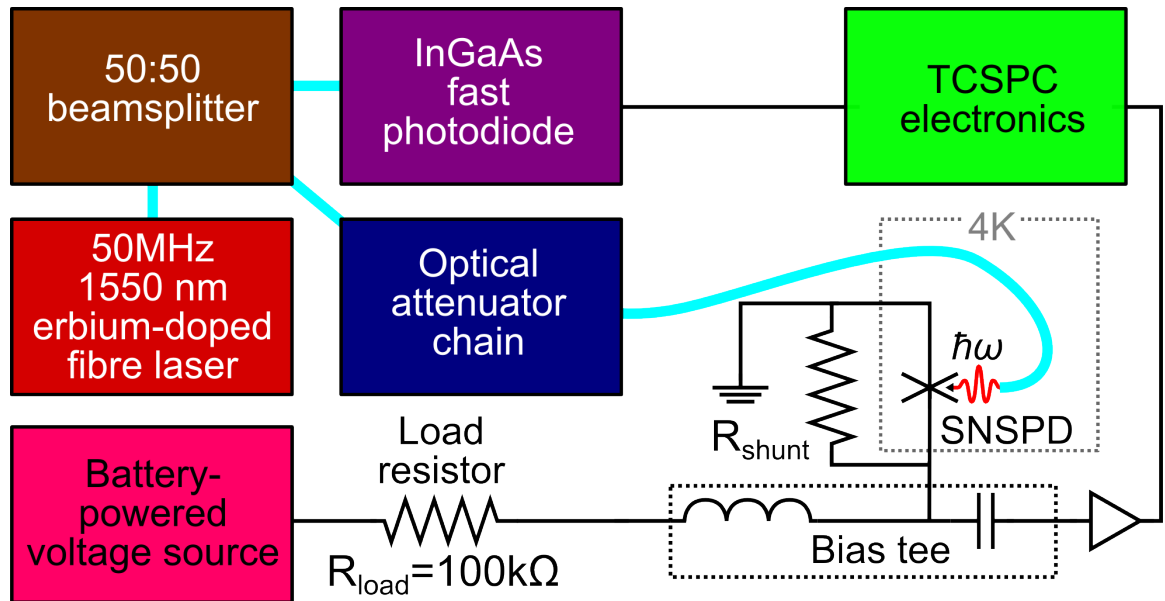


Figure 3.19: Diagram of the setup for taking a detector jitter measurement. A Kphotonics CNT-1550 50 MHz pulsed laser with picosecond pulse width is fed through a 50:50 beamsplitter. One output is routed to an InGaAs fast photodiode (intrinsic jitter 15 ps), which is wired into the time-correlated single photon counting (TCSPC) electronics' sync. The other output is sent through the attenuator chain and attenuated to the single photon level. This is then inserted into the cryostat. The output pulses from the SNSPD are routed through the bias tee and amplifier chain to the TCSPC input: when a pulse arrives, the TCSPC electronics record the time between the last sync pulse and the detection event. The TCSPC electronics, either a PicoQuant PicoHarp 300 (minimum 4 ps bin size) or PicoQuant HydraHarp 400 (minimum 1 ps bin size) generate a histogram of arrival times. For a single-wire SNSPD, the full-width at half-maximum (FWHM) of the peak of this histogram, which will be Gaussian, is the timing jitter. Parallel-wire detectors have a well-documented[74, 116, 117] tail in response which complicates definition of the jitter.

of jitter across the devices. If the arrival time of the signal is known, the SNSPD can be biased nearer the critical current and still detect efficiently by gating the detector readout, as many dark counts will occur when the counting electronics are turned off. The electronics stores the photon arrival time in bins of 1 ps or 4 ps depending on whether the HydraHarp or PicoHarp respectively is used, giving good resolution for arrival time and FWHM timing jitter measurements.

There are two modes of operation of a TCSPC card, forward start-stop and reverse start-stop mode. In forward start-stop mode, the device's gate is triggered by the reference pulses as described above. This has the advantage of measuring the time between the reference pulse and the event, but has disadvantages such as waiting for the device to 'time out' when a photon is not detected in that gate. In other TCSPC technologies this can be offset using reverse start-stop mode. In this mode of operation, the gate is opened when a photon arrives, and closes when the card sees the next reference pulse: as noted, this actually then measures the time between the event and the next reference pulse, however. The PicoQuant TCSPC technologies used here

are specifically designed to work efficiently in forward start-stop mode, circumventing the need for reverse start-stop mode.

### 3.12 Miniature confocal microscope configuration

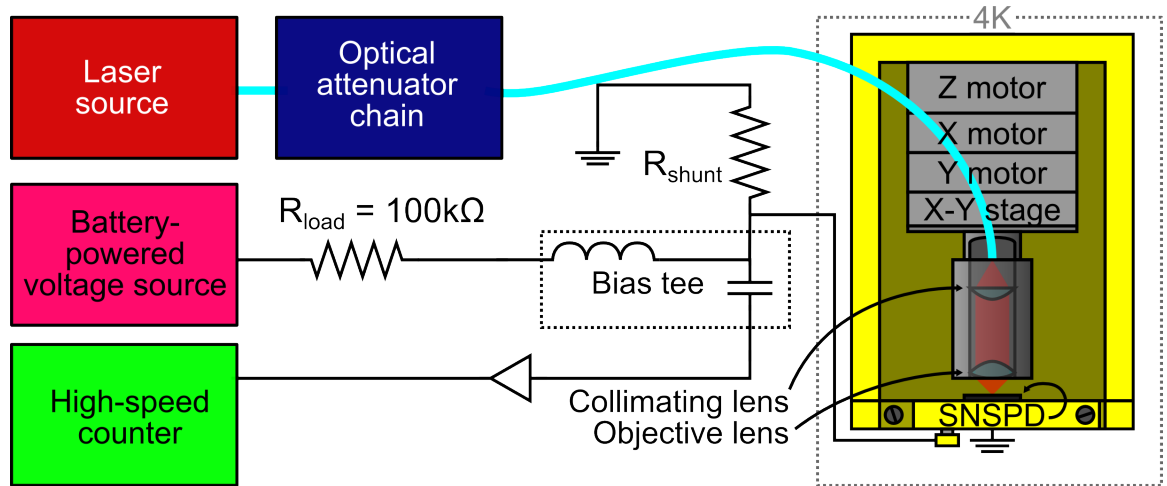


Figure 3.20: Diagram of the confocal microscope configuration: set up like this, the confocal microscope configuration can be used to scan a device to make an efficiency map. If the laser is swapped for the erbium-doped 1560 nm fiber laser, and the TCSPC electronics are connected, the system can be used to record a map of arrival time with position, also yielding a map of FWHM timing jitter.

Within the cryostat there is a miniature confocal microscope configuration setup[17, 18]. This is not used for confocal microscopy, but as a means of obtaining a tightly-focused spot for making spatial profiles of SNSPD response. It also permits testing multiple pixels in a single thermal cycle.

A stack of two Attocube ANPx101 piezoelectric motors give the setup 5 mm movement in X and Y, with an ANPz101 for Z movement. This gives the ability to focus the light to a point as well as translate this point across the device. The setup is shown in figure 3.20. This system can also make accurate, 40  $\mu\text{m}$ -by-40  $\mu\text{m}$  scans over the device with sub-nanometre step size[121] through an independent X-Y stage, an Attocube ANSxy100. This range is verified in figure 3.21.

Light delivered by the fibre is collimated by a Geltech 352280-C aspheric lens, numerical aperture numerical aperture (NA) = 0.15[122], and is focused by a Geltech 352330-C aspheric lens with  $NA = 0.68$ [123]. Both lenses have an anti-reflection coating suitable from 1050 nm to 1620 nm. The diffraction-limited spot size at 1550 nm of this setup is  $1300 \pm 363$  nm[17, 83].

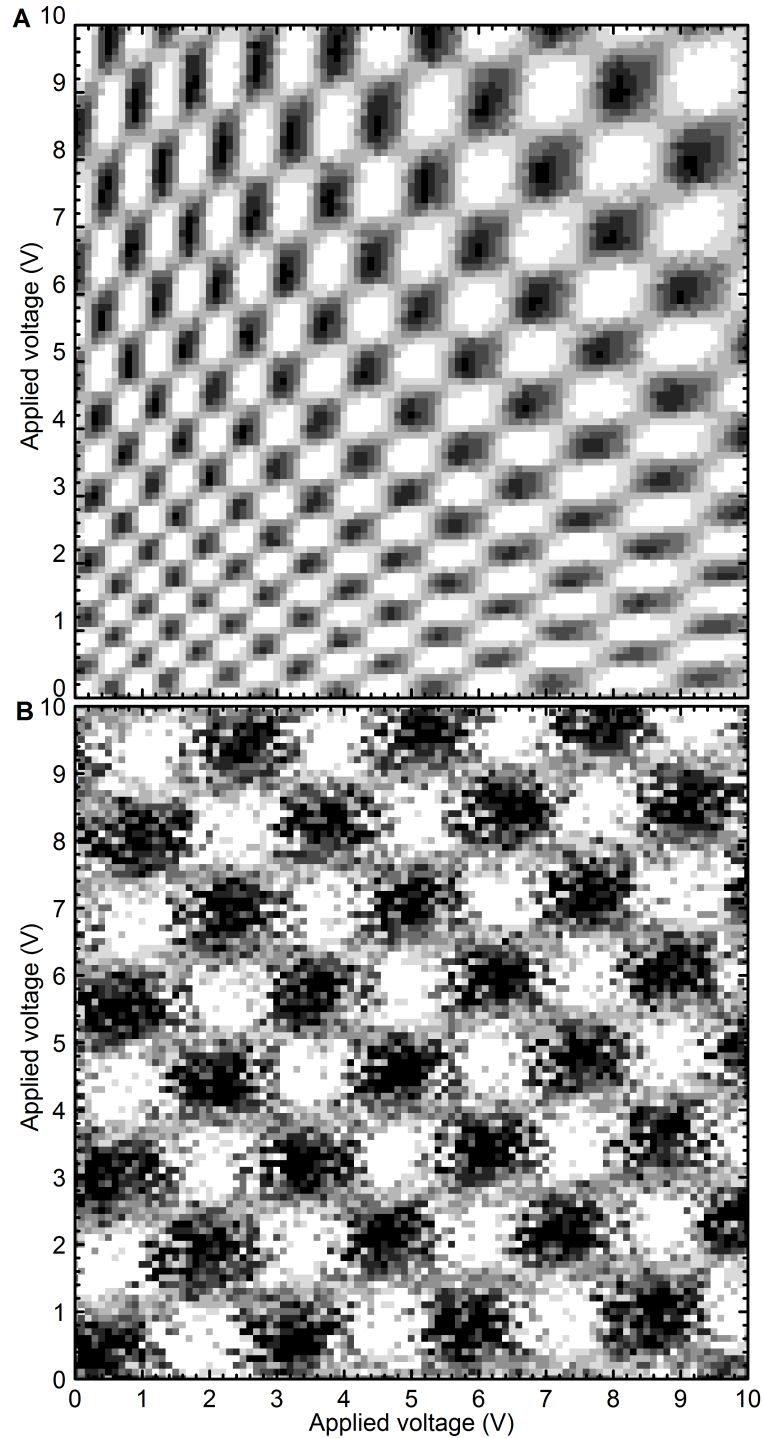


Figure 3.21: Checkerboard pattern imaged by miniature confocal microscope. A checkerboard with a period of  $10\ \mu\text{m}$  ( $5\ \mu\text{m}$  by  $5\ \mu\text{m}$  squares of reflector) is imaged with a broadband superluminescent diode. This allows a conversion from the input measurement (applied voltage, V) to length (position,  $\mu\text{m}$ ). In A, a full-range two-dimensional scan is taken: there is a nonlinear response at large extensions, with the number of full periods of the pattern varying from  $7 \pm 1$  to  $8 \pm 1$ , suggesting a varying scanning range of  $70\ \mu\text{m}$  to  $80\ \mu\text{m}$ . At low temperature, shown in B, the response is much more linear, with  $4.0 \pm 0.5$  repeating units, suggesting a scanning range of  $40 \pm 5\ \mu\text{m}$ .

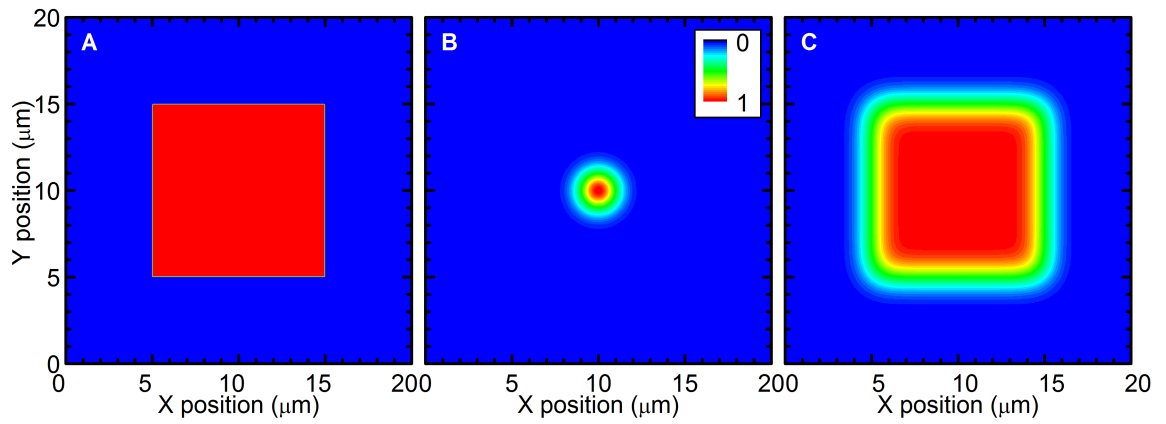


Figure 3.22: Convolution of square and Gaussian. A typical SNSPD is  $10\ \mu\text{m}$  by  $10\ \mu\text{m}$  in size. This is shown in A. If this is illuminated by a  $2\ \mu\text{m}$  FWHM spot (slightly larger than the theoretical minimum of the miniature confocal microscope at  $1550\ \text{nm}$  wavelength) shown in B, then the convolution is what we see as a response. This is shown in C.

### 3.12.1 Spot-response convolution

Using the miniature confocal microscope we raster-scan a Gaussian spot of light and measure the photoresponse with position. A typical SNSPD has a square geometry, but the response from images of the detection efficiency with position are rarely square. In fact, the response seen is a convolution of the underlying geometry and the shape of the spot being raster-scanned. A program was written which allowed convolution of a variable-FWHM spot with an arbitrary bitmap input. The outcome of this is seen in figure 3.22: the SNSPD response area, the red square in A, is convolved with the Gaussian spot in B, producing output C. This looks very similar to the response from a typical SNSPD[71]. A constricted SNSPD, where only one area responds, looks very different: the only response seen will be about the size of the Gaussian beam.

Two-dimensional convolution is performed computationally by multiplying the FFT of the input and the spot, and then calculating the inverse FFT of the real part of the result. Naively, it should be trivial to perform the inverse operation, and deconvolve a result back to its underlying response; however, deconvolution is very sensitive to noise in the signal. Deconvolving a signal that has been convolved by simulation works well, but the noise in the signal of real data (dark counts, oscillations in the base temperature of the fridge) make this practically impossible.

### 3.12.2 Minimising vibration

Though the miniature confocal microscope is housed in a system built around a pulse tube cold head which has low vibration, the system needs to have very low vibration

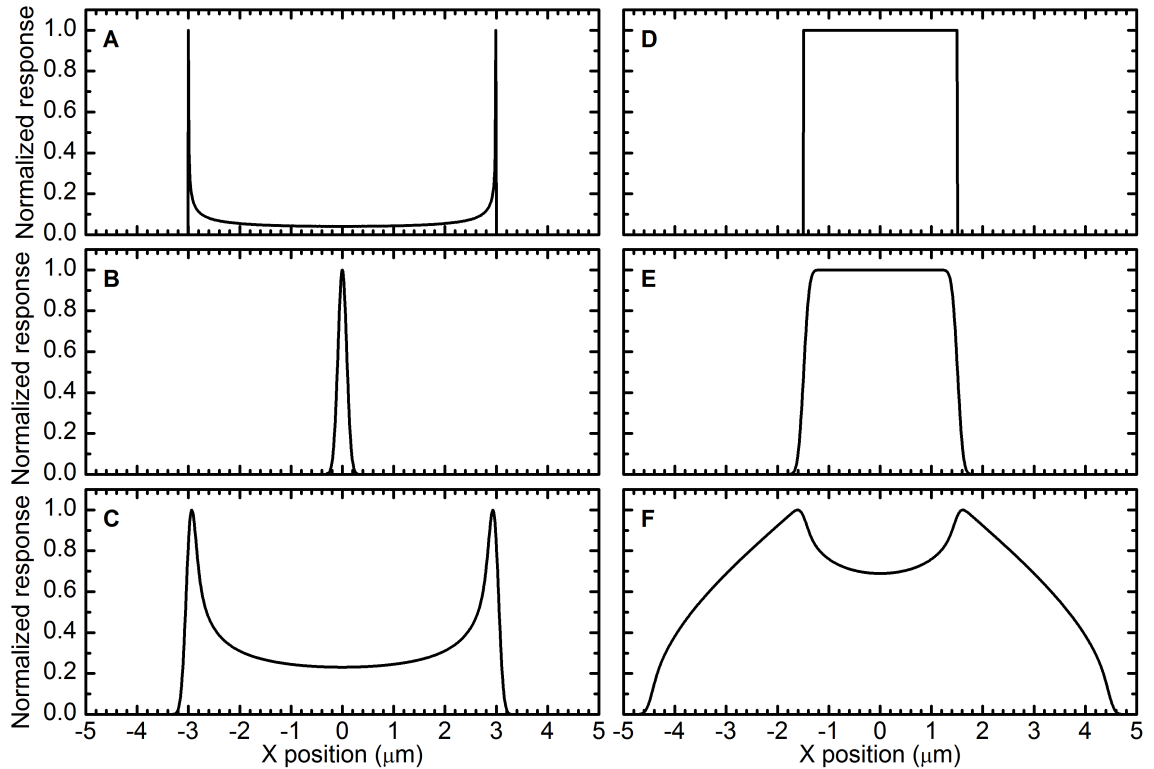


Figure 3.23: Diagram of device response when system vibrating. **A** is a normalized graph of the spatial distribution of simple harmonic motion, with oscillations from  $-3\mu\text{m}$  to  $3\mu\text{m}$ , which would be a typical size for a vibration in the miniature confocal microscope system. **B** is a 2D Gaussian with FWHM of  $2\mu\text{m}$ , representing a slightly out-of-focus spot size. **C** is the convolution of **A** and **B**, and represents the effective beam profile for a Gaussian undergoing simple harmonic motion. **D** represents a cut-through of an  $3\mu\text{m}$  SNSPD, a size used for the individual pixels in the spatially-separate parallel-wire SNSPD experiment, with well-defined edges. **E** shows the expected response when convoluted with the stationary Gaussian in **B**: this is effectively a cut-through of figure 3.22C. **E** is what would be observed if the Gaussian spot is oscillating: the detector response is obfuscated. Subsequently it is clear that very low vibration is a requirement to make meaningful use of the miniature confocal microscope.

levels, as the optical spot being raster-scanned has, when fully focused, a FWHM spot size of  $1.3\mu\text{m}$ . Unless extra precautions are taken, external vibrations couple in, which significantly affect the result. A diagrammatic representation is shown in figure 3.23 and an experimental result when vibrating is shown in figure 3.24. This oscillatory behaviour can obfuscate a genuine result, so it is important to ensure the system is not vibrating.

To mitigate vibrations entering the miniature microscope the cryostat is connected to the cold head by flexible copper braids and the vibrating parts of the cold head are separate from the cold head itself. In addition to this, the cryostat is mounted to a winch system which rests on anti-vibration matting. When in use, the system is lowered onto a further layer of anti-vibration matting and allowed to rest such that neither the winch nor the floor have the full load.

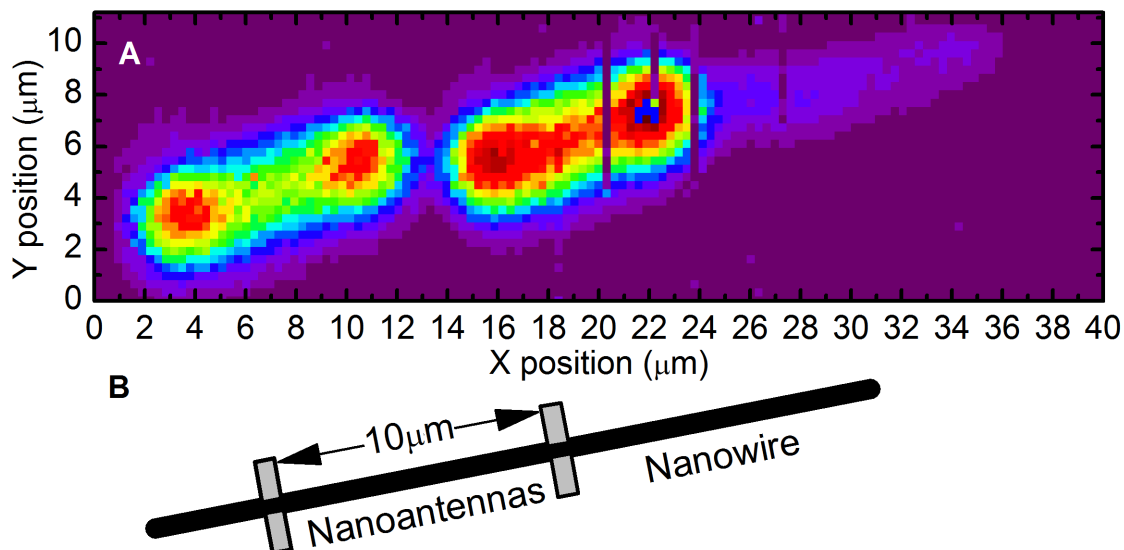


Figure 3.24: Photoresponse of nanoantenna-coupled SNSPD when vibrating. **A** shows the result itself, and **B** depicts the underlying structure: from this we can deduce that there is a strong vibrational oscillation just out-of-line with the direction of the nanowire, causing duplication and smearing of the features.

When resting on the vibration-damping matting, the miniature confocal microscope is focused onto the bond pad of the SNSPD, and the reflection measured. The miniature confocal microscope is then scanned linearly over the edge of the bond pad. When the optics are properly focused, the spot size should be  $1.3\ \mu\text{m}$  FWHM: by looking at the profile of the reflection as the microscope transits across the edge, the spot size can be directly measured. This is carried out in the X and Y directions, as a vibration entirely in X will have no component in Y. If a sub-optimal spot size is measured the cryostat's resting position is shifted and the measurements repeated until the vibrations are gone.

### 3.12.3 Minimizing effect of thermal oscillations

As mentioned in section 3.4, there are oscillations in the temperature of a pulse tube. The efficiency of an SNSPD is a function of temperature: as it oscillates, so too does the count rate. As depicted in figure 3.25**A**, if the measurement time  $t_{meas}$  does not closely match the thermal oscillation time  $t_{osc}$  then measurements taken become dependent on their phase difference with the oscillation time. In order to cancel out this effect, it is important to match  $t_{meas}$  and  $t_{osc}$ . By taking the measurements in figure 3.25**B** it was determined that  $t_{osc} = 0.7\ \text{s}$ . Thus, measurements presented in this work are taken over  $0.7\ \text{s}$  and normalised to cps, or stated as the SDE in %.

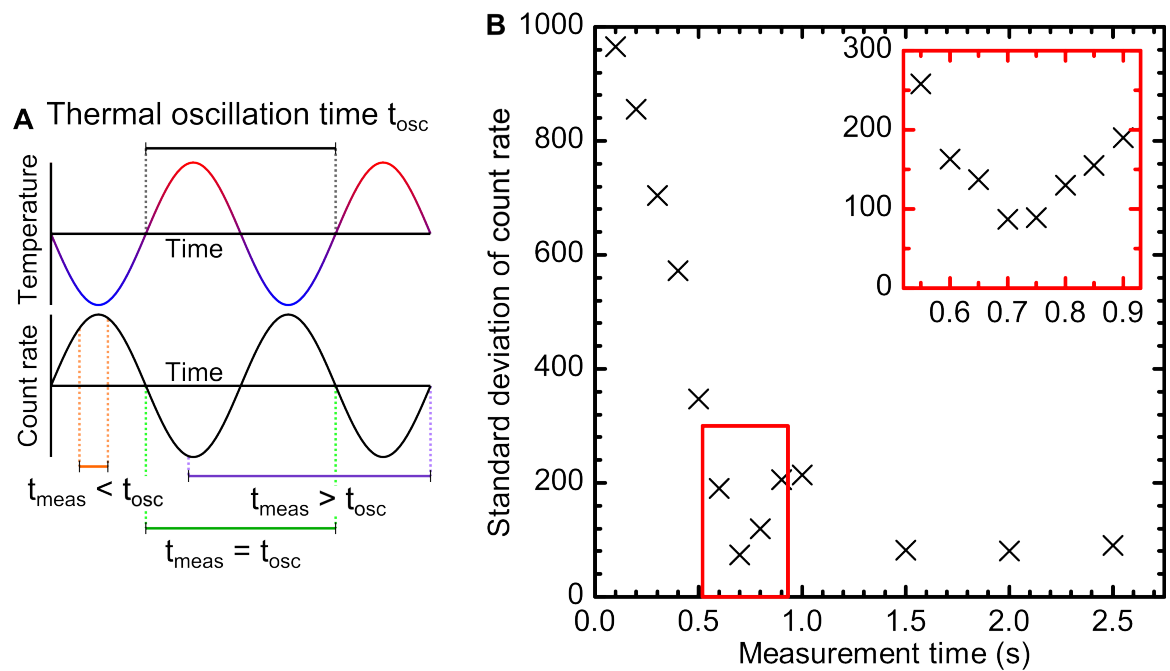


Figure 3.25: Effect of thermal oscillations on SNSPD count rate. A common and natural unit to measure a count rate in is counts per second (cps) or Hz. However, as seen in A, the efficiency of a detector is related to its temperature by its critical current  $I_C$  which has a temperature dependence. If the thermal oscillation time  $t_{osc}$  is not equal to  $t_{meas}$  this will result in readings that overcount and undercount, adding oscillations into any measurements that are taken. Readings for longer than the thermal oscillation time suffer the same issue but to a smaller extent. As shown in B, for the equipment used for the work in this thesis, when  $t_{meas} = 0.7s$  the standard deviation of the measurements is minimized, suggesting discrepancy due to thermal fluctuations are minimised.

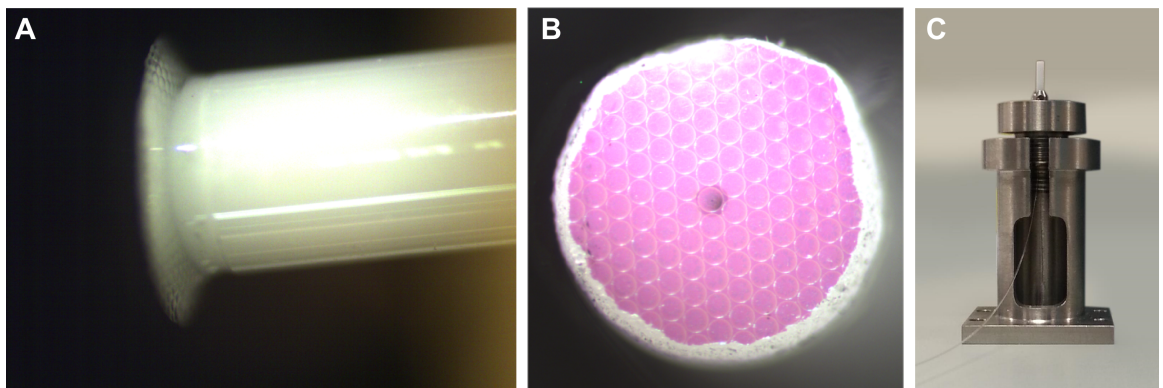


Figure 3.26: Photograph of DBR fibre and fibre mount. A shows a zirconia fibre ferrule viewed from the side with a microscope: attached to the end is a DBR array. This is seen more clearly from the front in B. A large number of the  $r = 250\mu m$  spherical caps are adhered to the ferrule, but the fibre cladding (dark area in the centre) is centred on the outline of a DBR cap. In the centre of this is the single-mode fibre (SMF)-28 fibre core, seen as a black dot. The edges have been filed down to allow the ferrule to pass through the fibre mount. The mount itself with a mounted fibre is shown in C. This is attached by screws to the low-temperature piezoelectric motors used by the miniature confocal microscope described in section 3.12 and allows mounting of fibres.

### 3.13 Tunable cavity configuration

In order to build a tunable cavity, a cavity is required, as is some method of tuning. To this end a fibre mount was constructed for use with the miniature confocal microscope system detailed in section 3.12. Into this we placed either a fibre with attached DBR, or a bare fibre for comparison. Using a grub screw to secure the fibre ferrule, this allows movement of the fibre over the surface of the SNSPD, and tuning of the cavity length. When coupled with the tunable-wavelength laser sources described in section 3.14 this allows two-dimensional tuning of the cavity.

#### 3.13.1 Distributed Bragg reflector design

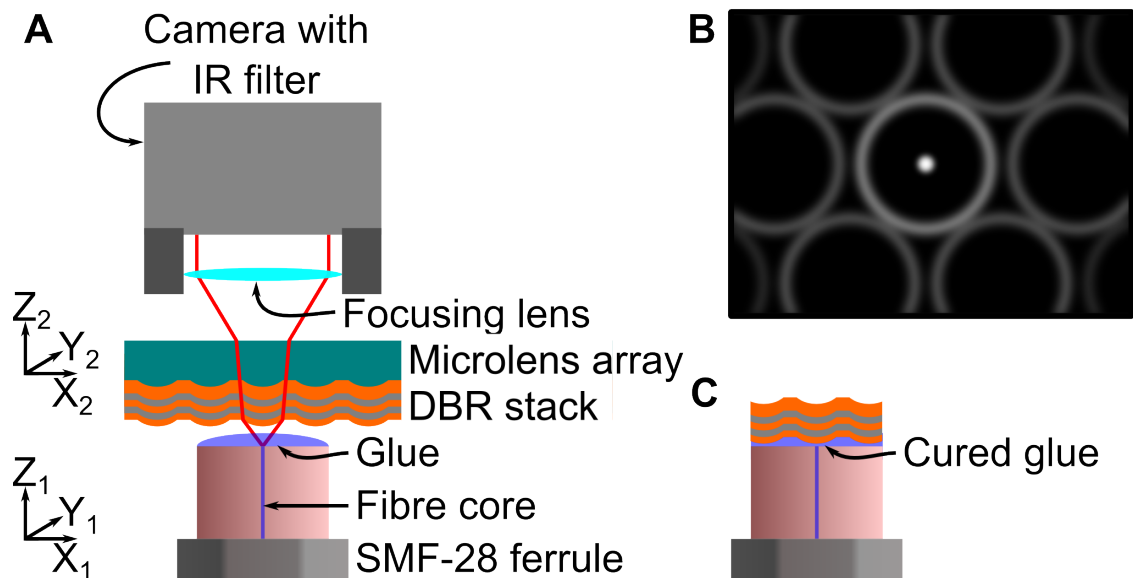


Figure 3.27: Schematic of attaching the DBR layers to the fibre ferrule. The alignment rig is shown in A: a fibre ferrule with  $X_1, Y_1, Z_1$  movement axes is situated beneath the microlens array, with  $X_2, Y_2, Z_2$  movement axes. These are both able to move independently, allowing alignment beneath a computer-controlled video camera with infra-red (IR) filter. This produced an image similar to the diagram in B: by adjusting the two sets of axes, it was possible to align the fibre core with the centre of a microlens. The ferrule was brought into contact with the DBR stack after application of an adhesive glue to the polished end and left to cure. After curing the ferrule was moved away from the microlens array, pulling the DBR layers with it. This is shown in C; photographs are shown in figure 3.26.

A key technical challenge for building the optical cavity was the creation of a DBR-coated fibre ferrule. Dr Michael Tanner designed glass microlens arrays, with hexagonal close-packed spherical caps with radius of curvatures of  $250\ \mu\text{m}$  to  $500\ \mu\text{m}$ . A Dektak profilometer measurement of the surface of an  $r = 250\ \mu\text{m}$  lens is shown in figure 3.28. At Optische Interferenz Bauelemente GmbH, Germany, two pairs of  $\text{TiO}_2/\text{SiO}_2$  layers, with a thickness per layer of  $L_t = \lambda_0/4n$  were deposited, where  $\lambda_0$  is the desired

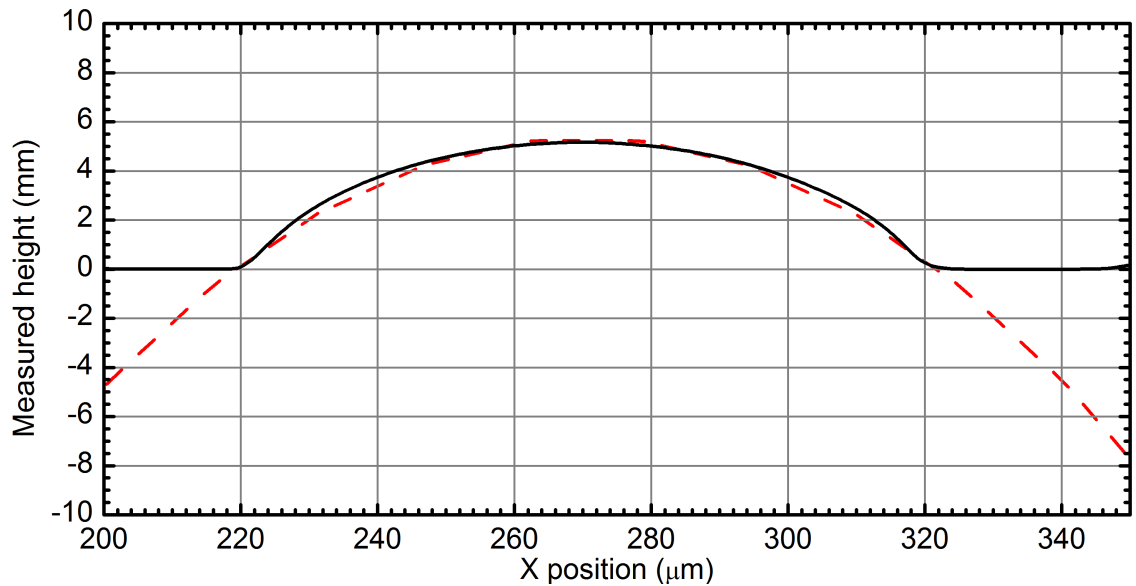


Figure 3.28: Dektak profile of microlens substrate. The black line is data sampling a  $250\ \mu\text{m}$  microlens, with one point every  $0.5\ \mu\text{m}$ . This is fitted with an  $r = 250\ \mu\text{m}$  circle, shown as a red dashed line. The spherical cap is in good agreement with the circle.

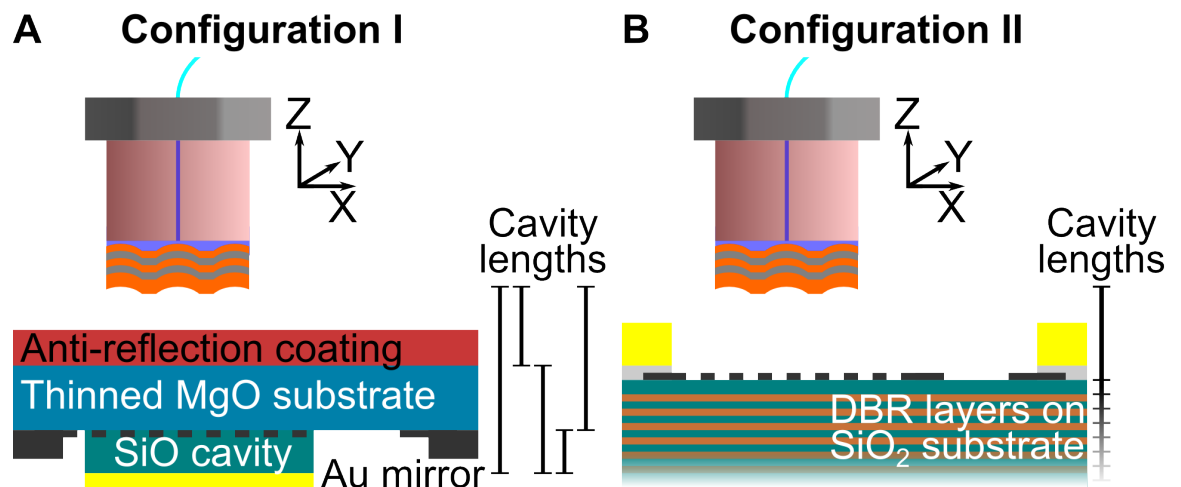


Figure 3.29: Diagram of the two optical cavities formed with Configurations I and II. In both, light arrives through the fibre ferrule which is mounted on low-temperature piezoelectric motors, passing through the DBR layers on the tip. This creates a tunable optical cavity with the reflector deposited behind the SNSPD. In **A**, which depicts Configuration I, the light is back-side coupled to the SNSPD through  $250\ \text{nm}$  of anti-reflection fluoropolymer, and a  $45\ \mu\text{m}$  thinned MgO substrate. The reflector,  $100\ \text{nm}$  of gold, is mounted on  $250\ \text{nm}$  of SiO spacer. The possible cavity lengths from reflective interfaces are shown by the lengths demarcated to the right of the diagram: the full length, from the fibre to the mirror, is expected to be strongest, due to the high reflection from the Ag. In **B**, which depicts Configuration II, the light is front-side coupled to the SNSPD, and reflects off the DBR layers directly behind the SNSPD. This has a single cavity with an indeterminate length.

resonance wavelength in free space. These had a final layer of thickness  $L_t = \lambda_0/2n$  of  $\text{TiO}_2$  deposited to set the phase of the reflected signal such that there was a node at the DBR-vacuum interface.

An alignment system with three degrees of freedom for the microlens array and three degrees of freedom for the ferrule in-line with an infra-red camera was used to position the centre of the ferrule at the centre of a microlens, shown in figure 3.27A. A schematic depicting the image from the camera used to align the two layers is shown in figure 3.27B. The spot of light, shown centre, is aligned with the centre of the outline of the distortion caused by the presence of the microlens. The input laser power was decreased until it was barely visible to allow the best alignment, and the ferrule was slowly brought nearer to the microlens array until it touched. The ferrule was then backed away and adhesive was applied to the polished zirconia face of the ferrule, then the face was brought back into contact with the DBR-layered microlens array and left to cure. Once cured, the ferrule was moved away from the microlens array, the adhesive pulling the DBR coating with it, as shown in figure 3.27C. In figure 3.26A, a photograph of the ferrule viewed from the side is shown. From figure 3.26B, a photo from above the ferrule end, we can see that the alignment was imperfect. Owing to the microlens array being comprised of shallow spherical caps this misalignment was not expected to significantly alter the behaviour of the cavity. The ferrule, mounted in the housing that is attached to the piezoelectric motors, is shown in figure 3.26C.

The adhesive used, Epoxy Technology EPO-TEK 301-2, was chosen as it is low-outgassing, which is important in a high-vacuum environment, and it has 98% transmission in the wavelength range used[124]. Furthermore, its refractive index was expected to be closely matched with the SMF-28 optical fibre used[125] which minimized back-reflections and losses in the system. Though not explicitly designed for cryogenic operation, in private correspondence to Dr Michael Tanner it was recommended for use at low temperature by an Epoxy Technology Applications Engineer.

The ferrule was employed to form a cavity with a gold reflector, referred to as Configuration I, which is shown in figure 3.29A. Configuration II is shown in figure 3.29B and depicts the same ferrule forming a cavity with a DBR reflector. This has a more tightly-focused wavelength response, determined by the separation of the layers in the DBR substrate and DBR fibre.

### 3.13.2 Cavity lengths from fringe spacing

It is possible to calculate the length of a tunable cavity by measuring the distance between interference fringes. Let the length of a cavity be defined as  $d$ . Resonance will occur when there are an integer number  $N$  of waves with wavelength  $\lambda$  standing along

the full path length of this cavity, the length  $2d$ . This is the familiar equation

$$2d = N\lambda \quad (3.9)$$

which may be found in any introductory text[40]. If we have two adjacent resonance wavelengths such that  $\lambda_1 < \lambda_2$ , by equation 3.9 we can describe these by  $\lambda_1 = 2d/N$  and  $\lambda_2 = 2d/(N - 1)$ . The difference between these resonance wavelengths is then  $\Delta\lambda = \lambda_2 - \lambda_1$ . Substituting, we obtain  $\Delta\lambda = 2d/(N - 1)N$ . If  $N$  is large, such that  $N \approx N - 1$ , then this becomes

$$\Delta\lambda \approx \frac{\lambda_1^2}{2d}. \quad (3.10)$$

This equation allows measurement of cavity lengths by tuning the wavelength of the laser sources. However, the calculation does not consider the effect of the refractive index the cavity is in  $n$ , which has the effect of changing the propagation velocity of the wave. Subsequently, a cavity length calculated using equation 3.10 must be scaled accordingly. There is one further factor to consider: the cavity may be through a substrate, with refractive index  $n_{sub}$ , and we are tuning a vacuum gap,  $n_0$ , so the effective  $n$  will actually be a weighted average of these indices and lengths. By letting total length  $d = d_{sub} + d_{gap}$ , average  $n = (d_{sub}n_{sub} + d_{gap}n_0)/d$ . We can redefine  $\lambda$  to be the effective wavelength  $\lambda = \lambda_0/n$  where  $\lambda_0$  is the wavelength when  $n = 1$ , substitute in, simplify as  $n_0 = 1$ , and rearrange for  $d_{gap}$ , and so the final equation

$$d_{gap} \approx \frac{\lambda_1^2}{2\Delta\lambda} - d_{sub}n_{sub} \quad (3.11)$$

is derived. This equation relies on *a posteriori* knowledge of the distance through the substrate to the reflector  $d_{sub}$  and its associated  $n_{sub}$  to obtain a valid cavity  $d_{gap}$  length, but this isn't a significant limitation, and the result can be verified: we employ OCT to demonstrate and confirm the validity of this approach for determining  $d_{gap}$  values in figure 3.31.

Cavity behaviour for the device shown in figure 3.29A is shown in figure 3.30. The optical cavity length may be measured using equation 3.11, which with  $\Delta\lambda = 10.5$  nm,  $\lambda_1 = 1529$  nm,  $d_{sub} = 45$   $\mu$ m and  $n_{sub} = 1.71$ [126] gives  $d_{gap} = 34.4$   $\mu$ m. The simulation parameters are for an 33.9  $\mu$ m gap; given that the equation used to calculate this is an approximation, there is good agreement here.

To further confirm the validity of equation 3.11, comparison with OCT was performed. This is shown in figures 3.31A and B. At both cavity lengths there is good agreement between the measurements.

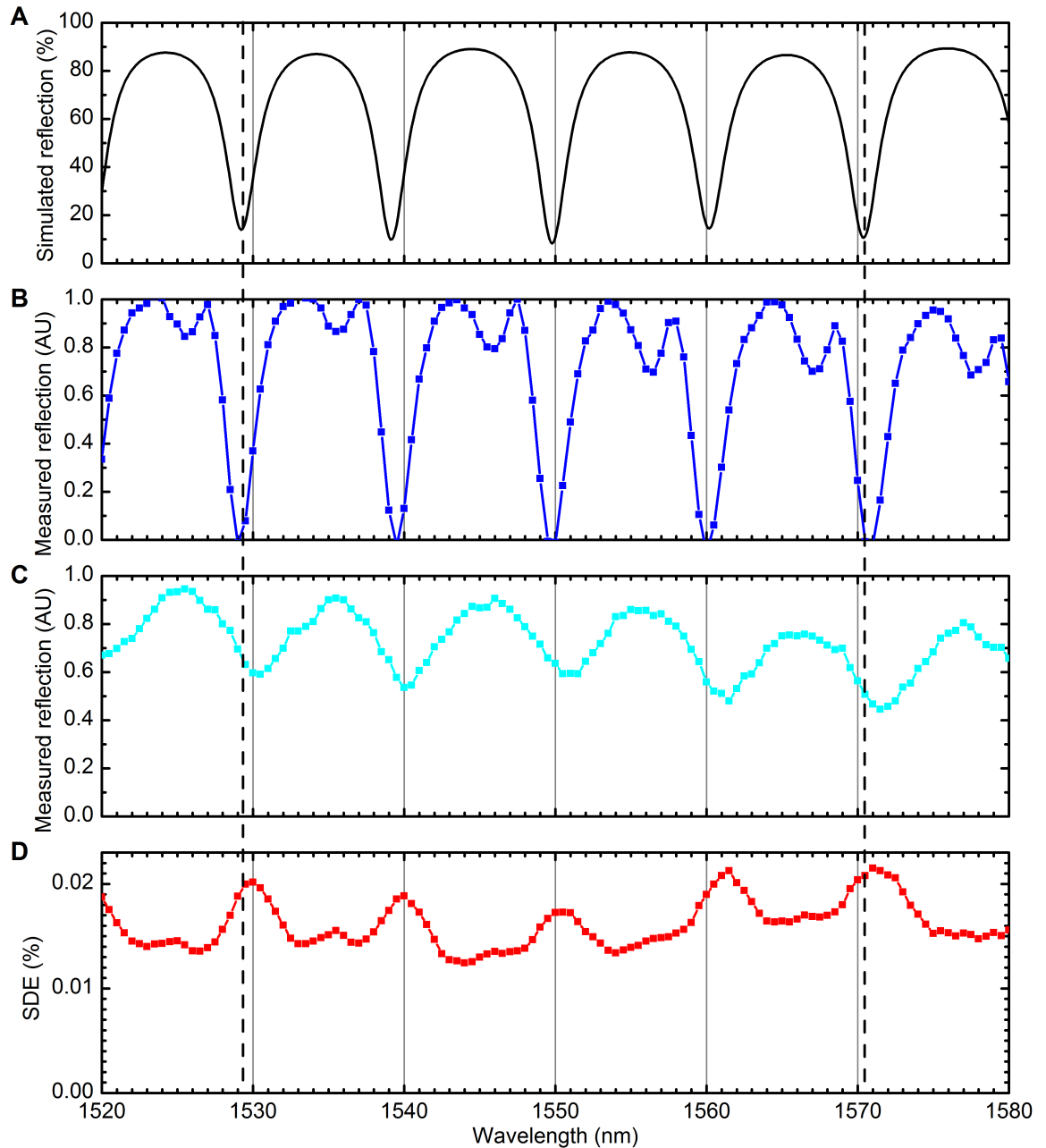


Figure 3.30: Comparison of simulated and experimentally-observed cavity behaviour. A preliminary method for verifying the optical cavity behaviour is to test the reflection back through the system: when the cavity is resonant the reflection should be negligible. The simulated reflected signal from the bond pads is shown in A as a continuous black line (parameters:  $33.9\ \mu\text{m}$  air gap,  $45\ \mu\text{m}$  MgO). Directly-comparable reflection determined experimentally is shown in B, in blue. The measured reflection when illuminating the detector area is shown in C, in cyan. Finally, the SDE of the detector is measured, shown in D. As the cavity moves in and out of resonance, the reflected signal drops, and the SDE peaks. Though there are some oscillations on the signal experimentally, the resonances are in close agreement. For comparison with theory, a length of four oscillations is demarcated by dashed black lines. This suggests a fringe spacing  $\Delta\lambda$  of  $10.5\ \text{nm}$ .

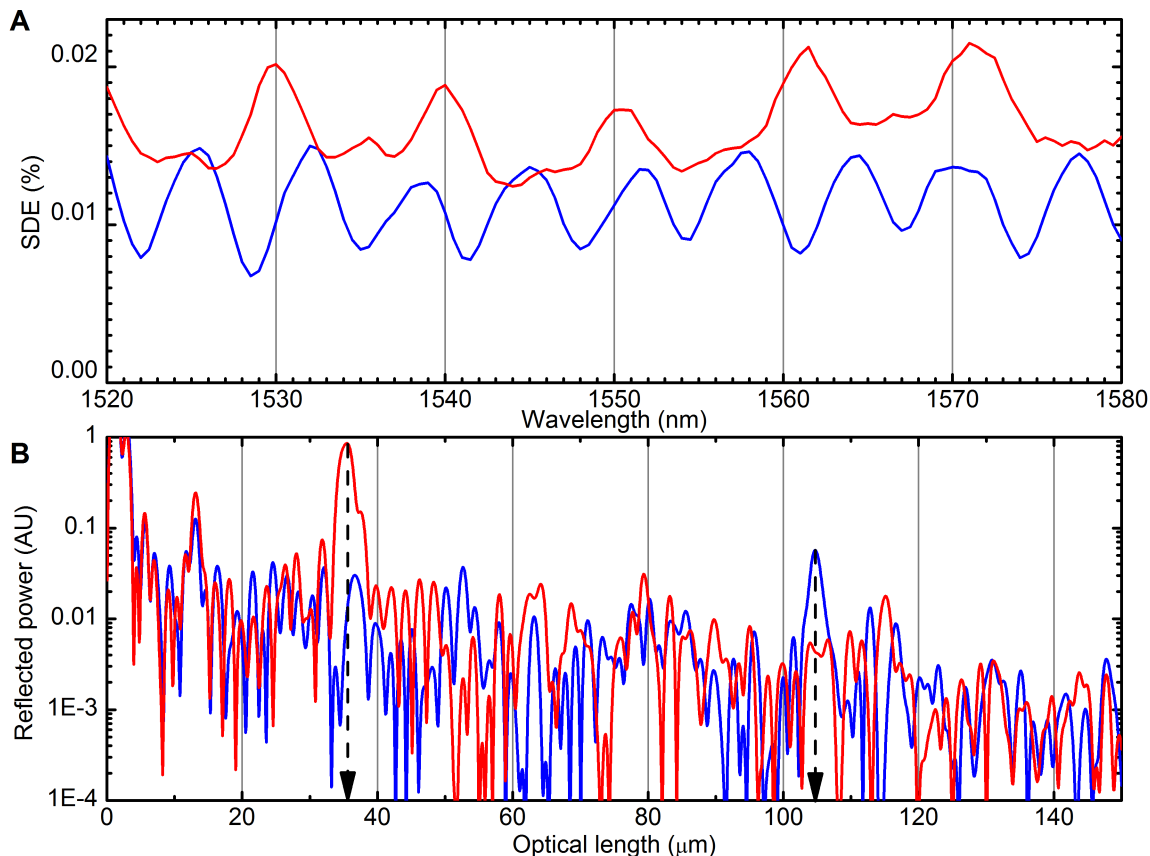


Figure 3.31: Graphs depicting the agreement between OCT and fringe spacing calculation. Wavelength–SDE scans (A) and OCT (B) were carried out at two cavity spacings. The initial air gap length is calculated from the same data shown in figure 3.30D, and suggests as previously calculated a gap length of 34  $\mu\text{m}$ . It is shown as red lines in both graphs. Via OCT, we see a response at an optical length of 35  $\mu\text{m}$ , in agreement with the previous simulation and calculation. This signal is reflection from the near side of the detector package rather than the back of the cavity. Looking at the data after increasing the cavity length, shown as blue lines, we see a more frequent oscillation in the SDE, suggesting  $\Delta\lambda = 6.5 \text{ nm}$ . This in turn suggests  $d_{gap} = 101 \mu\text{m}$ : we see a peak in the OCT at around 105  $\mu\text{m}$ .

### 3.14 Wavelength scanning tests

To take measurements of detectors that have a response dependent on wavelength, such as detectors that have resonant features such as nanoantennas or that are fabricated in a cavity, a tunable wavelength source is beneficial. Additionally, as nanowires have a power absorption related to the polarisation of the incident light[68, 127] it is important to consider the variation in polarisation when tuning a tunable laser. To this end a system of three CW external cavity tunable lasers connected to an electronic polarisation controller was designed and constructed, and a control program written that stepped through a range of wavelengths, measuring a set of polarisations at each step.

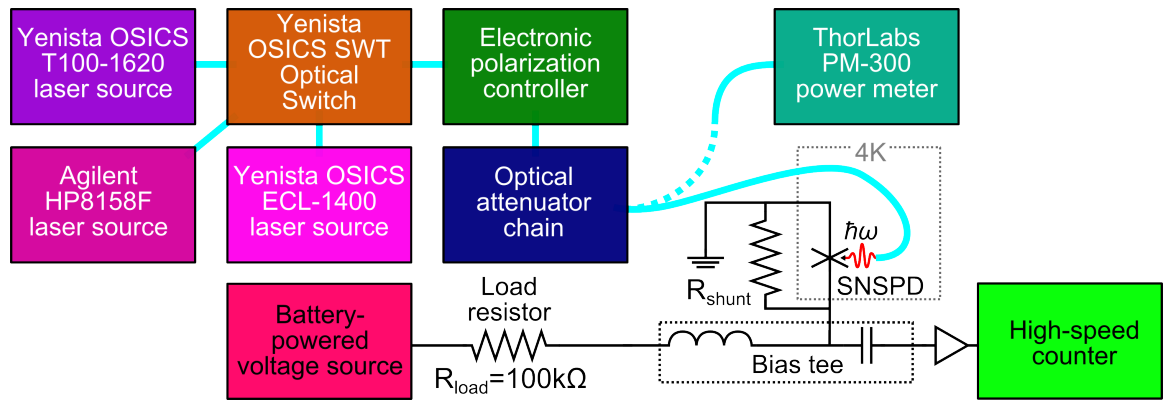


Figure 3.32: Diagram of wavelength scanning test setup. Three laser sources, shown as shades of purple, are connected by SMF-28 to the optical switch. This runs through a polarisation controller and into the attenuator chain described earlier. From this the system may be attached to a ThorLabs PM-300 power meter (dashed line) or connected to the SNSPD system.

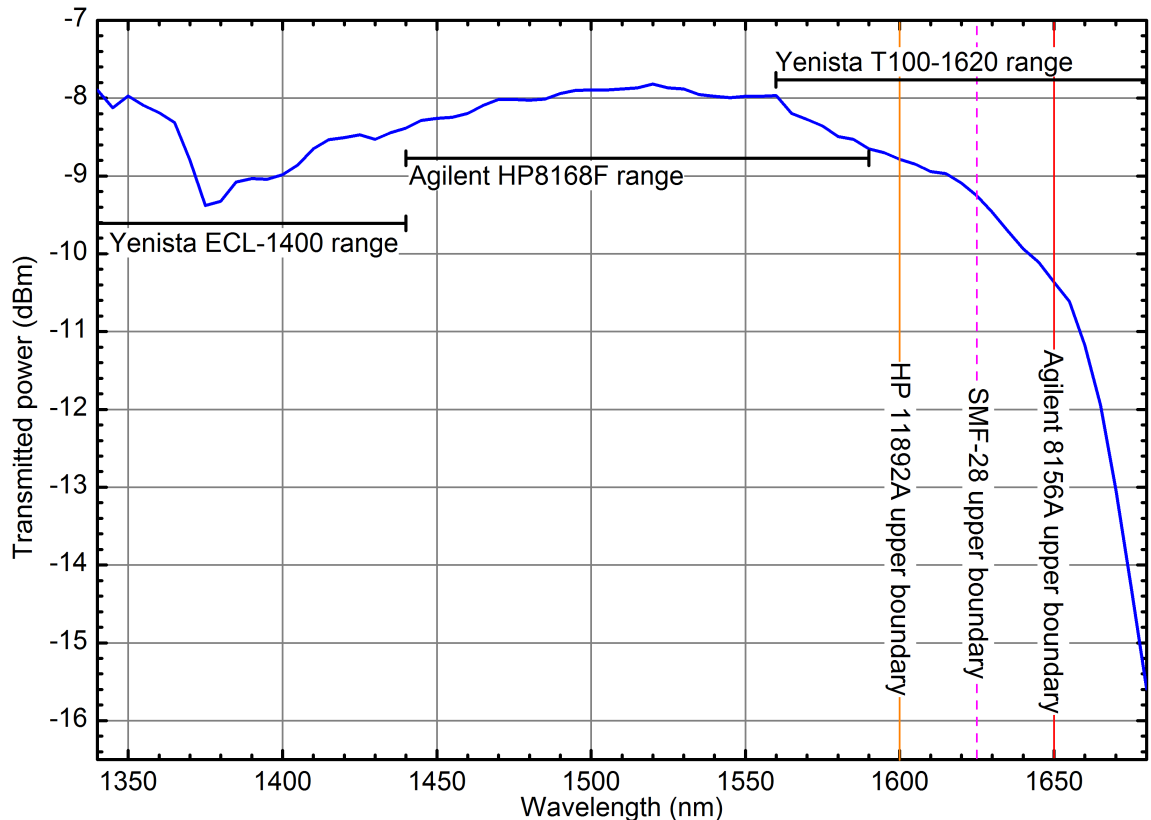


Figure 3.33: Graph of typical power profile of wavelength scanning system. The power is measured after all optical components but before entry to the closed-cycle cryostat. The wavelength ranges of the three constituent lasers are shown as labelled bands. Boundaries of the wavelength ranges of optical components that fall within the laser ranges are shown as coloured lines. The losses from the polarisation controller and SMF-28 outside so close to their range are small, and are able to be taken into account. However, at 1650 nm the attenuators, which in this power measurement are set to 0 dB of applied attenuation, can go no higher and remain accurate. As such, wavelengths above 1650 nm are tested using this system.

An Agilent HP 8168F (range 1440 nm to 1590 nm)[128], a Yenista OSICS ECL-1400 (range 1340 nm to 1440 nm)[129] and a Yenista OSICS T100-1620 (range 1560 nm to 1680 nm)[130] were all connected to an electronically-controlled optical switch, a Yenista OSICS SWT. The switch output was then passed through two Agilent 8156A variable optical attenuators (range 1340 nm to 1650 nm) connected in series, and this was then passed through an Agilent 11896A electronic polarisation controller. By taking a power calibration using a Thorlabs PM 300 power meter it was possible to post-correct for the nonlinear power profile of this system. This is shown schematically in figure 3.32 and a typical power measurement is shown in figure 3.33.

The fibre used, SMF-28[131], has less than 0.35 dB losses per kilometre of length in the wavelength range 1310 nm to 1625 nm; this variation, alongside the variation in the output laser power with wavelength, is mitigated by post-correction, leaving only the small length of fibre within the cryostat and scope optics unaccounted for. A method for measuring the spot size was detailed in section 3.12.2. By using this method at the extremes of the wavelength range (1340 nm and 1650 nm), we were able to confirm that the spot size variation remains within the stated error of the measurement at a wavelength of 1550 nm, discussed in section 3.12.

## 3.15 Programming and automation

Where required, automation of the experimental procedures was performed to increase their reliability and repeatability. This was generally performed in the interpreted programming language Python, using version 2.7. To allow rapid development, a variety of third-party modules were used. These modules are listed below.

**PyVISA** for interaction with hardware connected via general purpose interface bus (GPIB) or serial

**NumPy** for mathematical operations, calculation of FFTs, and handling of matrices

**SciPy** for fitting algorithms and basic signal processing

**Matplotlib** for rapid plotting of experimental data

**Python Image Library** for input and output of signal convolution

**wxPython** for creating a graphical user interface for written software

**Django** for web-based monitoring of system performance

Further to automating experiments, custom user-driven software was written. An example of the spot-device response convolution software is shown in figure 3.34. This

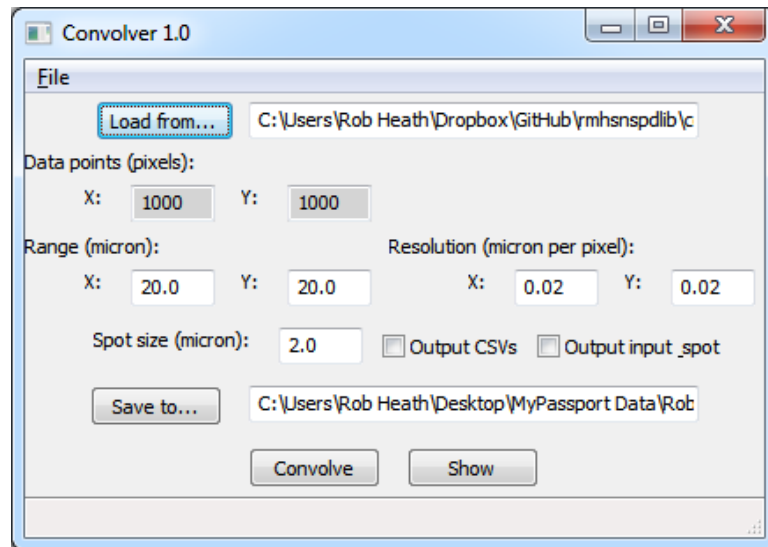


Figure 3.34: Example of custom convolution software written for analysing output.

software was used to compare the photoresponse of a detector with what would be expected from its underlying geometry: an example of its output is shown in figure 3.12.1. In addition to this, routines were written for analysing data and fitting theory, as well as web-based software for remote monitoring of the health of unattended systems operating at low temperature.

# Chapter 4

## Spatially-resolvable parallel-wire SNSPDs

Superconducting nanowire single photon detectors (SNSPDs)[45] are exceptionally fast single photon detectors with low jitter[132]. This makes them desirable for applications in satellite communications[133], medical physics[13], fiber-optic distributed Raman temperature measurement[134], and quantum communications and computing[8, 14]. For observing photon anti-bunching in quantum optics and in many areas of quantum information[135] photon number resolution (PNR) is desirable[136]: a single-wire SNSPD does not have this property.

The device physics of parallel-wire SNSPDs is based on a cascade process, as described in section 3.7. Using nano-optical techniques and a parallel wire device with spatially-separate pixels this work explicitly demonstrates the single- and multi-photon triggering regimes. It develops a model for fitting the efficiency of a detector operating in the arm-trigger regime. This work investigates the timing response of the detector when illuminating a single pixel and two pixels, and observes a change in the active area of the detector between the two regimes. It finds the two-pixel trigger regime to have a faster timing response than the one-pixel regime. This work suggests that a multi-pixel detector connected in parallel could be used to discriminate between less-than  $N$  and  $N$  or more photon detection, allowing photon number discrimination and so allowing a single SNSPD to be used in some cases where PNR is required.

### 4.1 Multi-pixel triggering theory

The fitting equation detailed in equation 3.5[21] describes the probability of a nanowire with quantum efficiency  $\eta$  detecting at least one of  $\mu$  incident photons when illuminated by a pulsed laser with repetition rate  $f$ . This works only in the case where there is

one detector element. We have  $R_{detected}$  as the detected count rate,  $f$  as the repetition rate of the pulsed laser source,  $\mu$  as the mean photon number per pulse,  $\eta$  the quantum efficiency, and  $D$  as the dark count rate.

In a typical multi-element SNSPD[73, 74, 117, 137] there are  $n_{par}$  wires connected electrically in parallel. Equation 3.5 can be used to describe photon absorption when  $n_{par} > 1$ , but only when  $b = 1$ , where  $b$  is the required number of pixels to absorb a photon before the detector outputs a pulse (derived from new model in section 4.1.2). This is called the ‘arm-trigger’ regime of a parallel-wire SNSPD[74]. Calculating  $\eta$  when  $b > 1$  for a given detector is not possible using equation 3.5.

One might intuitively imagine that simple statistical models could be applied to a detector in this scenario. However, the binomial distribution, which has been used to describe a single-element SNSPD detecting multiple photons[138] is unable to be applied here as the absorption of each of the  $\mu$  incident photons is not independent: once a pixel is ‘armed’, its current is redistributed through the remaining  $n_{par} - 1$  pixels and it becomes dead until the detector resets or  $b - 1$  other pixels are also ‘armed’, at which point the whole detector triggers.

One might also look at applying a hypergeometric distribution to the problem, but here also the model doesn’t fit the scenario: a hypergeometric distribution requires a finite number of possible failures. An SNSPD’s detection efficiency being less than unity means that it’s possible (though improbable) that all  $\mu$  photons will fail to be absorbed, even in a single pixel case. For an accurate description of parallel-wire detection this important factor must be included.

When approaching multi-pixel triggering theory, an initial attempt to describe the photoresponse was designed using Markov chains. This provided a good approximation of the response, but ignored dark counts. A more accomplished Bayesian model was developed in collaboration with Mark Webster at the University of Leeds which includes the dark-count rate[18]. Both models are presented here.

### 4.1.1 Markovian approximation

Equation 4.1 defines the system detection efficiency (SDE) with three factors, the coupling coefficient  $\eta_{coupling}$  representing the probability of the photon coupling into the nanowire, the absorption coefficient  $\eta_{absorption}$  representing the probability of the coupled photon being successfully absorbed in the thin film, and triggering coefficient  $\eta_{trigger}$  representing the probability of the device then going on to trigger.

$$\eta = \eta_{coupling} \cdot \eta_{absorption} \cdot \eta_{trigger} \quad (4.1)$$

In a parallel-wire device with  $n_{par} \geq b \geq 2$ ,  $\eta_{coupling}$  changes between one absorbed photon and the next, as the active area is reduced. Subsequently, we use  $\eta$  in this definition as shorthand for  $\eta_{absorption} \cdot \eta_{trigger}$ , and consider  $\eta_{coupling}$  as a separate pre-factor, as this is dependent on the positioning of the detector. To simplify this, we assume that each pixel is equally illuminated, which holds true for devices illuminated symmetrically, and is also a valid approximation for devices illuminated by a Gaussian spot with a full-width half-maximum significantly larger than the detectors' active area.

Defining a bi-diagonal square matrix  $\mathbb{P}_m$  of side  $b+1$  elements, as in equation 4.2 with rows  $0 \leq i \leq b$  and columns  $0 \leq j \leq b$ , and where  $p_{i,j}$  represents the probability of going from row  $i$  to state  $j$ , we have a Markovian transition matrix model for each incident photon.

$$\mathbb{P}_m = \begin{pmatrix} (1-\eta) & \eta & 0 & 0 & \dots & 0 & 0 \\ 0 & (1 - \frac{n_{par}-1}{n_{par}}\eta) & \frac{n_{par}-1}{n_{par}}\eta & 0 & \dots & 0 & 0 \\ 0 & 0 & (1 - \frac{n_{par}-2}{n_{par}}\eta) & \frac{n_{par}-2}{n_{par}}\eta & \dots & 0 & 0 \\ \vdots & \vdots & \vdots & \vdots & \ddots & \vdots & \vdots \\ 0 & 0 & 0 & 0 & \dots & (1 - \frac{n_{par}-b}{n_{par}}\eta) & \frac{n_{par}-b}{n_{par}}\eta \\ 0 & 0 & 0 & 0 & \dots & 0 & 1 \end{pmatrix} \quad (4.2)$$

In this, there is  $1 - \eta$  chance of not triggering the a pixel and  $\eta$  chance of going from zero triggered pixels to one pixel,  $1 - \frac{n_{par}-1}{n_{par}}\eta$  chance of staying at one triggered pixel and  $\frac{n_{par}-1}{n_{par}}\eta$  chance of triggering the second, and so on. The final state  $p_{b,b} = 1$ , as once this threshold level is reached the detector triggers and any further detections become irrelevant.

By raising the transition matrix to  $\mu$ , we obtain a transition matrix that describes the probability of absorbing at least  $b$  photons on unarmed pixels. Defining the row vector  $\mathbb{S}$  in equation 4.3, which is  $b+1$  elements long with  $0 \leq j \leq b$  and  $s_j$  representing the probability of  $j$  pixels being triggered, we can obtain the probability of the detector triggering by calculating equation 4.4.

$$\mathbb{S} = \left( 1 \ 0 \ 0 \ 0 \ 0 \ \dots \ 0 \right) \quad (4.3)$$

$$\mathbb{Q} = \mathbb{S}\mathbb{P}_m^\mu \quad (4.4)$$

Similar to  $\mathbb{S}$ ,  $\mathbb{Q}$  is a row vector where  $q_j$  represents the probability of  $j$  pixels being triggered. The value of  $q_b$  represents the probability of at least  $b$  photons being absorbed, and thus represents the probability of a parallel-wire SNSPD emitting an output pulse when illuminated by  $\mu$  photons.

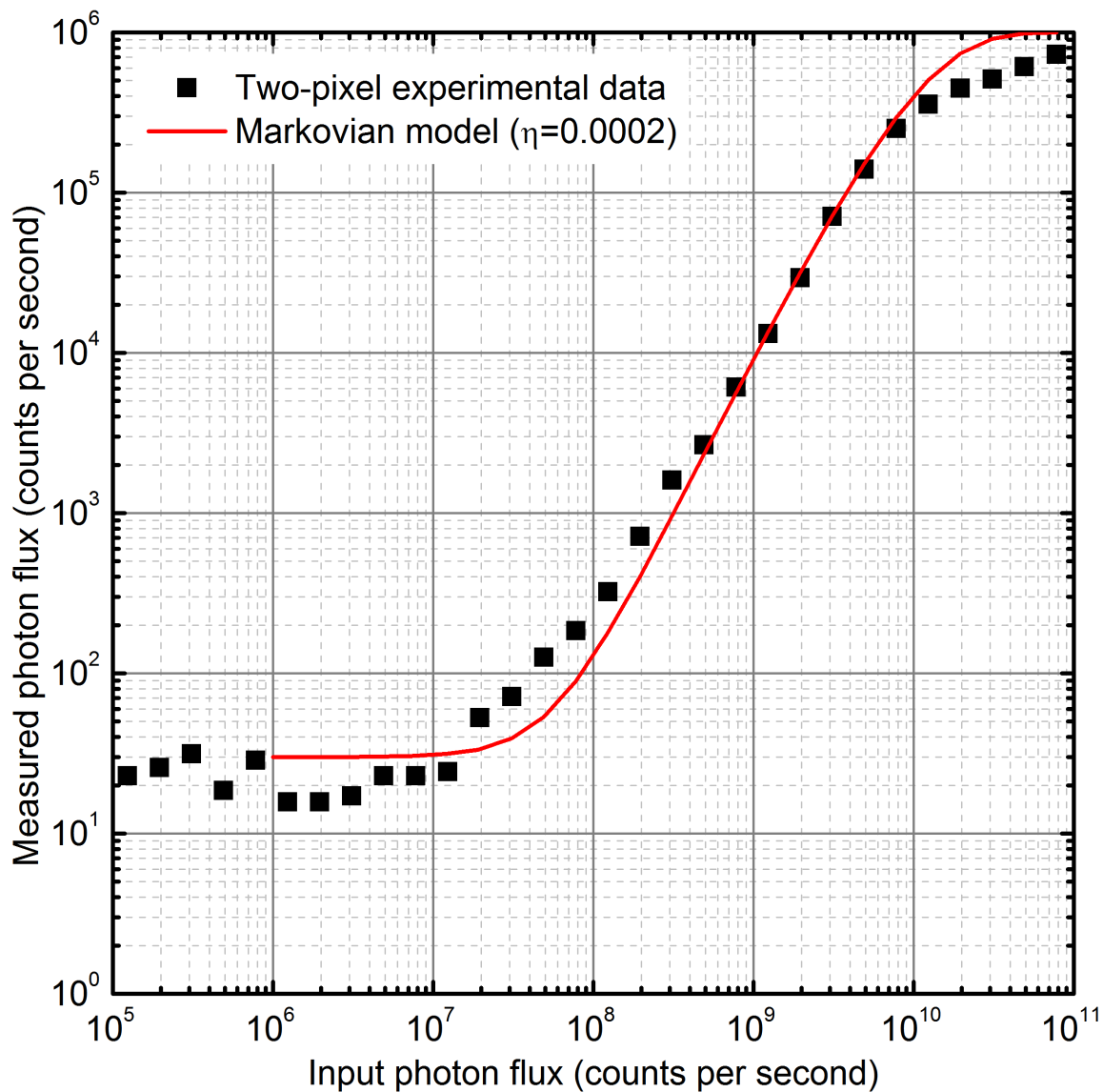


Figure 4.1: Comparison of Markovian two-pixel triggering model with real data. Owing to the complex nature of the model, this is not a rigorous  $R^2$  fit but a ‘by eye’ comparison. The model is slightly modified by the simple addition of a dark count rate of 30 counts per second (cps). The model loosely fits the data.

This model offers a simple, easily-scalable approximation of the response of a detector with multiple parallel pixels, as seen in figure 4.1. However, this model is unable to properly handle dark counts, which are simply added. Additionally, raising matrices to high powers is computationally intensive, and is too complex for fitting in many software packages. In light of this, a new model was designed.

### 4.1.2 Bayesian model

In this Bayesian model developed with Mark Webster from University of Leeds, we assume the detector only outputs a pulse if  $b$  of the  $n_{par}$  pixels are triggered ( $b$  depends on the bias current and  $n_{par}$  is defined by the detector geometry), and the active area of the detector changes as each pixel arms. We assume even illumination of the pixels, which is valid if the optical spot is positioned equidistantly between pixels. We must first consider dark counts: one may arm the device, meaning a single photon can trigger the detector even in the two-pixel regime, or two must coincide on separate pixels for the counter to register them. For this reason we consider the switching of individual pixels without a photon being absorbed as a ‘dark event’ - not all dark events result in a registered count. Modelling the dark event rate as a Poisson process with rate  $\lambda$  gives probability  $\gamma = 1 - e^{-\lambda}$ . In our model, the total number of dark events  $g$  affect the trigger probability, and have a binomial distribution described as

$$p(g|\gamma) = \binom{n_{par}}{g} \gamma^g (1 - \gamma)^{n_{par}-g} \quad (4.5)$$

where we use binomial notation, which represents

$$\binom{a}{b} = \frac{a!}{b!(a-b)!}. \quad (4.6)$$

Considering then the  $\mu$  incident photons, we have  $\eta$  probability of each to form a hotspot, which gives  $d$  detectable (though doesn’t tell us in which pixels the arming events happen; they could all occur in the same pixel, in which case there would be no trigger). Taking the dark events into account, the chance of having  $d$  arming events is binomial, equal to

$$p(d|\mu, \eta, g) = \binom{\mu}{d} \eta^d \left(1 - \frac{n_{par} - g}{n_{par}} \eta\right)^{\mu-d}. \quad (4.7)$$

The probability of whether a triggering event  $T$  occurs  $\mathbb{P}(T|\mu, \eta, \gamma)$  is formed by multiplying the probability of having a certain number of arming events by the probability of those events being distributed in such a way that at least  $b$  pixels are armed, such

that  $\mathbb{P}(T|\mu, \eta, \gamma) = \sum_{d=0}^{\mu} p(d|\mu, \eta, \gamma)\mathbb{P}(T|d, \gamma)$ . Combining this with the pixels armed by dark counts gives

$$\mathbb{P}(T|\mu, \eta, \gamma) = \sum_{g=0}^b p(g|\gamma) \sum_{d=0}^{\mu} p(d|\mu, \eta, g)\mathbb{P}(T|d, g). \quad (4.8)$$

Solving equation 4.8 is non-trivial for general  $b$ . However, when two pixels are required to cascade ( $b = 2$ ) as in this case, and dark events  $g = 0$ ,  $\mathbb{P}(T|d, g) = (1 - n_{par}^{1-d})(1 - \delta_{d,0})$  where  $\delta_{a,b}$  is the Kronecker delta, equal to one if  $a = b$ , else zero. When  $g = 1$ ,  $\mathbb{P}(T|d, g) = (1 - \delta_{d,0})$ , and when  $g \geq 2$ ,  $\mathbb{P}(T|d, g) = 1$ . In this case, by summing from  $d = 1$ , the  $g = 0$  case becomes  $\mathbb{P}(T|d, g) = (1 - n_{par}^{1-d})$  and the  $g = 1$  case becomes 1, and so with two pixels illuminated equally we have

$$\begin{aligned} \mathbb{P}(T|\mu, \eta, \gamma) &= \sum_{g=0}^b p(g|\gamma) \sum_{d=0}^{\mu} p(d|g, \mu, \eta)\mathbb{P}(T|d, g) \\ &= \sum_{g=0}^2 \binom{2}{g} \gamma^g (1 - \gamma)^{2-g} \sum_{d=2-g}^{\mu} \binom{\mu}{d} \left(\frac{2-g}{2}\eta\right)^d \left(1 - \frac{2-g}{2}\eta\right)^{\mu-d} \mathbb{P}(T|d, g) \\ &= (1 - \gamma)^2 \sum_{d=2}^{\mu} \binom{\mu}{d} \eta^d (1 - \eta)^{\mu-d} (1 - 2^{1-d}) \\ &\quad + 2\gamma(1 - \gamma) \sum_{d=1}^{\mu} \binom{\mu}{d} \left(\frac{\eta}{2}\right)^d (1 - \eta/2)^{\mu-d} + \gamma^2 \\ &= (1 - \gamma)^2 (1 - (1 - \eta)^{\mu} - \mu\eta(1 - \eta)^{\mu-1}) \\ &\quad - 2(1 - \gamma)^2 \sum_{d=2}^{\mu} \binom{\mu}{d} \left(\frac{\eta}{2}\right)^d (1 - \eta)^{\mu-d} (1 - 2^{1-d}) \\ &\quad + 2\gamma(1 - \gamma) (1 - (1 - \eta/2)^{\mu}) + \gamma^2 \\ &= (1 - \gamma)^2 (1 - (1 - \eta)^{\mu} - \mu\eta(1 - \eta)^{\mu-1}) \\ &\quad - 2(1 - \gamma)^2 \left( (1 - \eta/2)^{\mu} - (1 - \eta)^{\mu} - \mu\frac{\eta}{2}(1 - \eta)^{\mu-1} \right) \\ &\quad + 2\gamma(1 - \gamma) (1 - (1 - \eta/2)^{\mu}) + \gamma^2 \\ &= (1 - \gamma)^2 (1 + (1 - \eta)^{\mu} - 2(1 - \eta/2)^{\mu}) \\ &\quad + 2\gamma(1 - \gamma) (1 - (1 - \eta/2)^{\mu}) + \gamma^2 \\ &= 1 + (1 - \gamma)^2(1 - \eta)^{\mu} - 2(1 - \gamma)(1 - \eta/2)^{\mu}, \end{aligned}$$

which can be restated as equation 4.9. This is used to fit the two-pixel data in figure 4.5.

$$R_{detected} = f (1 + (1 - \gamma)^2 (1 - \eta)^{\mu} - 2(1 - \gamma) (1 - \eta/2)^{\mu}) \quad (4.9)$$

This model does not allow for pixels armed in a previous pulse window ('pre-armed' pixels), which is a possibility when operating in the two-pixel trigger regime: the

current redistribution[139] suggests that the unarmed pixels would experience a much higher relative bias while the pre-armed pixel supports little. However, dark events increase with bias, which would thus increase the probability of another pixel triggering before the next pulse and resetting the detector. Pre-arming the detector would give a linear dependence on photon flux where we see a quadratic, suggesting that this effect does not contribute significantly. Current redistribution may reset the detector between pulse windows, resulting in an increased dark count rate.

With two pixels but when only one is required to trigger ( $n_{par} = 2, b = 1, g = 0$ ),  $\mathbb{P}(T|d) = 1 - \delta_{d,0}$  which by summing from  $d = 1$  simplifies to  $\mathbb{P}(T|d) = 1$ . This leads to equation 4.10

$$\begin{aligned} \mathbb{P}(T|\mu, \eta, \gamma) &= \sum_{g=0}^2 p(g|\gamma) \sum_{d=0}^{\mu} \binom{\mu}{d} \left(\frac{2-g}{2}\eta\right)^d \left(1 - \frac{2-g}{2}\eta\right)^{\mu-d} \mathbb{P}(T|d, g) \\ &= (1-\gamma)^2 \sum_{d=1}^{\mu} \binom{\mu}{d} \eta^d (1-\eta)^{\mu-d} + 2\gamma(1-\gamma) + \gamma^2 \\ &= 1 - (1-\gamma)^2(1-\eta)^{\mu}, \end{aligned} \tag{4.10}$$

and so, if we do not take into accounts the dark events ( $\gamma = 0$ ) we see that the existing description of single-pixel triggering in equation 3.5 can be derived. This may be used to fit single-pixel data.

Though the general case is complex, once calculated this model offers a better description of the response of a detector with multiple parallel pixels, as seen in figure 4.2. This model handles dark events in a rigorous manner, and is simple for the purpose of fitting.

## 4.2 Device layout & operation

Parallel-wire variants of SNSPDs[73] offer the possibility of higher count rates[137], thinner wires with higher signal-to-noise[117], and multi-photon detection. These devices, also referred to as cascade-switching detectors or superconducting nanowire avalanche photodetectors (SNAPs)[117], are able to operate in a different regime to single-wire SNSPDs, triggering only on the absorption of at least two photons[74]. Typical geometries employed to date when patterning these devices have 2–24 spatially-indistinguishable, often interleaved nanowires connected in parallel[73, 74, 117, 137]. As a result of this layout, it is impossible to explicitly observe what happens when only one wire of the parallel structure is illuminated, and in turn distinguish one- and two-photon detection. In this work we have fabricated a device with spatially-separated

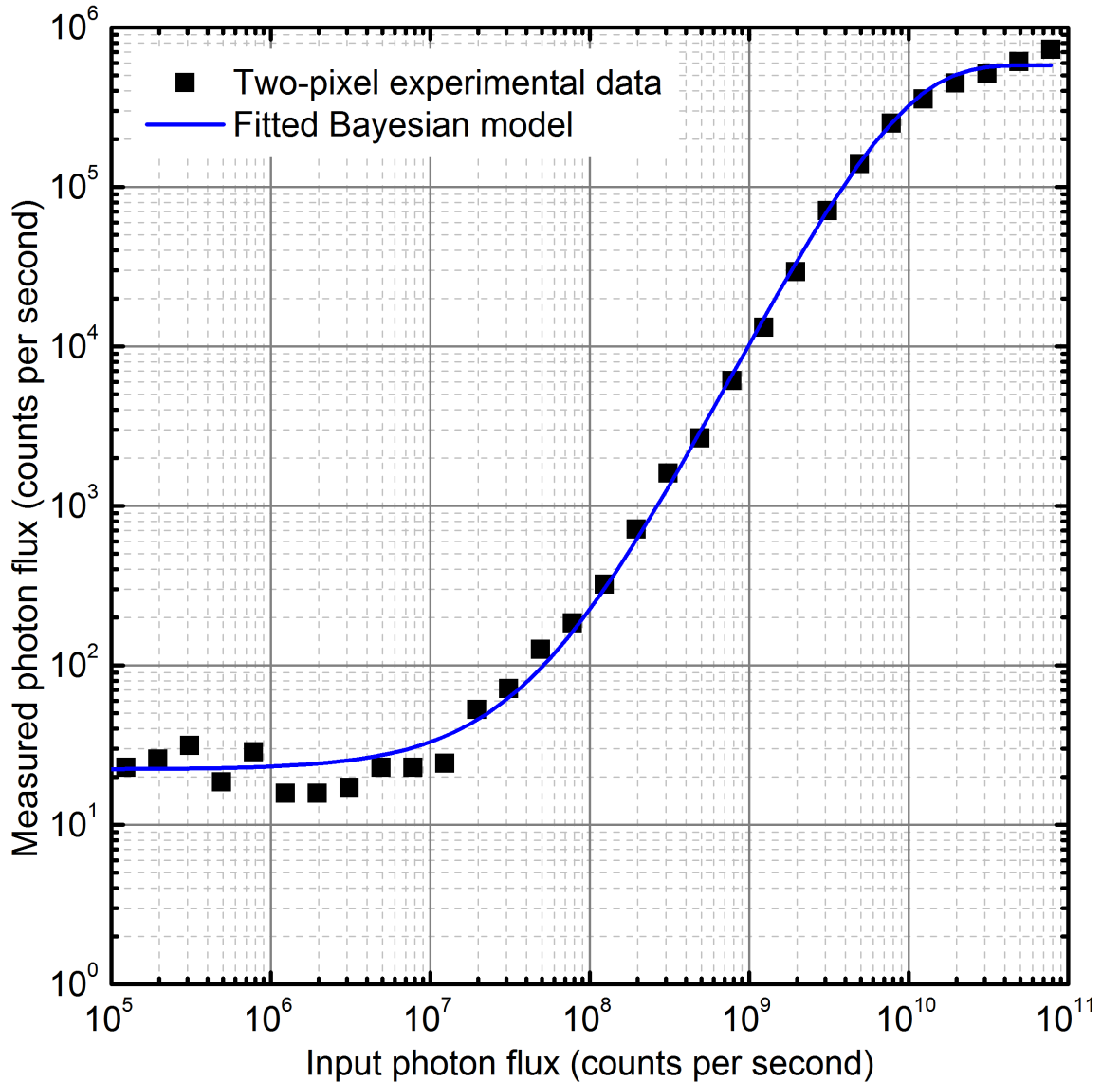


Figure 4.2: Comparison of Bayesian two-pixel triggering model with real data. This is a maximised- $R^2$  fit, with a value of  $R^2 = 0.99219$ , showing good agreement between model and experiment. The fitted  $\eta$  value is  $\eta = 1.59 \times 10^{-4}$ [18].

multiple wires connected in parallel (referred to as pixels) to capture these distinct absorption regimes.

As described in section 3.7, in a parallel-wire SNSPD,  $n$  wires are biased such that, if the bias current is sufficiently low[72] ( $I_b < I_{av}$  where  $I_{av}$  is the avalanche or cascade threshold current), one may absorb a photon without immediately triggering a second. If  $I_b$  is sufficiently near  $I_C$  ( $I_b > I_{av}$ ), a single photon pushing a single wire resistive will trigger the cascade process[73]. It is by operating in the arm-trigger regime that multi-photon discrimination is possible.

To observe the spatially-separate one- and two-photon absorption regimes on a multi-pixel device, one must have a sufficiently small spot of light, and some method of accurately translating this across the device. We have used a miniature confocal microscope with low temperature piezoelectric nanopositioners in previous work[17, 62]

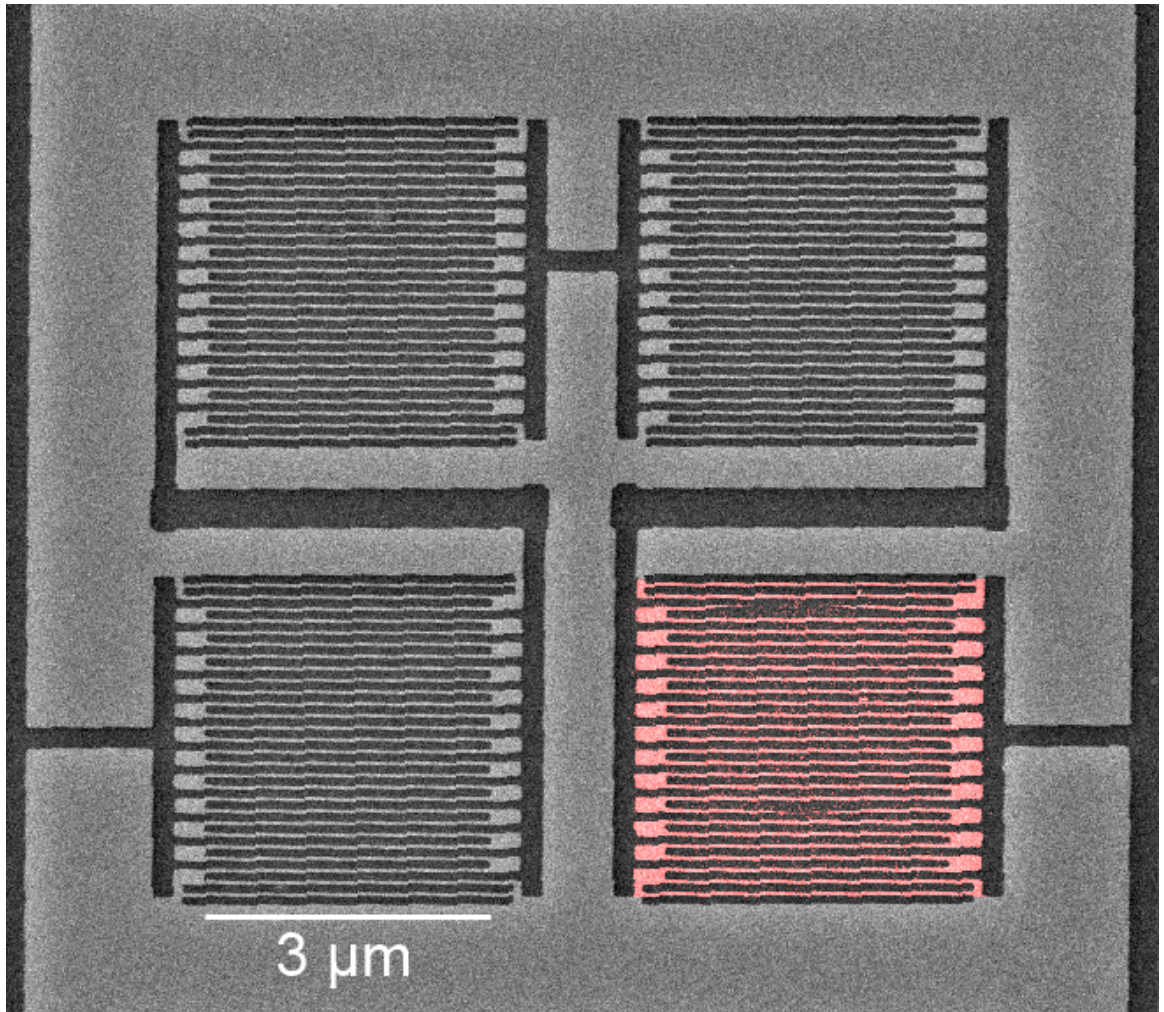


Figure 4.3: Scanning electron microscope (SEM) image of the spatially-separable parallel-wire SNSPD, with NbN bright and substrate darker. Each pixel is spatially separate but electrically connected in parallel. As one pixel (shown in red) failed—the broken wire can be seen clearly—this is in effect a 3-pixel parallel nanowire device. Image courtesy of Dr Lara San Emeterio Alvarez.

which we exploit again for this purpose. Work by others exploring the trigger mechanism of parallel-wire SNSPDs[74] under broad illumination shows that, in a multi-wire device biased at a low  $I_b$ , an arm-trigger mechanism occurs: the first photon will ‘arm’ the device and the second will ‘trigger’ it: unless the device has a trigger pulse as well, or is triggered by a dark-count, the detector will behave as though nothing was detected, and will ultimately reset as the hotspot energy dissipates into the substrate.

The device under test, a spatially-separate multi-pixel SNSPD fabricated in NbN on a sapphire substrate with 55 nm-wide wires at 130 nm pitch, was cooled to 3.5 K in a vibration-damped closed-cycle cryostat based on a pulse-tube refrigerator. The miniature confocal microscope[17] was employed to realise photoresponse maps of the device, which had a film thickness of 8 nm and a superconducting transition temperature of 9 K. A critical current of 21  $\mu\text{A}$  was measured when operated with a 50  $\Omega$  shunt resistor in parallel at 3.5 K. Large meanders were patterned at either end of the active area

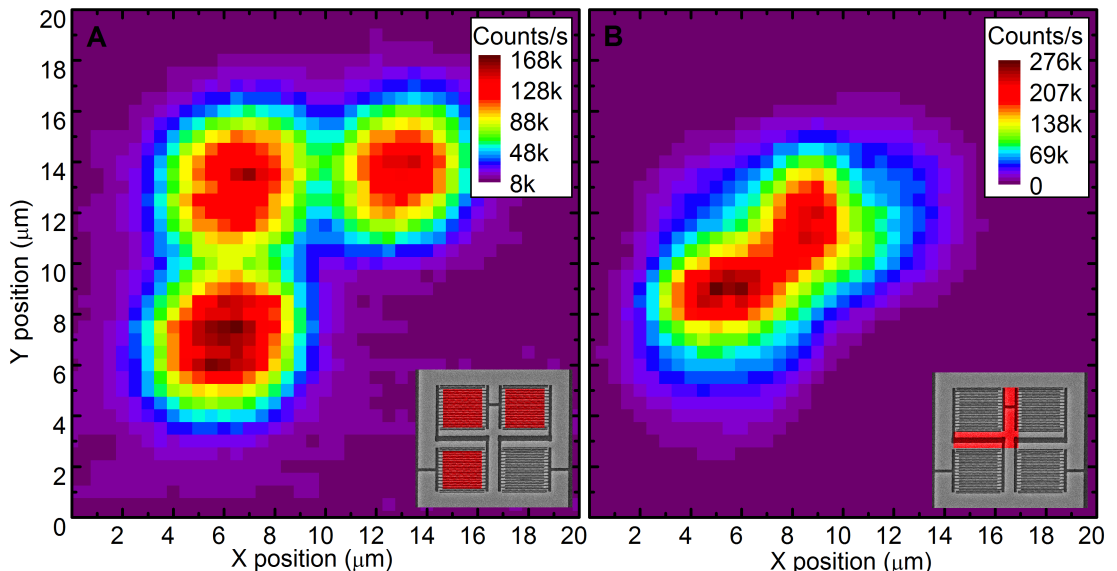


Figure 4.4: Maps of the photoresponse with position of spatially-separable parallel-wire SNSPDs in two bias regimes. **A** is the high-bias ( $0.83I_C$ , 25 photons per pulse) photoresponse with position of the three pixels that were successfully fabricated: it is clear that the lower pixel counts more than the other two, which we attribute to a small non-uniformity in film thickness during fabrication. In **B** we see two-pixel discrimination highlighting the areas where there are two active pixels, which occurs at lower bias ( $0.69I_C$ , 8000 photons per pulse). A small blue ‘halo’ around the between-areas’ response shows that the single pixels still respond in this regime, though at a much reduced rate.

to increase the kinetic inductance of the device which, along with the shunt resistor, allowed it to reset without latching.

Light of wavelength 1550 nm from a 1 MHz pulsed diode laser was delivered by optical fiber into the closed-cycle cryocooler. The light was then collimated in a miniature confocal microscope and focused to a diffraction-limited spot with full-width at half-maximum (FWHM)  $1.3\ \mu\text{m}$  which is able to move relative to the detector. Large-range Attocube piezoelectric motors (5 mm range) allow rough placement of the spot, while a piezoelectric X-Y scanner ( $40\ \mu\text{m} \times 40\ \mu\text{m}$  scan area at 3.5 K, sub-micrometer precision) allows accurate characterisation of the detector response.

To allow readout from the detector for the counts maps in figure 4.4, the device was biased by a voltage source in series with a  $100\ \text{k}\Omega$  resistor and low-pass filter through a bias tee’s direct current (DC) ‘input’. The radio frequency (RF) + DC side was shunted with a  $50\ \Omega$  resistor to allow the detector to reset and connected to the SNSPD. The RF output of the circuit was amplified (gain 56 dB typical, amplifier bandwidth 10 MHz–580 MHz) and connected to a counter.

The SEM image in figure 4.3 shows the layout of the device. Each of the four parallel pixels is  $3\ \mu\text{m} \times 3\ \mu\text{m}$ , though the bottom-right pixel has a broken wire, meaning the device behaves as a 3-pixel device. The photoresponse of the active pixels is shown for

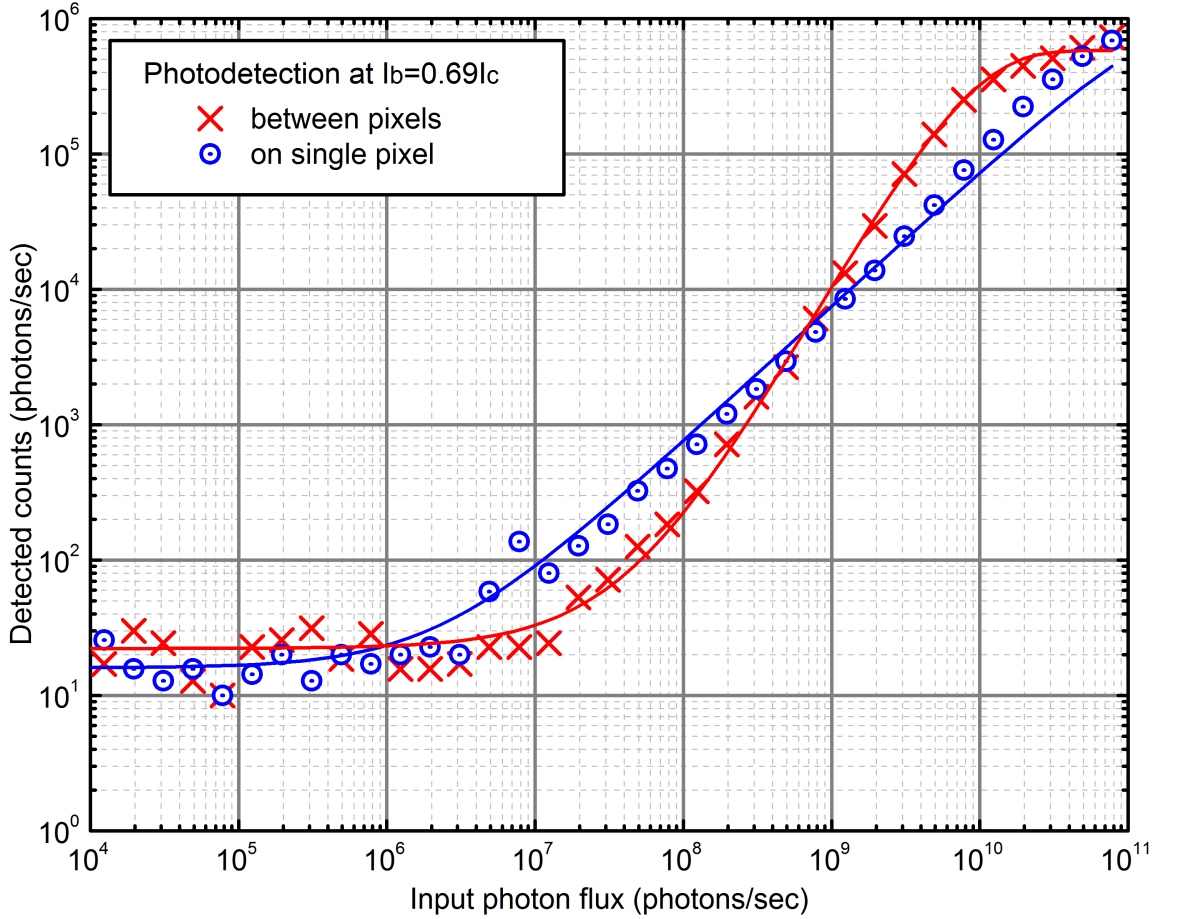


Figure 4.5: Graph of the count rate as a function of photon flux entering the system when illuminating one- and two-pixels at fixed bias current. Maximized- $R^2$  models of photon absorption in these regimes (equations 3.5 and 4.9 respectively) were fitted. In the single-pixel illumination case, the fit has efficiency  $\eta = 7.5 \times 10^{-4}$  and  $R^2 = 0.99165$ , while the two-pixel illumination has efficiency  $\eta = 1.59 \times 10^{-4}$  and  $R^2 = 0.99219$ . The efficiency is expected to fall in the two-pixel case, as much of the optical spot is illuminating the inactive area between pixels. The low bias point ( $0.69I_C$ ) was used to keep the dark-count rate constant, and shows that even at low bias, both one- and two-pixel triggering regimes are possible, albeit with low efficiency.

high bias ( $0.83I_C$ ) in figure 4.4A and for low bias ( $0.69I_C$ ) in figure 4.4B. These plots suggest that the pixels are not perfectly uniform, with the lower pixel approximately 10% more responsive than the other two. The individual pixels respond at high bias, while at low bias and high flux the areas between multiple pixels respond most strongly: this agrees with the concept of an arm-trigger regime at lower bias[74].

### 4.3 Results

As is shown in figure 4.5, equations 4.9 and 4.10 fit well: the two-pixel case is much steeper, which is to be expected as it has a greater dependence on photon flux. The SNSPD transitions seamlessly between the two regimes as the bias current  $I_b$  is varied. At  $I_b = 0.69I_c$  there is clearly both one- and two-pixel triggering occurring. When

operating in the between-pixel illumination regime the device will occasionally trigger on a single pixel, especially at low flux when two-pixel triggering is unlikely. When illuminating on-pixel, some of the light some of the time will form a hotspot on a second pixel and a cascade will happen via the two-pixel process. This effect will cause the data to deviate from the theory, which only describes a single regime at a time.

In figure 4.6, we present the timing properties of the device over different bias and illumination conditions. A time-correlated single photon counting (TCSPC) technique was employed and the device was current-biased through a bias tee, with a  $50\ \Omega$  shunt resistor. The amplified output was run to the input of a PicoQuant PicoHarp 300. The input light at wavelength 1550 nm from a Kphotonics CNT-1550 mode-locked erbium-doped fiber laser was pulsed at 50 MHz with picosecond pulse width, and was split between an InGaAs fast photodiode (intrinsic jitter 15 ps) and the parallel-wire SNSPD. The fast photodiode was connected to the reference input of the PicoHarp. This allows the PicoHarp to measure, in 4 ps bins, the temporal response of the detector with respect to the reference pulse, from which we can obtain the jitter and peak arrival times.

Figure 4.6A, taken illuminating one pixel, shows line plots of the response of the parallel-wire device when one pixel is illuminated as its bias is reduced from its single-photon-sensitive regime. At the peak, the number of counts decreases, and the position is delayed, with the characteristic ‘tail’ explained by Ejrnaes[116] that others also observe[74, 117] in the instrumental response of parallel wire devices becoming more pronounced. This is also shown in figure 4.6C, which more clearly shows the tail.

Comparing figure 4.6A with figure 4.6B which shows the response when two pixels are illuminated, an additional feature is seen—a small bump on the rising edge of the response time peak. As the bias decreases in the two-pixel regime, the dominant peak (single photon response) reduces significantly, while the bump, the two-photon response, becomes stronger until it is more prominent than the single photon response. This is seen in figure 4.6D as protrusion from the single-photon response area, maintaining high count rates per bin to much lower bias than in figure 4.6A. The reduction of the count rate from the on-pixel illumination to the two-pixel is due to the change in active area with respect to the center of the optical spot, while the increased count rates at low bias in the between-pixel illumination regime is due to the absorption of two or more photons on at least two pixels, enabling the cascade process.

Examining the timing properties of the device using TCSPC, on figures 4.6C and d the peak arrival times are displayed. For both one- and two-pixel illumination the ‘single photon’ relative peak arrival time is lowest at high bias, and the FWHM jitter of this peak is narrow, suggesting the device consistently responds quickly. As the bias is decreased, the time to the peak is delayed, and the jitter becomes larger. The change

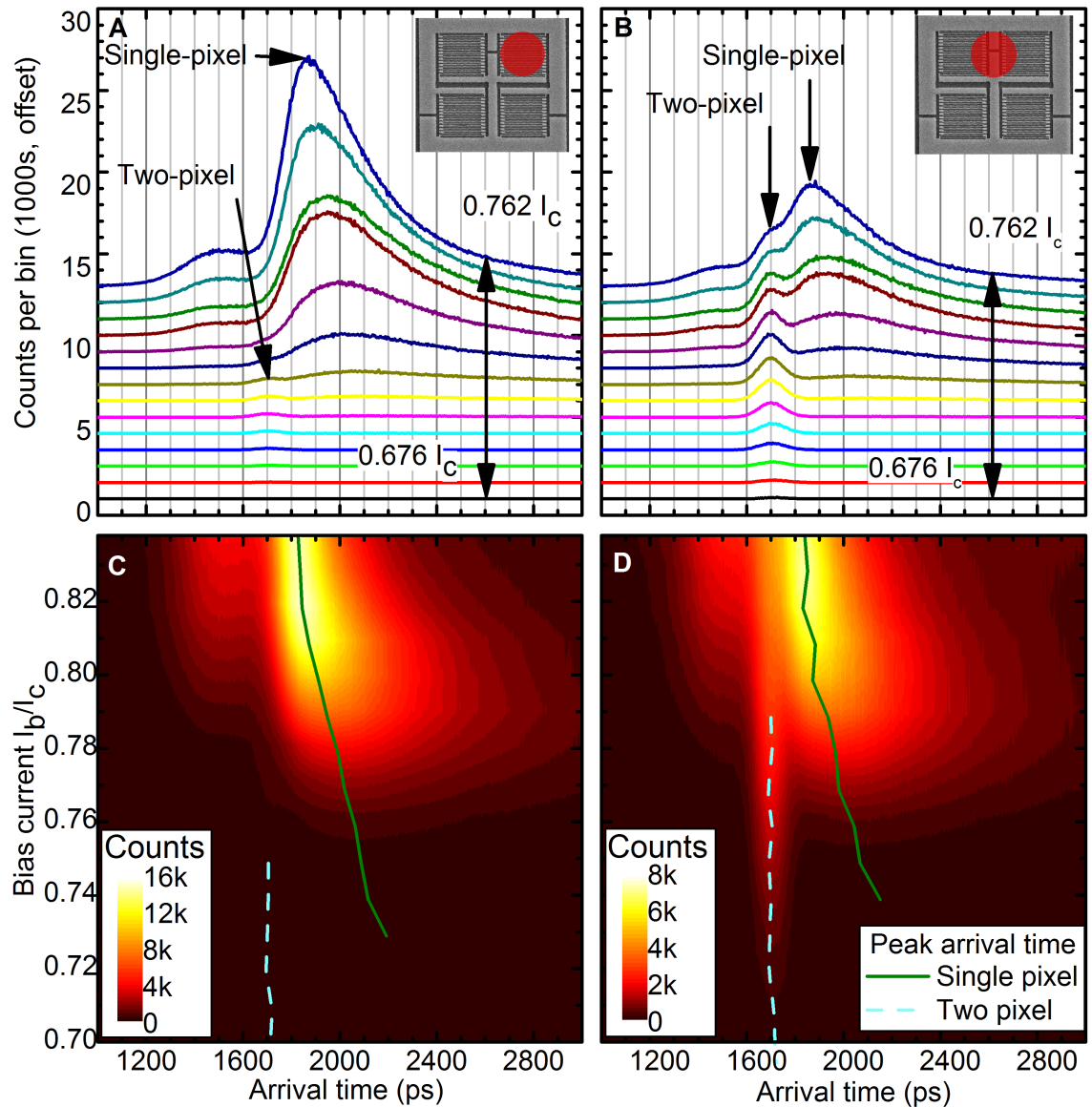


Figure 4.6: The photon arrival time profiles when illuminating one or two elements of a multi-pixel SNSPD. The two cases: figures 4.6A and 4.6C illuminating a single element, and figures 4.6B and 4.6D illuminating two elements. The stacked line section plots are offset in Y to make them more visually distinguishable. As the bias current is reduced in the one-pixel case, the device triggering delay increases, until it triggers no further and the response drops away. In the two-pixel illumination case, the device behaves similar to the one pixel case at high bias, but as the bias is reduced, a second signal peak emerges, ahead of the single photon absorption peak and with comparable FWHM jitter. In this regime we are discriminating two-photon events. The peak arrival times for single- and two-pixel triggering are shown on figures 4.6C and 4.6D for one-pixel trigger (green line) and two-pixel trigger (cyan dash). As the bias decreases and the jitter increases and arrival times are delayed, the count rate of the detectors decreases, which can be seen in figure 4.6C and figure 4.6D.

in relative peak arrival time is greater than other results in the field[117], though none of these feature long meanders and our TCSPC equipment, contrary to some, measures to the peak of the pulse. These factors both independently increase this value. Between  $0.78I_C$  and  $0.74I_C$  for between-pixel illumination there is an overlap in one- and two-pixel triggering regimes, seen in the growing left peak in figure 4.6B and that there are both one- and two-pixel peak arrival times in figure 4.6D. The lack of a distinct switch from one regime to another may be due to the non-uniformity of the device. Even so, these values tie in with electrothermal simulation by Marsili[72], which shows that a uniform device with three wires in similar layout should move to the two-pixel trigger regime at  $0.78I_C$ . Two wires simultaneously arming will divert current to the remaining wire at a faster rate, resulting in the faster relative peak arrival time seen in the ‘two photon’ case.

When illuminating one pixel, some small number of photons are able to strike a second pixel which results in there being a small two-photon response which emerges at  $0.76I_C$ . This is significant enough to show in figure 4.6A, though as is clear from its profile it occurs with very low count rates, and is included for completeness. As the bias is reduced, both the single- and two-photon responses are delayed, as shown in figures 4.6C and D. We also see from the width of the profiles in figures 4.6A and 4.6B there is an increase in the FWHM jitter. A simple electrical model shows that at lower bias, it takes longer for sufficient current to be diverted to the remaining wire for a cascade to take place.

## 4.4 Conclusion

This work presents a single detector capable of spatially distinguishing one- and two-pixel events. At a single bias point, the single-pixel illumination efficiency is  $\eta = 7.5 \times 10^{-4}$ , while the two-pixel illumination efficiency is  $\eta = 1.59 \times 10^{-4}$ : the detector efficiency is not significantly diminished when operating in the two-pixel trigger regime. Additionally, the work demonstrates that the desirable SNSPD timing properties in this regime are preserved.

The particular detector used is a proof-of-concept, and suffers from a low SDE with respect to the state-of-the-art[9]. However, spatial mapping of a multi-pixel parallel SNSPD operating in the two-pixel trigger regime is original. The work is especially notable for being the first spatially-distinguishable demonstration of the one- and two-pixel triggering regimes[18]. Further to this it develops two new models for the detector behaviour when operating in these regimes.

Understanding the device physics of parallel SNSPDs opens the pathway to large-area parallel SNSPDs with extended spectral range, low jitter, short reset times and multi-photon discrimination. In the time between this work being performed and this thesis being written the field has seen developments in multi-pixel detectors, from proof-of-concept readout schemes[78, 79] to a 64-pixel array[77]. Even in light of this, the relative fabrication ease and operation of a two-or-more pixel detector is attractive. The parallel-wire SNSPD remains useful in its own right as the detector element in photon correlation experiments, eliminating the need for a more complex optical system with multiple detectors.

Using a low-temperature nano-optical measurement system this work presents a spatially-distinguishable demonstration of the one- and two-pixel trigger regimes of parallel-wire SNSPDs. This work formulates a theoretical description of the efficiency of these devices, and shows that while it is less efficient in the multi-pixel trigger regime owing to the reduced active area caused by ‘arming’ a single pixel, the timing properties show the device to be faster than when it is operating in single-photon detection mode. This work explicitly demonstrates and describes the temporal features of a spatially-separate parallel-wire SNSPD applicable to short-length and interleaved designs.

# Chapter 5

## Nanoantenna-coupled SNSPDs

Two front-side-coupled silver dipole nanoantennas, simulated to have resonances at 1480 nm and 1525 nm, were fabricated in a two-step process 30 nm above an NbN superconducting nanowire. An enhancement of 50 % to 130 % in the system detection efficiency (SDE) was observed when illuminating the antennas. This offers a pathway to increasing absorption into superconducting nanowires, creating larger active areas, and giving more efficient detection at longer wavelengths.

### 5.1 Introduction

For detection technologies based on superconductivity, and in contrast with single photon detectors based on semiconductors, there is no sharp cut-off in absorption[48, 140] as incident photon wavelength increases; thus superconducting nanowire single photon detectors (SNSPDs) have considerable potential for use at mid-infra-red (IR) wavelengths[141]. However, at longer wavelength photons are less energetic, and detection efficiency suffers. This may be partially mitigated by ultra-thin nanowires[48], but this has a trade-off in the form of the coupling efficiency  $\eta_{coupling}$ . Simply increasing the length of the meandering nanowire will increase the kinetic inductance of the detector, impacting its reset time[69]. One route to increasing the absorption into the meander may be through nanowire-coupled nanoantennas, as discussed in section 2.5.

In this work we design, fabricate, simulate and characterise the response of two silver dipole nanoantennas. The nanoantennas are intended to be resonant around the IR telecoms band to allow for nano-optical photoresponse maps to be obtained using the vibration-damped low-temperature nano-optical system described in section 3.12. Initial finite difference time domain (FDTD) simulations of antenna response were performed by Dr Vincenzo Giannini and Prof Stefan Maier at Imperial College London, London, UK; later simulation, presented here, was performed by the author. Fabrica-

tion was performed by Dr Shigehito Miki at the National Institute of Information and Communication Technology, Kobe, Japan.

## 5.2 Device layout & simulation

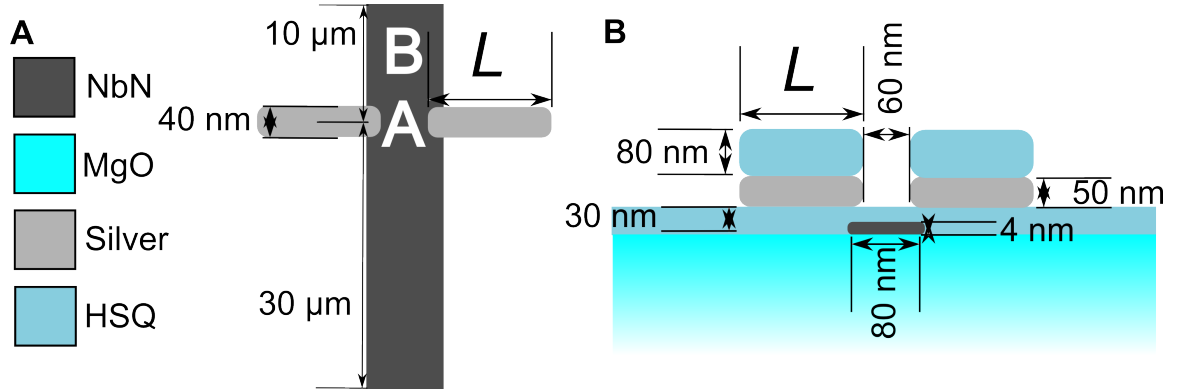


Figure 5.1: Schematic of the layout of the nanoantenna device. This outlines the simulation setup used to model the power absorbed into the nanowire. It matches the modified design described in section 3.2. Length  $L$  is a key determining factor in the resonance of the antenna. Two design length  $L_{des}$  values were fabricated and tested:  $L_{des} = 220$  nm, and  $L_{des} = 210$  nm. **A** is looking top-down, while **B** is a cut-through along the direction of current flow in the nanowire.

The nanowire was patterned in a thin film of NbN on an MgO substrate. The exact dimensions of the antennas are shown in figure 5.1, top-down in **A** and in-plane with the wire in **B**. The antenna length  $L$  defines the resonance wavelength the antenna will enhance most. The SNSPDs and nanoantennas were fabricated according to the steps detailed in section 3.2.

Two antenna lengths were designed  $L_{des} = 220$  nm, and  $L_{des} = 210$  nm. As is seen in the scanning electron microscope (SEM) shown in figure 5.2**A**, these were fabricated successfully. By simulating as a guide for the initial design and then fitting the observed photoresponse resonance retrospectively, it is possible to determine to a higher degree of accuracy the likely antenna dimensions. These are referred to as the actual antenna length  $L_{act}$ . We will ultimately see that the design length  $L_{des} = 220$  nm corresponds to an actual length nearer  $L_{act} = 240$  nm, and the  $L_{des} = 210$  nm antenna corresponds to a length nearer  $L_{act} = 225$  nm. In order to avoid ambiguity we introduce these lengths now, and note that they are within the measurement error of the SEM image.

The incident power absorbed into the nanowire was modelled using the FDTD method in Lumerical FDTD Solutions. The simulation parameters are shown in figure 5.1. These simulations modelled the power absorbed at each point. This allows a cut-through ‘slice’ of the absorbed power both on- and off-resonance, shown in figures 5.2**B** and **C** for the  $L_{act} = 240$  nm antenna.

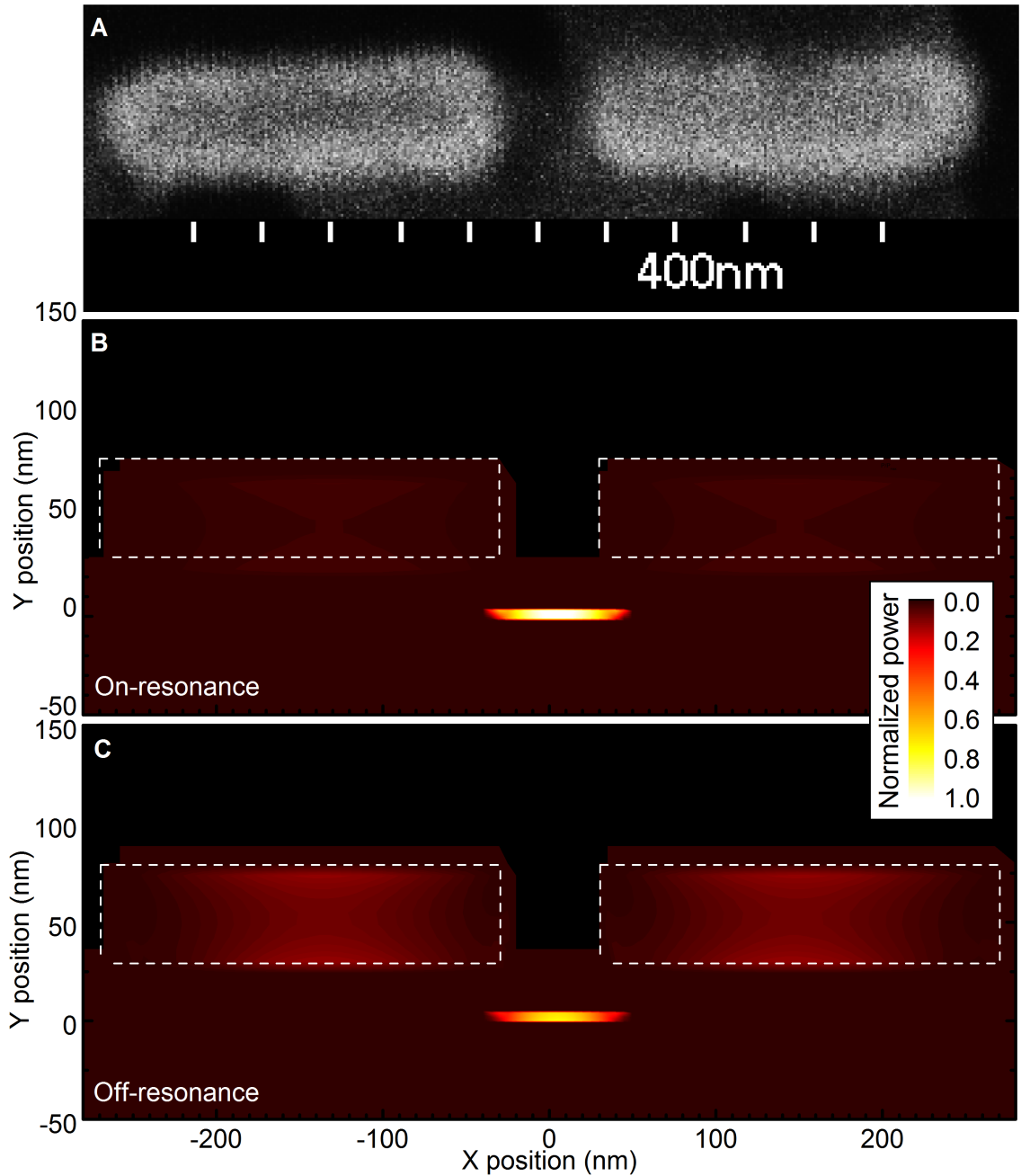


Figure 5.2: SEM and simulation of the nanoantenna. **A** is a top-down SEM image (comparable with figure 5.1A) courtesy of Dr Alessandro Casaburi showing the  $L_{des} = 220$  nm nanoantenna. From this it is clear that the fabricated nanoantenna length is actually  $L_{act} = 240$  nm. The nanowire is not visible due to being buried under 30 nm  $\text{SiO}_x$ . After etching, residual hydrogen silsesquioxane (HSQ) resist remains on the surface. **B** shows a normalized slice of the simulation of the absorbed power for the  $L_{act} = 240$  nm antenna on-resonance: most of the power is absorbed into the NbN nanowire. Companion plot **C** is off-resonance: much more of the power is absorbed into the nanoantennas in this case. The antennas are marked with white dashed lines.

On-resonance it is clear that the majority of the power is absorbed into the nanowire, peaking at the normalized maxima 1.00 in the middle of the nanowire; off-resonance, the antenna absorbs a significant amount, and the peak power in the nanowire reaches only 0.65 of the maxima.

The total power absorbed into the entire length of the nanowire was obtained from the simulation, and was the most readily comparable metric with the SNSPD's SDE. These simulations suggested a resonance wavelength  $\lambda_{res}$  for the  $L_{act} = 240$  nm nanoantenna of  $\lambda_{res} = 1525$  nm, while the  $L_{act} = 225$  nm nanoantenna's simulated resonance wavelength was  $\lambda_{res} = 1480$  nm, as seen in figure 5.3A. The crossing of the polarisation sensitivity in the 'no antenna' case is attributable to an unavoidable numerical artifact: a 13% reflection from the SiO spacer and the simulation boundary reaches a resonance condition at 1540 nm, enhancing absorption in all polarisations and obscuring the true polarisation sensitivity of the wire. We explored the parameter space to ensure this artifact is understood and small enough not to significantly influence the results with an antenna, and thus can be discounted. It is estimated that a small wire of these dimensions could have a degree of polarisation of less than 100%, but is too small to become fully unpolarised[127]. This is consistent with experimental observations (figure 5.4).

The simulations were employed to assess expected behaviour if the nanowire was misaligned with the nanoantenna, shown in figure 5.3B for the  $L_{act} = 240$  nm nanoantenna. Due to the HSQ cap and the low profile of the nanowire it was not possible to resolve the nanowire in the SEM. For a small misalignment the peak resonance wavelength (red) is pushed to lower wavelengths and the absorbed power decreases (blue), until a misalignment of 60 nm, when the peak resonance moves below 1340 nm, the lowest wavelength of our tunable lasers. Subsequently, we can determine that if our experimental setup is able to characterize the resonance peak, the upper bound on the misalignment of the nanowire and nanoantenna is less than 60 nm.

The detector tested had a 9  $\mu$ A critical current when cooled to 3.5 K in a vibration-damped cryostat based on a closed-cycle Cryomech PT403-RM pulse-tube cryorefrigerator. Light was delivered by fibre, to a miniature confocal microscope configuration with a spot of 1.3  $\mu$ m[17], and was used to illuminate the nanoantenna detectors from the front side. The wavelength of the input light was varied from 1340 nm to 1650 nm, a spectral range of 310 nm, in 5 nm steps.

Light was inserted from a combination of an Agilent HP 8168F (range 1440 nm to 1590 nm) and two modules in a Yenista OSICS rack: an ECL-1400 (range 1340 nm to 1440 nm) and T100-1620 (range 1560 nm to 1680 nm) through an electronically-controlled optical switch. This was then passed through two Agilent 8156A variable optical attenuators connected in series to reduce the input photon flux, and was then

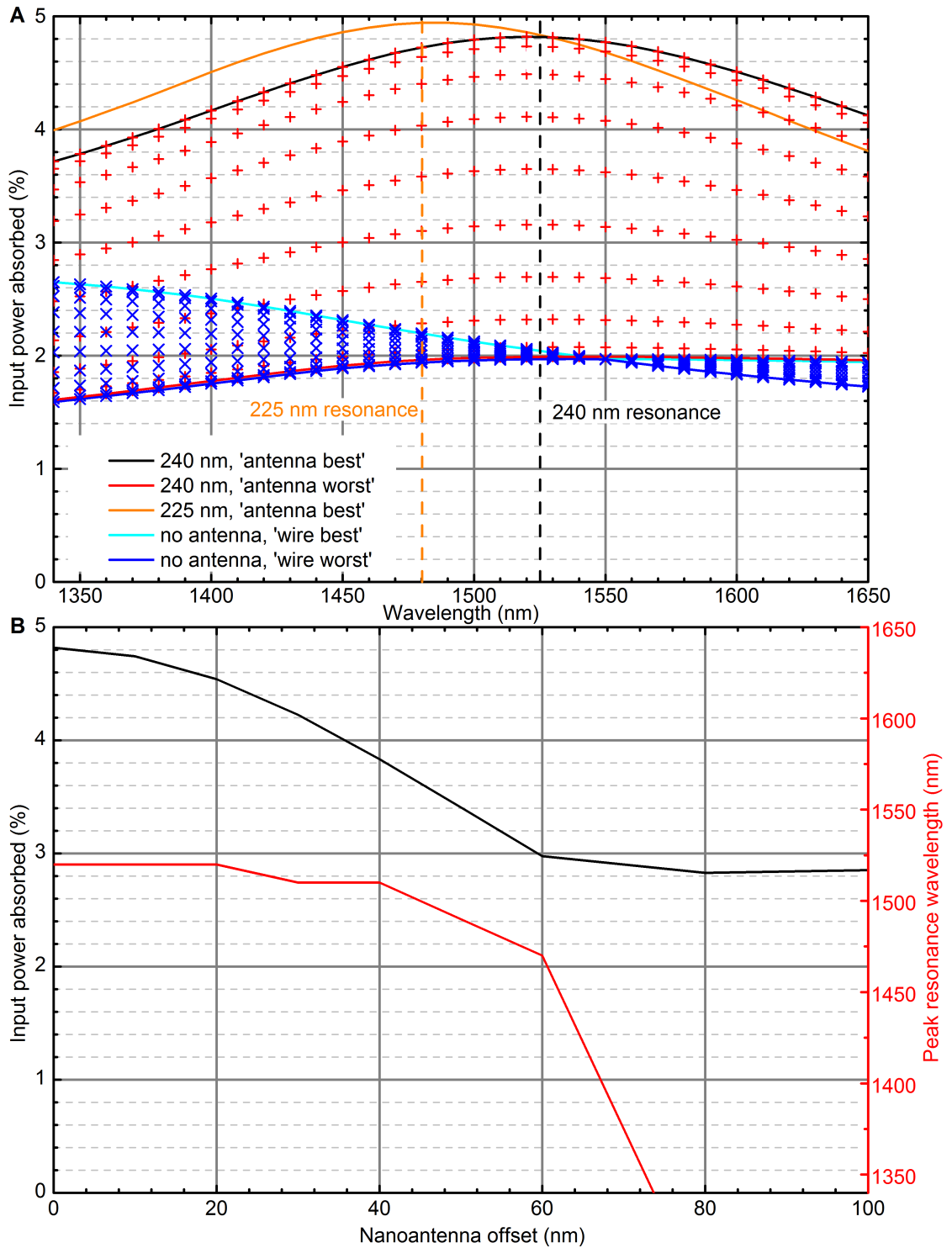


Figure 5.3: Simulation results of nanoantenna behaviour with wavelength and misalignment. The output of simulation of the total absorbed power into the nanowire is shown in **A** across a range of linear electric field polarisations. Red pluses represent the  $L_{act} = 240$  nm antenna simulation data, and are bounded by a black line and a red line to denote the ‘antenna best’ and ‘antenna worst’ responses to incident light. Blue crosses represent the bare nanowire photoresponse, bounded by a cyan line and a blue line to denote ‘wire best’ and ‘wire worst’. Additionally, the ‘antenna best’ response for the  $L_{act} = 225$  nm antenna is shown in orange for later comparison, and the resonances of the antennas are marked with dashed lines. Determining the effect of offsetting the nanoantenna from its location centrally over the nanoantenna is shown in **B**. For comparison with detector photoresponse note that these models do not consider the SNSPD triggering probability  $\eta_{trig}$ , which is wavelength-dependent.

passed through an Agilent 11896A electronic polarisation controller. At this point, to calibrate the incident light, the power was measured across the range with 0 dB applied attenuation at the input to the cryostat. The power meter, a Thorlabs PM 300, was disconnected and the fibre connected to the cryostat's optical input. The detector response was tested, and afterwards the laser power profile was re-tested to confirm the stability of the laser power. The power meter and attenuators have calibrations traceable to the National Institute of Standard and Technology.

A power variation of 3 dB was observed across the wavelength range of the lasers, as described in section 3.14. The varying power of the laser was normalized out afterward: the applied attenuation and laser power were summed and the photon flux calculated. From this it was possible to determine the SDE at each wavelength and electric field polarisation. The optical attenuators were calibrated between 1340 nm and 1650 nm, so all measurements were within this range.

It was important to control the electric field polarisation during this experiment as both nanowires and nanoantennas are polarisation-sensitive. Measuring the electric field polarisation at the detector is non-trivial as this is at 3.5 K, so a relative measurement scale is used: the computer-controlled polariser is deterministically swept across a number of positions of the Poincaré sphere and the 'best' and 'worst' count rates are used as positions of reference. From literature one might expect the 'wire best' polarisation to be a linear polarisation in-line with the wire, and 'wire worst' to be a polarisation perpendicular to the wire[67] but these were observed for a meander geometry SNSPD, which is fundamentally a diffraction grating, and so may not necessarily apply here. Simulation suggests that the power absorbed into the nanowire peaks when polarisation is in-line with the antenna, and that the antenna behaves worst when the polarisation is in-line with the wire (which would not excite an antenna resonance). We are reluctant to assert that these are necessarily 'antenna best' and 'antenna worst' without a more rigorous study connecting SDE and absorbed power into the nanowire. Furthermore, the simulation was limited to linear polarisations, and so ignored elliptical and circular polarisations. Subsequently, the 'best' and 'worst' labels are used only in reference to what is empirically observed.

Electric field polarisations cannot be assumed to be maintained as the lasers change and each laser sweeps wavelength. For this reason, at every wavelength, a scan through the electric field polarisation space was taken, and the 'wire best' and 'antenna best' polarisations were extracted retrospectively. As the polarisation sweeps were made using a computer-controlled polariser it was possible to compare the exact response of two spatially-distinct regions of the detector, allowing comparisons for each polarisation from both the antenna and the bare wire. The locations used are shown in figure 5.1A as the white A and B over the nanowire.

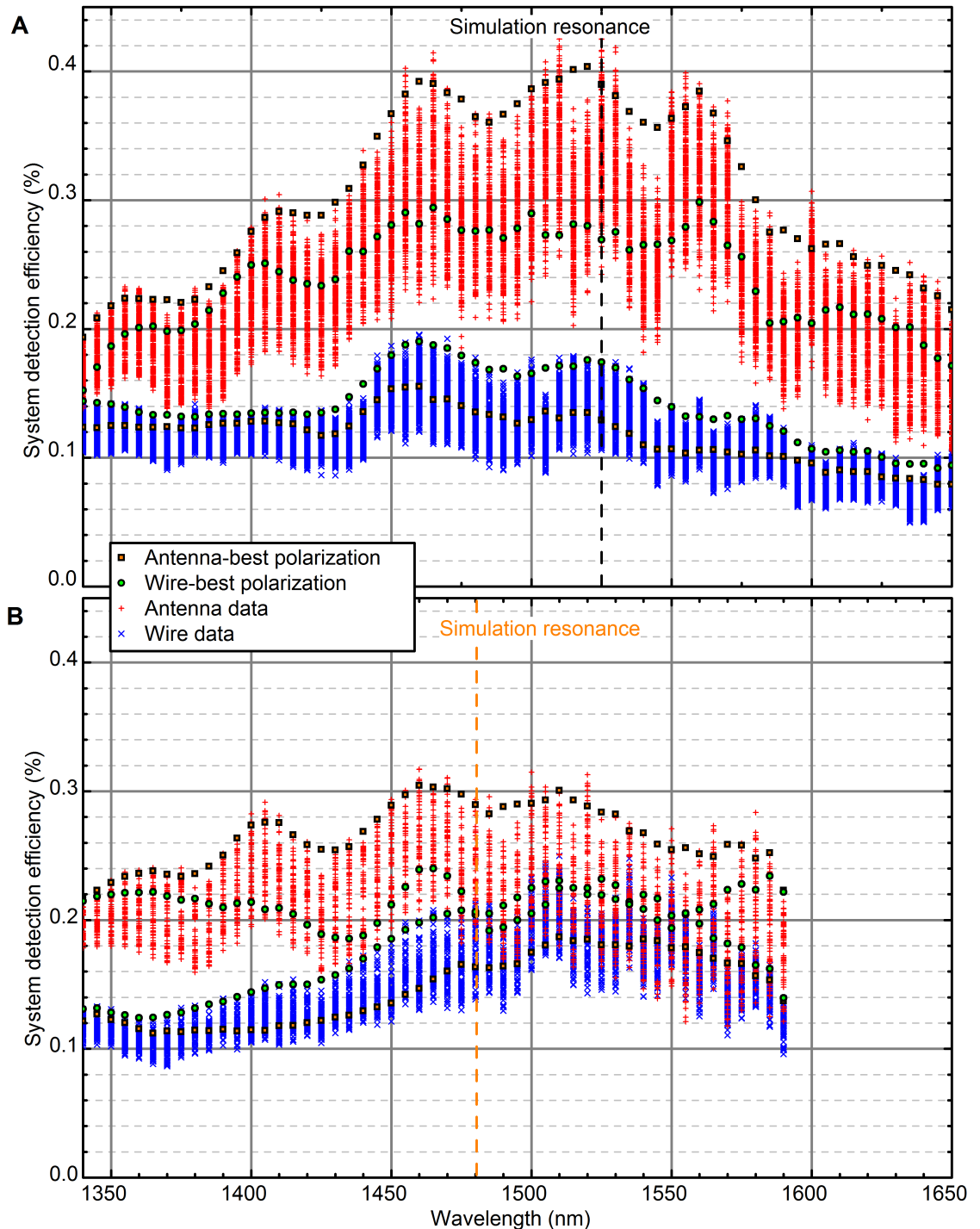


Figure 5.4: Graph of system detection efficiency of two nanoantennas as wavelength sweeps resonance. By sweeping the wavelength from 1340 nm to 1650 nm in 5 nm steps and normalizing out the photon flux using a separate power measurement it is possible to observe the range of efficiencies at each wavelength across the full polarisation space. In **A** the polarisations at which the  $\lambda_{res} = 1525$  nm nanoantenna and wire respond best are selected. **B** shows the response for the  $\lambda_{res} = 1480$  nm nanoantenna. The peak value data for these figures was averaged over the four adjacent points to smooth out the interference. There is clear agreement between the peak efficiency value and the simulation's suggested resonance (shown as a dashed line, comparable with figure 5.3A). **A** sampled 256 polarisations per wavelength while **B** sampled 64: separate testing showed no improvement using 256 points over 64, and it was quicker to measure fewer polarisations.

Looking at the detector response when the wavelength of the incident light is varied we are able to observe the nanoantenna resonance in the photoresponse of the detector. There are some oscillations in the SDE with wavelength, but as others have noted[140] these are an interference effect. In this case, the spacing of the oscillations suggests a characteristic length of about  $75\ \mu\text{m}$  which doesn't immediately stand out as any designed characteristic length, but as noted the data in figures 5.4A and 5.4B have been given a 5-point moving average, and the data was only taken every 5 nm, which means this could be an alias of a larger characteristic length.

### 5.3 Results

Figure 5.4A shows the 1525 nm-resonant nanoantenna's response and the response from the bare wire. At the 'antenna best' polarisation, there is strong enhancement over the response of the bare wire at the same polarisation: furthermore, the 'antenna best' polarisation and the 'wire best' are different, which is expected as both the nanoantenna and nanowire are polarisation-sensitive, and these are perpendicular. The enhancement at the resonant wavelength is 130 %, the SDE increasing from 0.17 % to 0.40 %. Looking at figure 5.4B, which is the 1480 nm-resonant nanoantenna response and response from bare wire, the resonance wavelength seen, as simulation suggested, is lower, but the enhancement is less strong, going from an SDE of 0.20 % to 0.30 %, an increase of 50 %. Whether this is due to poor fabrication or poor alignment with the nanowire is unclear, but the effect is still a net improvement of the photoresponse at the design wavelength.

Using the low-temperature piezoelectric miniature confocal microscope described in section 3.12, we map the photoresponse of the 1525 nm-resonant detector with sub-micrometer precision. By varying the polarisation we are able to spatially visualise the polarisation sensitivity of the detector. Figure 5.5 shows photoresponse from the nanowire and antenna with different polarisations of incident light. The nanowire runs horizontally through the image, with the antenna at about  $10\ \mu\text{m}$  along the wire's photoresponse. In figure 5.5A we see the 'antenna worst' polarisation: the antenna has only a small effect, boosting the wire response of 0.15 % to 0.25 %. Rotating the polarisation to the 'antenna best' polarisation, we obtain figure 5.5B: the nanoantenna responds much more strongly, enhancing the SDE from 0.15 % to 0.37 %. This qualitatively agrees with the FDTD simulation of the absorbed power into the nanowire: divergence in absolute values likely stems from the simulation ignoring the SNSPD trigger probability being wavelength dependent.

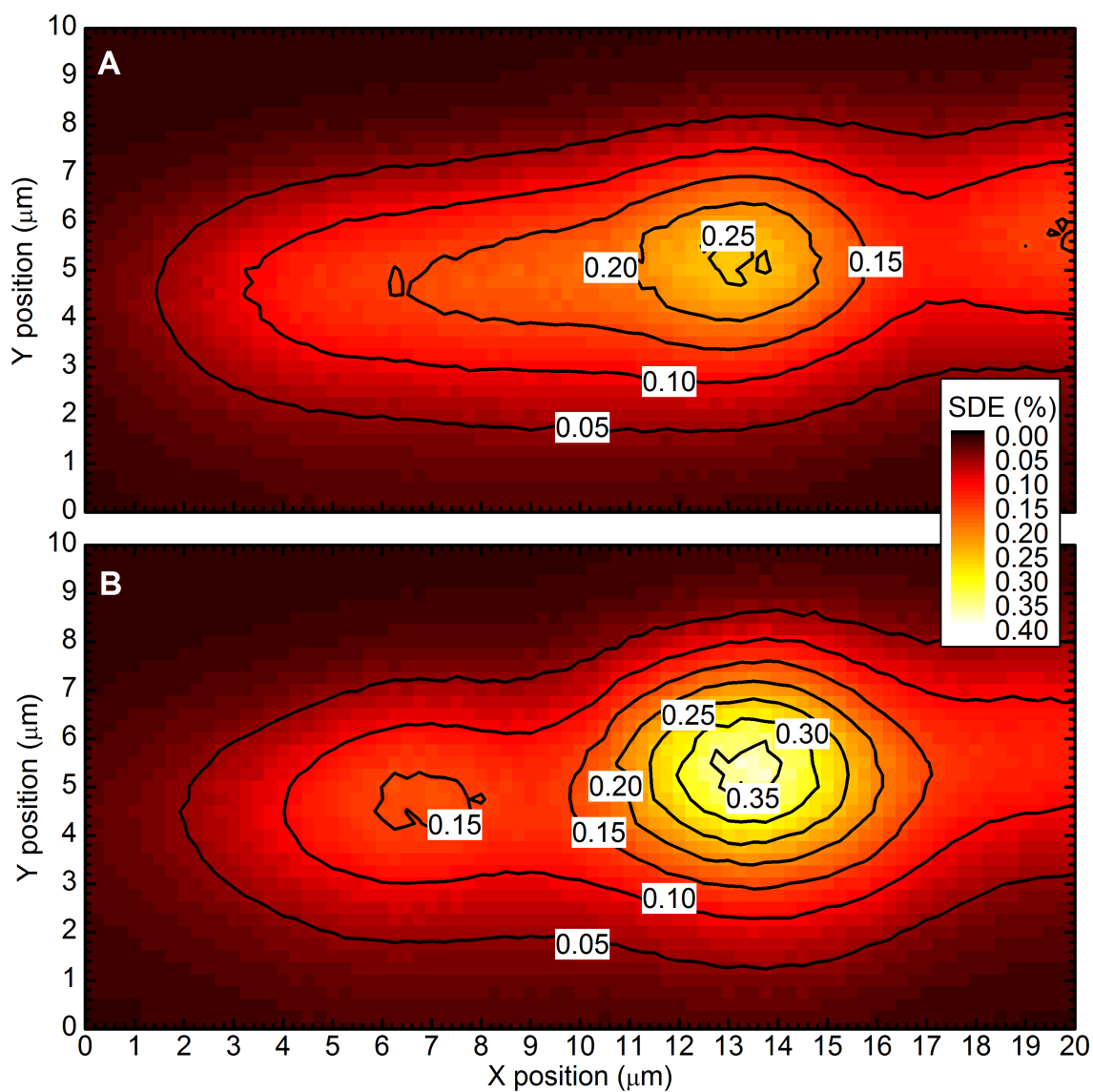


Figure 5.5: Spatial maps of the photoresponse when illuminating a nanoantenna. By raster-scanning the miniature confocal microscope over the active area of the SNSPD, maps of the photodetection profile are created. **A** shows a map of the nanowire when the incident light is polarised with the electric field such that the antenna responds least, the so-called ‘antenna worst’ polarisation. **B** is the same spatial area, with the polarisation rotated to give the highest response from the antenna, the ‘antenna best’ polarisation. There is significant improvement on ‘antenna worst’ response at ‘antenna best’, and it is clear that in both cases the antenna has a positive effect on the detection rate.

## 5.4 Conclusion

This work presents two nanoantennas with different resonant wavelengths, successfully fabricated atop superconducting nanowires. These were comprehensively characterized at low temperature. From comparing the position of the photoresponse resonance with simulation we can conclude that the nanoantennas had less than 80 nm of misalignment with the nanowire. The nanoantennas increased absorption into the nanowire, so creating a localised region of increased SDE with a separate polarisation sensitivity, and offered a 50 % to 130 % improvement in the local SDE.

Coupling an SNSPD to a resonant nanoantenna at telecoms wavelengths is a technical accomplishment in terms of fabrication, and creating spatial maps of the photoresponse offers a key insight into the device behaviour[19]. State-of-the-art SNSPDs are not typically coupled to a nanoantenna as less lossy methods of increasing the absorption such as integrated cavities[9, 66] become more common, but there has been interest in using them nevertheless[104–106].

This approach offers a route to improving SNSPD efficiency at longer wavelengths, out to the mid-IR, and could be employed to create larger-area detectors with a reduced fill factor. It may also offer a route to reducing the polarisation sensitivity of meander structures. Future work may look at increasing the number of antennas, and decreasing the gap between the antennas, to increase enhancement.

# Chapter 6

## Tunable-cavity embedded SNSPDs

A route to increasing the absorption of incident light into the nanowire has been to use reflectors behind the superconducting nanowire single photon detector (SNSPD). This has been widely adopted[64, 66, 142, 143]. By replacing the simple reflector with a distributed Bragg reflector (DBR), further enhancement at a given wavelength can be obtained[110]. This enhancement may be increased further still by inserting the light through a DBR mounted on the fibre, creating an optical cavity. We find good agreement with simulation, achieving increased absorption in low-system detection efficiency (SDE) devices, resulting in a 1.4 times increase in the SDE for 1560 nm light when using a simple reflector, and a similar increase for 1550 nm light when using a DBR substrate.

### 6.1 Introduction

A limiting factor for SNSPD development has been absorption of incident light into the nanowire. In previous work demonstrating the working principles of an optical-cavity-embedded SNSPD, the authors calculated a radiation absorption coefficient  $\eta_{absorption}$  for NbN of only 15% at a wavelength of 1310 nm[64]: clearly, high-efficiency SNSPDs would be impossible without some method of increasing the absorption. The simplest solution is to reflect transmitted light back through the nanowire. Injecting light between two reflective surfaces, an optical cavity, offers a significant improvement, as detailed in section 2.6. Using DBRs instead of simple reflective surfaces allows still further absorption, at the expense of broadband response: this is because DBRs operate by constructive interference and so must be designed for a specific wavelength.

In this work we design and construct a fibre-coupled tunable optical cavity, initially with a simple mirror, and then with a more complex DBR substrate. Tuning is per-

formed using a combination of continuous-wave tunable lasers for wavelength and low-temperature piezoelectric positioners for cavity length.

## 6.2 Device layout & operation

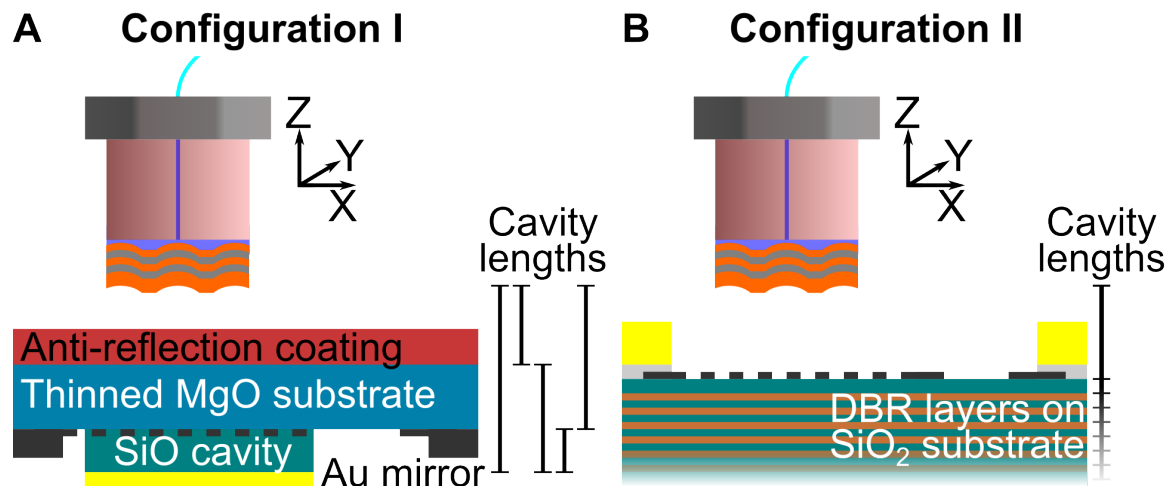


Figure 6.1: Diagram of the two optical cavities formed with Configurations I and II. In both, light arrives through the fibre ferrule which is mounted on low-temperature piezoelectric motors, passing through the DBR layers on the tip. This creates a tunable optical cavity with the reflector deposited behind the SNSPD. In **A**, which depicts Configuration I, the light is back-side coupled to the SNSPD through 250 nm of anti-reflection fluoropolymer, and a 45  $\mu\text{m}$  thinned MgO substrate. The reflector, 100 nm of gold, is mounted on 250 nm of SiO spacer. The possible cavity lengths from reflective interfaces are shown by the lengths demarcated to the right of the diagram: the full length, from the fibre to the mirror, is expected to be strongest, due to the high reflection from the Ag. In **B**, which depicts Configuration II, the light is front-side coupled to the SNSPD, and reflects off the DBR layers directly behind the SNSPD. This has a single cavity with an indeterminate length.

Diagrams of the optical cavities were given in figure 3.29, a figure sufficiently important to easily reference that it is reprinted here as figure 6.1. Both detectors formed an optical cavity with the DBR fibre, fabricated as shown in figure 3.27. This is a hemispherical cavity, stable when the cavity separation is below the radius of curvature of the DBR microlens array. This is experimentally verified in figure 6.2.

### 6.2.1 Configuration I: gold reflector SNSPD

This detector was a back-side-coupled device on MgO with a gold reflector fabricated on a layer of SiO<sub>2</sub>, provided by Dr. Shigehito Miki at the National Institute of Information and Communications Technology, Kobe, Japan. The fabrication process is detailed in literature[143], and the device is shown diagrammatically in figure 6.1A. This substrate had been reduced to a thickness of just 45  $\mu\text{m}$  to enable back-side coupling while keeping

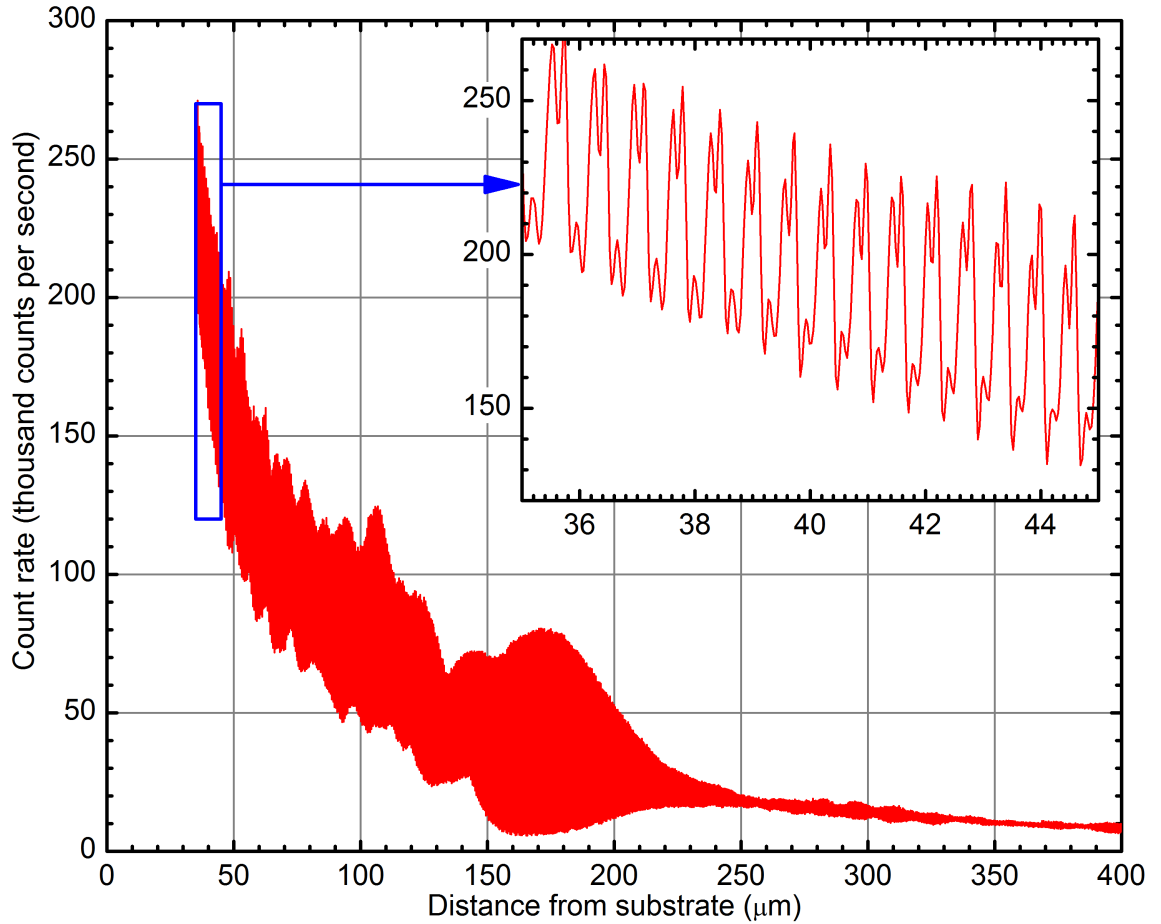


Figure 6.2: Cavity behaviour with increasing air gap length. The initial position was measured using optical coherence tomography (OCT) and determined to be  $(35 \pm 1)$   $\mu\text{m}$  from the substrate. From there, the DBR fibre was stepped away from the detector, and at each point the count rate of the SNSPD was measured. The position was determined by measuring the total distance travelled and dividing by the number of steps. Shown inset is the behaviour of the system over 10  $\mu\text{m}$  nearest the detector: the cavity oscillations are clearly visible. The distance from substrate does not include the 45  $\mu\text{m}$  MgO, which has an optical length of about 80  $\mu\text{m}$ . Subtracting this length from the expected stable cavity length of 250  $\mu\text{m}$ , the cavity should become unstable at an air gap of 170  $\mu\text{m}$ . We observe the cavity oscillations fall away as the  $Z$  displacement increases through this point, showing that the cavity is indeed stable when near the detector.

the coupling efficiency  $\eta_{coupling}$  high. The detector had a  $15\ \mu\text{m}$  by  $15\ \mu\text{m}$  active area with  $100\ \text{nm}$ -wide wires and  $200\ \text{nm}$  pitch fabricated on a  $4\ \text{nm}$  film of NbN, and a had critical current  $I_C$  of  $6\ \mu\text{A}$  and transition temperature  $T_C$  of  $9\ \text{K}$ .

### 6.2.2 Configuration II: DBR SNSPD

This detector was fabricated on a DBR substrate, with the SNSPD fabricated from an NbTiN film. The fabrication is discussed in depth in section 3.3, and the device is shown diagrammatically in figure 6.1B. The result was a front-side-coupled detector with  $90\ \text{nm}$ -wide wires,  $180\ \text{nm}$  pitch on an  $8\ \text{nm}$  film, and had a  $10\ \mu\text{m}$  by  $10\ \mu\text{m}$  active area. The detector had a critical current  $I_C$  of  $11.5\ \mu\text{A}$  and a transition temperature  $T_C$  of  $11\ \text{K}$ .

## 6.3 Simulation

Using Thin Films Center’s Essential Macleod, it is possible to create a one-dimensional model of the behaviour of the system as a layered stack. As with any model, this requires several assumptions. The first assumption is that the system is able to be approximated as linear. The second is that the materials used match the index values used in the simulation. The third is that the meander of the SNSPD is able to be approximated as a thinner film.

In the first case, the system is able to be approximated as linear when using the DBR fibre and when using a bare fibre. However, when the system is using a bare fibre, the fibre must be modelled as being made of air: modelling it as being made of glass will create plane-parallel cavity, which will have an effect on the results. These cavities are highly unlikely in the real setup as they are very unstable: a small error in the alignment and light will escape the cavity.

Source	Wavelength (nm)	$n$	$\kappa$
Tanner, 2010[64]	1310 nm	4.17	5.63
Dorenbos, 2011[144]	1550 nm	$4.7 \pm 0.5$	$6 \pm 0.5$
Miki, 2013[142]	1550 nm	4.563	4.911

Table 6.1: Reported complex refractive indexes for NbTiN

In the second case, while we have refractive index  $n$  and extinction coefficient  $\kappa$  values for NbN which the SNSPD in Configuration I is fabricated from at a range of wavelengths, these are not readily available for NbTiN used for Configuration II, and the particular film we have used has not undergone ellipsometry. Values in literature vary,

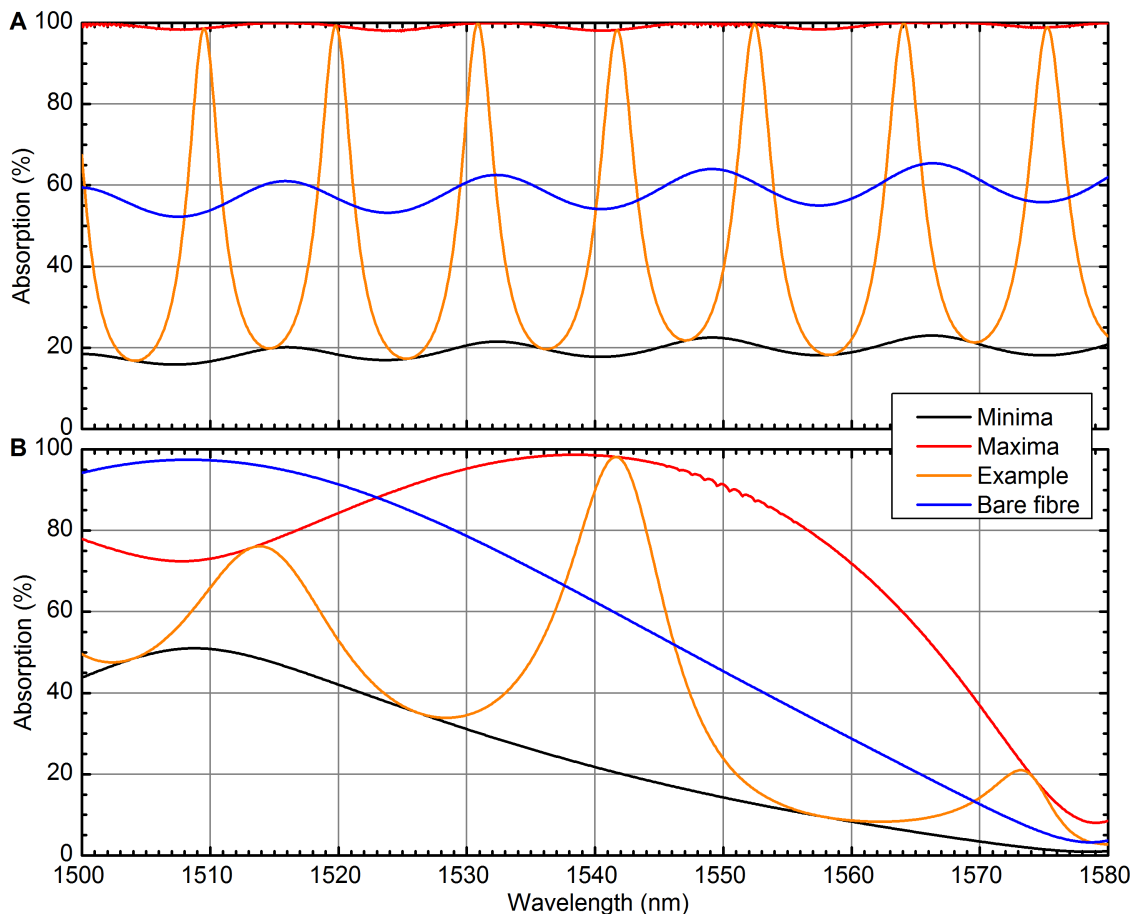


Figure 6.3: Simulation of the absorbed power in two optical cavities with and without DBR fibre. **A** shows the result of simulation of Configuration I, while **B** shows the result of simulation of Configuration II. By varying the cavity length over  $5\ \mu\text{m}$  and making a simulation every  $25\ \text{nm}$  it was possible to select the maxima and minima for both systems. These are shown as red and black lines. Example behaviour is shown in orange at a particular cavity length. For comparison, the bare fibre result is included.

as per table 6.1[64, 142, 144, 145], which is likely a product of the varying relative compositions of the films tested. Furthermore, for both of these, ellipsometry testing is performed at room temperature, and as such may be inaccurate at low temperature. As such, and because the film thicknesses typically vary, we rely on tuning of the parameters to match the experimental data, using the established values as a guide.

In the third case, we are left with little option but to accept the assumption that the patterned meander can be approximated as thin film. Owing to the lack of accurate  $n$  and  $\kappa$  data, we are unable to perform finite difference time domain (FDTD) simulations in two- or three-dimensions. However, this assumption is not without precedent: when used in previous studies it has agreed with data[64].

With these assumptions in mind, we are able to perform the simulations seen in figure 6.3. These demonstrate the expected response of the system described. As is seen in figure 6.3**A**, the absorption of a bare fibre illuminating Configuration I can be improved from 60% to near the maximum by the DBR fibre creating an optical cavity.

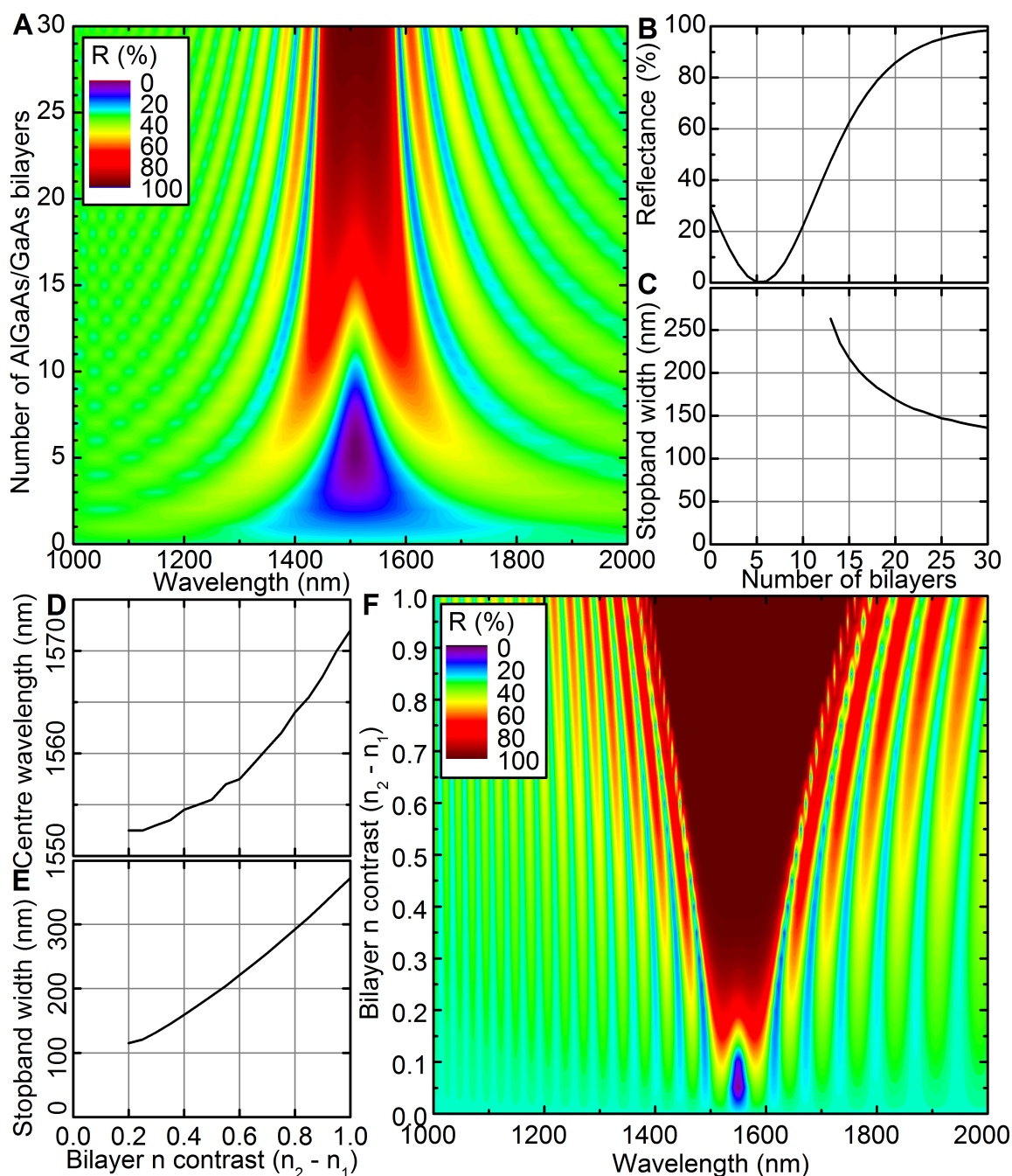


Figure 6.4: Simulation of DBR behaviour with varying refractive indices and number of bilayers. **A** shows the simulated reflectance of a system with the fabricated thickness parameters and refractive indices across a number of bilayers. **B** and **C** show the reflectance at the measured centre wavelength (1510 nm) and width of the stopband respectively. **D**, **E**, and **F** show the effect of varying the contrast of the two materials that make up the DBR, and show the position of the centre wavelength, stopband width, and reflectance with contrast. This was done by setting the substrate's refractive index  $n_2 = 3.3$ , approximately the value for GaAs at 1550 nm, and varying  $n_1$  such that  $2.3 \leq n_1 \leq 3.3$ . The stated stop band widths are full-width at half-maximum (FWHM).

Shown in figure 6.3B is the simulation of the behaviour of Configuration II. Due to imprecise fabrication, the resonance of the substrate that was intended to be at 1550 nm was at 1510 nm, shown in the graph in the bare fibre behaviour. With the addition of the DBR fibre it is possible to move this resonance wavelength, and by tuning the cavity length an  $\eta_{absorption}$  at a wavelength of 1550 nm of  $>90\%$  is possible where it would be  $<50\%$  without.

To verify the validity of these simulations, a study of the reflectance of the bare DBR was performed, shown in figure 6.4. This varied the number of bilayers of the reflector, and separately the refractive index of the AlGaAs. The DBR's reflectivity across the expected stopband was measured and matched simulation, shown in figure 6.5. From these results we can confirm that for the materials chosen we have a stopband of 130 nm FWHM centred around 1510 nm, and that 30 bilayers were required for at least 98% reflectance. The use of a  $\lambda/2$  layer causes a significant degradation in the reflected signal for low bilayer number, but is required to allow localisation of the field within the thin film[110].

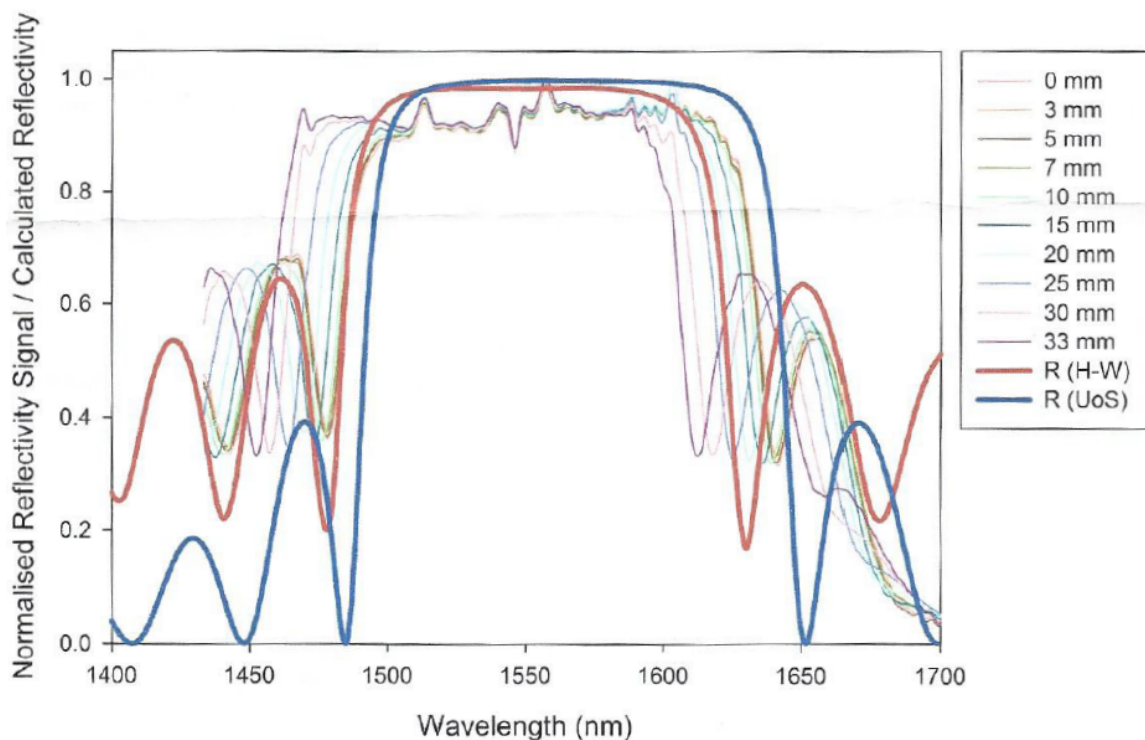


Figure 6.5: Room-temperature reflectivity spectra of the DBR. The experimentally-observed reflectivity (thin lines) was taken at various distances from the surface. Two models, one by the University of Sheffield who performed the deposition and one by Dr Michael Tanner at Heriot-Watt are indicated with thick lines. Image courtesy of University of Sheffield.

## 6.4 Results

The detectors were nano-optically tested using the system described in section 3.12 with the miniature confocal microscope being replaced by the DBR fibre described in section 3.13.1. This gave the system the possibility of tuning an optical cavity, allowing experimental confirmation of what was simulated. In addition, a set of results were taken where the DBR fibre had been replaced with a bare ferrule, creating a simple reflection instead of a cavity. This allowed comparison of the cavity behaviour with the regular approach of simple reflectors.

While the piezoelectric motors move uniformly, the resistive readout of the  $Z$  motor had a margin of error that makes it unsuitable for use when measuring small cavity lengths. There are two further methods of measuring the position with a high degree of accuracy. The OCT technique described in section 3.8.1 is able to measure the cavity length before tuning occurs. After the cavity has been swept over the tuning length, the position is measured again. This allows the intermediate positions to be inferred, and achieves good results. The second method uses the fringe spacing when sweeping the wavelength, as detailed in section 3.13.2. This allows a confirmation of the distance measured by OCT. A proof of the agreement between these two measurements is provided in section 3.13.2.

Both devices were tested in this system.

### 6.4.1 Configuration I results

The Configuration I SNSPD was cooled to 3.4K and aligned with the DBR fibre to form a cavity. The wavelength was tuned across a 60 nm range, centred on 1550 nm. The cavity length was also tuned. The parameters used were employed in an Essential Macleod simulation. The result of the simulation and experiment is seen in figure 6.6. The simulation's wire thickness parameter was tuned to match the absorption found experimentally: this data is a simulated 6 nm thick film. Given the unclear nature of the film behaviour in a meander when modelled in a one-dimensional simulation, and of the variation in film thickness expected, that the simulation fits with a value of the same order of magnitude is reassuring. In both cases, the colour scale has been set to run from the next round value above the peak value to half of the peak value, and using this there is good agreement between the features seen in each.

As seen in figure 6.7, an improved SDE is obtainable using the tunable cavity over using the bare fibre. The minimum and maximum values are selected from the data shown in figure 6.6B. The bare fibre data was taken in a separate cycle of the closed-cycle cryostat, and while it was matched to the parameters used in A, it is not perfectly

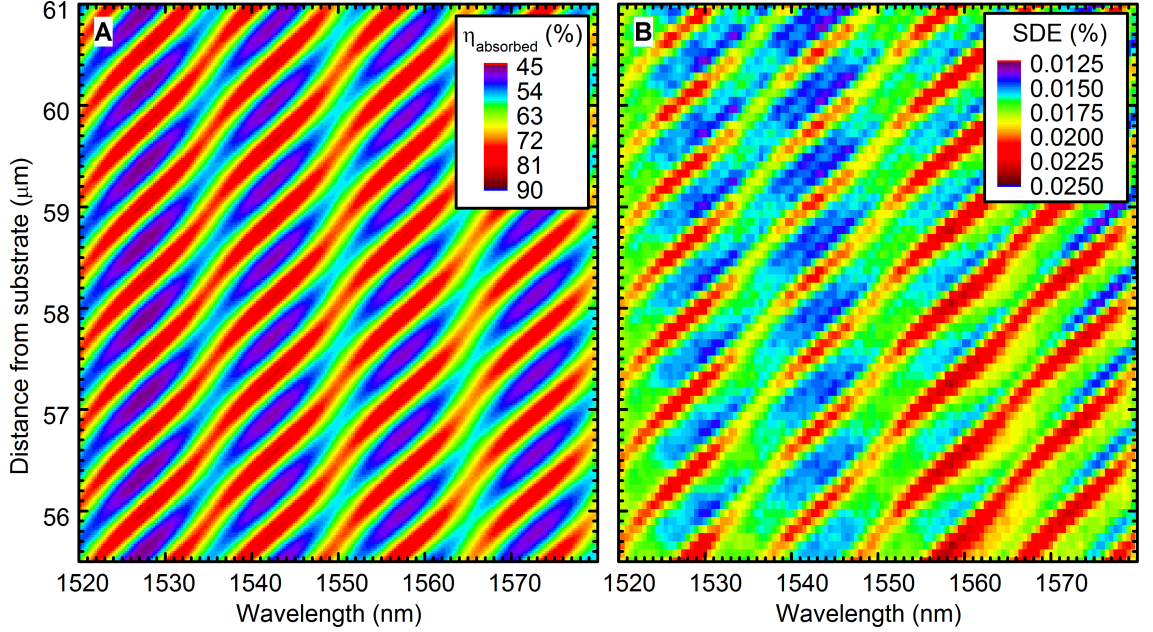


Figure 6.6: Tuning NICT back-side-coupled SNSPD cavity: simulation and experimental result. **A** shows a simulation of the absorption in the cavity over the length from the fibre to the surface of the MgO of 55.5  $\mu\text{m}$  to 61  $\mu\text{m}$ . **B** shows the experimental result tuning the cavity over the same range. In both cases, the incident photon wavelength is swept from 1520 nm to 1580 nm. The features are in agreement, with similar relative changes in the efficiency.

comparable, hence it is plotted separately. Acknowledging this, we see an increase in the SDE from 0.017 % at 1560 nm to, when properly tuned, 0.24 %, an improvement of 1.4 times.

When using both the bare and DBR fibre, the polarisation of the input light was adjusted to achieve the maximum count rate. Prior testing of the equipment revealed that the polarisation of the laser used was stable over the small range used in this test.

## 6.4.2 Configuration II results

The Configuration II SNSPD was cooled to 3.5 K. As with the Configuration I device, the wavelength was tuned, as was the cavity length: in this experiment, a wider tuning range was used, as the features are more broad than in the simple reflector case. The parameters used experimentally were used in a one-dimensional Essential Macleod simulation. The simulation and result are seen in figure 6.8.

There is a greater degree of disagreement between the simulation and the experimental result for this device: notably, the simulation suggests a bimodal distribution when there is a DBR fibre, where the experimental result is a single peak. It is important to consider the complexity of a DBR substrate in light of this: a relatively small error in the deposition could easily shift resonances, and it is quite probable there are

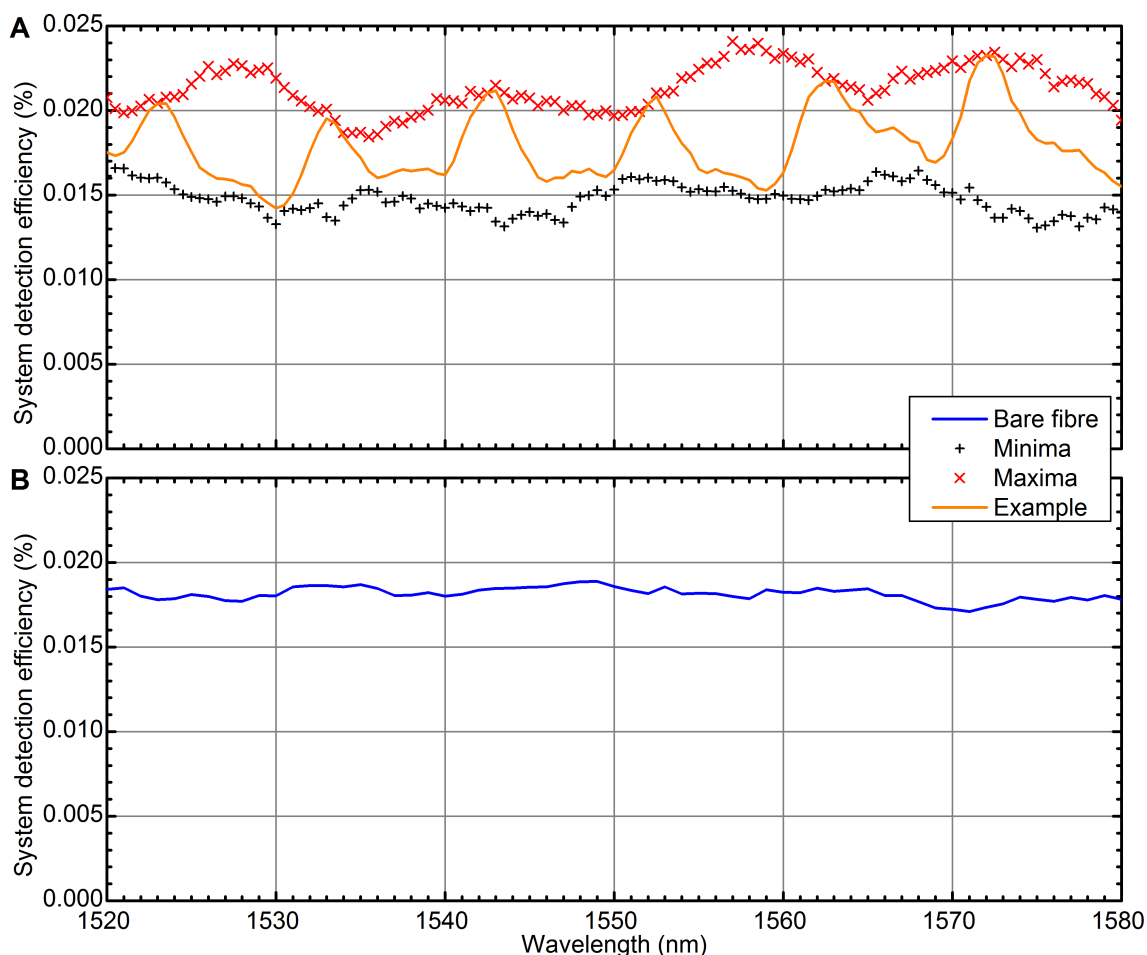


Figure 6.7: Graphs of SDE tuning range of Configuration I, shown in **A**, and comparison with bare fibre, shown in **B**. Post-selected maxima and minima are shown as individual points. An example set of data is given when using the DBR fibre to illustrate the response and peak spacing. The bare fibre data are shown in a separate graph as the data are not directly comparable, because factors such as the coupling efficiency might vary. Using OCT it was possible to match the length from the end of the fibre to the substrate, which is why the SDE is of the same magnitude. The behaviour matches the simulation in figure 6.3A: the bare fibre has only a small SDE dependence on wavelength, while the tunable cavity has a more visible oscillation. By forming and tuning the cavity with the DBR fibre, an improved count rate is obtained with wavelength. By selecting suitable cavity length, this can be positioned at 1550 nm wavelength.

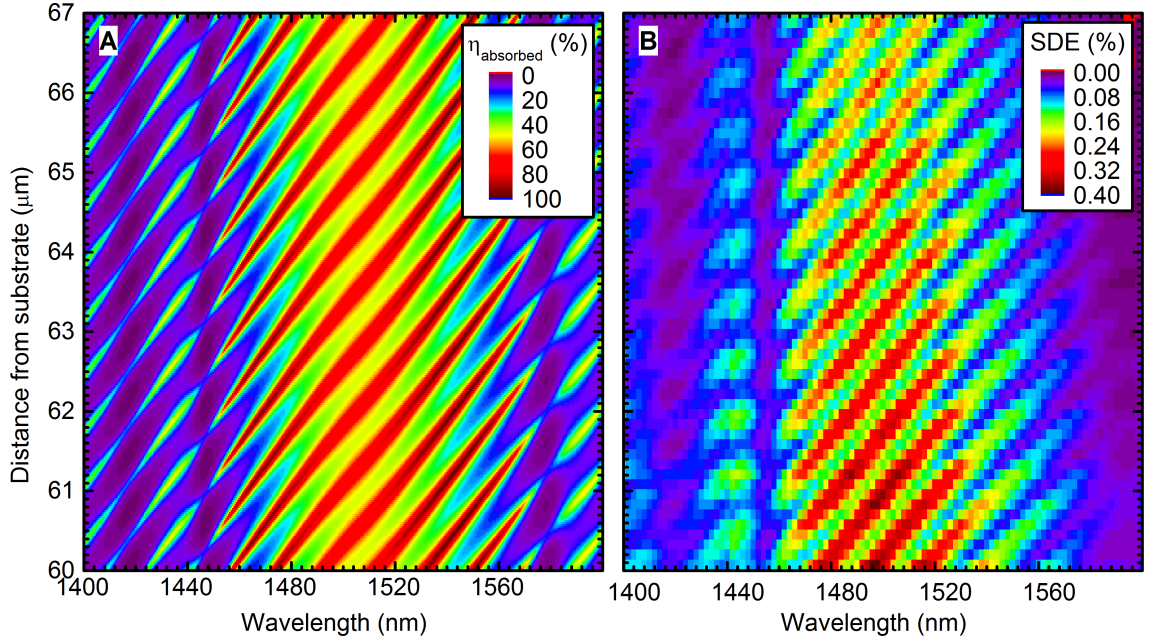


Figure 6.8: Tuning front-side-coupled DBR SNSPD cavity: simulation and experimental result. **A** shows a simulation of the absorption in the cavity over the length from the fibre to the surface of the MgO of 60  $\mu\text{m}$  to 67  $\mu\text{m}$ . **B** shows the experimental result tuning the cavity over the same range. In both cases, the incident photon wavelength is swept from 1400 nm to 1600 nm. In the experimental data the SDE reduces as the cavity length is increased, which is not seen in the simulation: this is a limitation of the one-dimensional simulation being unable to model the spot size changing and reducing  $\eta_{\text{coupling}}$ . Accepting this, the features are in agreement, with similar relative changes in the efficiency.

inhomogeneities in between theoretically identical layers. If this is not a systematic error it could lead to a general ‘blurring’ of the features, which in turn could manifest as a single peak.

However, even in light of the disagreement between simulation and experimental result, the cavity structure still performs largely as designed: a strong resonance effect is seen. This is able to be tuned in the wavelength range suggested, leading to an increase in the efficiency for photons of 1550 nm wavelength. The tuning range is shown more clearly in figure 6.9A.

Unlike in figure 6.7, the parameters for positioning the fibre were unable to be matched for the data in figure 6.9, as the dark count rate increased past a certain cavity length, which we attribute to some part of the fibre mount coming into contact with the surface of the SNSPD. Subsequently, we cannot simply calculate a figure of merit comparable to the 1.4 times SDE increase seen for Configuration I. However, we can determine that, for a bare fibre (figure 6.9B) at 1550 nm the SDE is 0.49%, compared to a peak value of 1.47% at 1500 nm. So,  $\eta_{1550\text{nm}} = 0.33\eta_{1500\text{nm}}$ . Seen in figure 6.9A, by tuning correctly it is possible to get an SDE of 0.17% at 1550 nm, and the peak SDE at 1500 nm is 0.37%: so, we have  $\eta_{1550\text{nm},\text{DBR}} = 0.46\eta_{1500\text{nm},\text{DBR}}$ . From this we can see

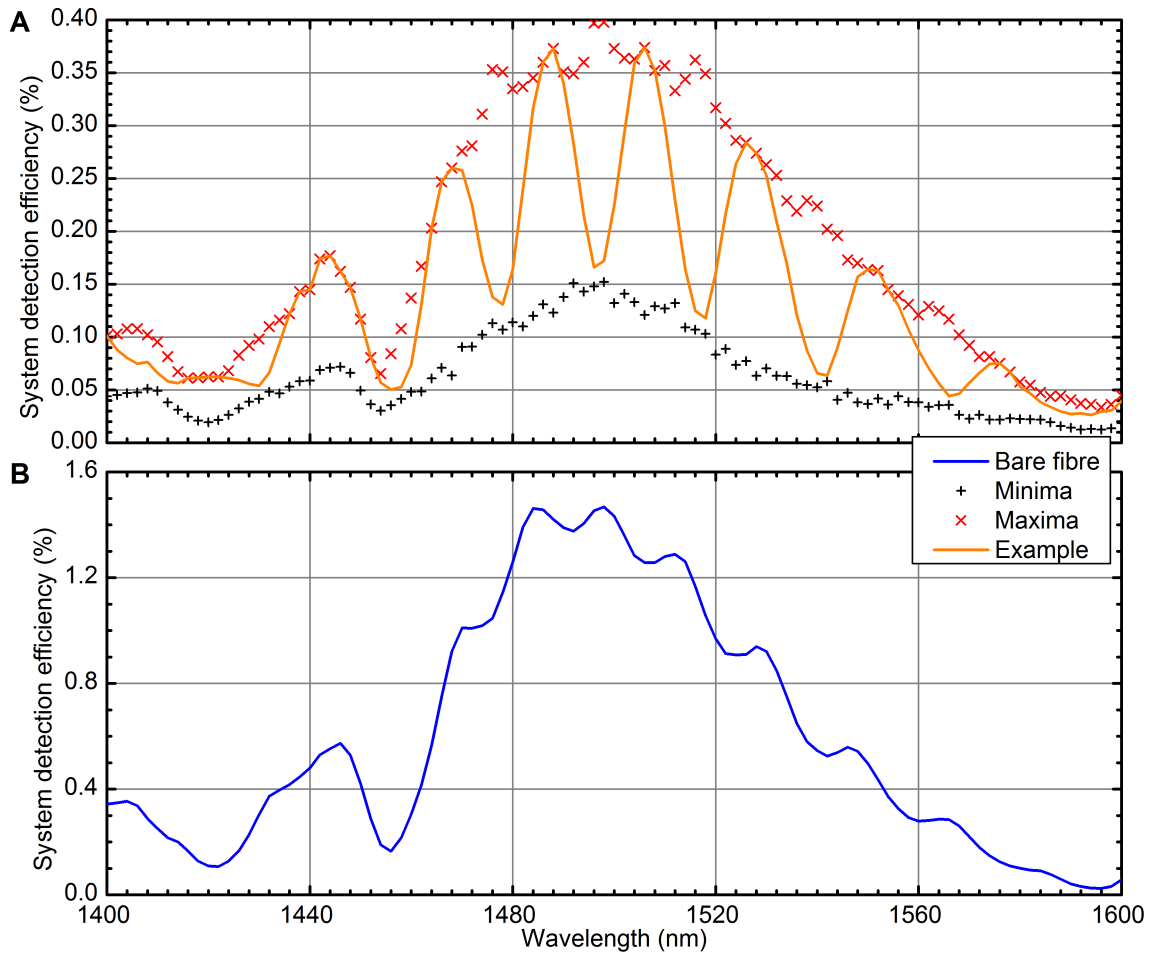


Figure 6.9: Graphs of SDE tuning range for Configuration II, shown in **A**, and comparison with bare fibre, shown in **B**. As with Configuration I data, the data are shown in separate graphs as they are not directly comparable. The bare fibre result shows a much higher SDE, but this is because (unlike for the Configuration I data) the cavity lengths are not matched. Worthy of note is that off-resonance, at 1550 nm, the tunable cavity offers the opportunity to select a cavity length and wavelength that increases the SDE.

that the SDE at 1550 nm is improved from 0.33 to 0.46 of the maximal SDE at 1500 nm, an improvement coincidentally also of 1.4 times.

## 6.5 Conclusion

It is clear that the overall effect of the tunable cavity is to take the effect of the common reflector structure that is widely employed[9, 64, 66, 110, 142, 143] and allow a degree of control over the wavelength at which the resonance occurs. From the results presented here for a simple reflector as demonstrated by Configuration I, this offers an SDE of 1.4 times the value obtained without a cavity, for incident photons of wavelength 1560 nm. Simulation suggests that the absorption should increase by about 1.64 times (from 60% to 99%). Considering that the experimental realisation has losses such as

reflections from the fibre-to-glue and glue-to-DBR boundary incorporated into the SDE that aren't accounted for when looking solely at the absorption, this is an encouraging result.

For the Configuration II SNSPD fabricated on a DBR reflector, at a wavelength of 1550 nm it also offers 1.4 times the SDE. This was determined by a different method to the Configuration I detector due to a peculiarity of the experiment preventing matching of cavity lengths. From simulation, an increase of around 2 would be expected: accounting for the same factors as Configuration I, and noting the challenges of perfect DBR fabrication that likely lead to a shift in features between simulation and experiment, that an improvement is seen remains important.

There is qualitative agreement between the features seen in the one-dimensional simulation of absorbed power into the nanowire and the experimental results. We do not expect to see identical responses, because the simulations do not consider the other factors that influence the SDE, such as the polarisation of the input light, and the  $\eta_{coupling}$  and  $\eta_{triggering}$  coefficients, which will vary.

State-of-the-art detector designs typically incorporate optical cavities[9, 142] to enhance performance at a target wavelength. However, these have a fixed cavity length. The proof-of-concept system used in this work is original in that its cavity length may be tuned as required[20]. Furthermore, this work represents the first cavity-embedded SNSPD in which both reflectors are DBRs.

In this work, the SDE of two SNSPDs was measured at a range of wavelengths and cavity spacings, using a bare fibre and using a DBR-coupled fibre. The response in both situations matched a one-dimensional simulation, and experimentally demonstrated tuning of the cavity resonance, and in turn an enhancement in the SDE at a photon wavelength of 1550 nm. The tight localisation of the field within a thin spatial zone could allow probing of ultrathin layers such as graphene and related two-dimensional materials, and the tunable nature of the cavity offers some mitigation of the imprecise nature of DBR fabrication.

# Chapter 7

## Conclusions

This chapter will summarise the individual conclusions of the three results chapters and the broader conclusions of the whole work. It will discuss the significance of the work, offer a critical analysis, and suggest future work that could improve on the results.

### 7.1 Summary and discussion of results

This work presents three nano-optical studies of very different phenomena: parallel-wire superconducting nanowire single photon detectors (SNSPDs) operating in one- and two-pixel trigger regimes, nanoantenna-coupled SNSPDs with enhanced local coupling, and SNSPDs in a distributed Bragg reflector (DBR) cavity with an enhanced absorption across the full detector.

There are several technical advancements presented in this thesis. This work developed the nano-optical system demonstrated in earlier work[83] by adapting it for low-vibration operation, and extending its operational wavelength range out to the limits imposed by single-mode fibre (SMF). The work further added the use of DBR fibre in place of a miniature confocal microscope, allowing the formation of a tunable cavity. From the results here presented, one may conclude that the nano-optical testing system is a robust and effective method of obtaining vital data on the performance of these SNSPDs.

#### 7.1.1 Spatially-resolvable parallel-wire SNSPDs

By employing the nano-optical testing setup to spatially-separate parallel-wire SNSPDs[18], this thesis presents an original, explicit demonstration of the arm-trigger regime for parallel-wire devices, and that when operating exclusively in this regime the detector retains its fast timing properties. It develops a statistical model to describe the

behaviour. The work specifically shows that the particular parallel-wire detector under test may be biased such that it can trigger when illuminating a single pixel with  $\eta = 7.5 \times 10^{-4}$  or when illuminating two pixels with  $\eta = 1.59 \times 10^{-4}$ .

Independent of this work, readout schemes for true multi-element SNSPDs have been demonstrated[78, 79]. These remove the exploitable effect of multi-pixel discrimination, at the expense of a more complex fabrication process, and more demanding hardware requirements for reading the output, but offer true photon number resolution (PNR).

Despite multi-element SNSPDs developed elsewhere, work on multi-pixel detectors with a single readout remains important and relevant: high-efficiency, packaged detectors comprised of two stacked pixels have been demonstrated[146] that would benefit from the mathematical description if operating in the arm-trigger regime.

### 7.1.2 Nanoantenna-coupled SNSPDs

The nano-optical study of the nanoantenna-coupled SNSPD shows strong evidence that there is a significant enhancement in the absorption into the nanowire. This appears as an increased count rate at the spatial location of the antennas tested, and peaks near their respective design wavelengths. This is further supported by three-dimensional finite difference time domain (FDTD) simulation of the system, which qualitatively agrees with the result. The increase in system detection efficiency (SDE) when measuring over the antenna is, at the best electric field polarisation, 130 % higher than when measuring over bare wire.

The FDTD simulation of the nanoantenna-coupled detectors suggests a resonance which agrees with what is observed experimentally. However, the simulated resonance is more broad than is observed, and the simulation does not describe the smaller oscillations, likely from cavity effects, seen in the result. Furthermore, the response with polarisation when illuminating a bare wire (blue data in figure 5.3) disagrees with what we expect from the response by showing a crossing in the power absorption with electric field polarisation. This is also not experimentally observed. These are limitations of the simulation that could be improved upon.

The nanoantenna-coupled SNSPD successfully simulated, fabricated, and comprehensively characterised in this work at telecoms wavelengths more than doubles the efficiency of the detector, and offers a potential route to lower fill-factor devices. It could in principle be extended to mid-infra-red (IR) wavelengths, to allow efficient operation when photon energies are lower.

### 7.1.3 Tunable-cavity embedded SNSPDs

Using the DBR-coupled fibre with detectors fabricated with a reflector, this work demonstrates cavity tuning, and that it matches with simulation. For a detector in a cavity formed with a simple reflector, an enhancement in the SDE of 40 % is observed at 1560 nm. For a detector in a cavity formed with a DBR reflector, an enhancement of 40 % in SDE is observed at 1550 nm, though due to the peculiarities of fabrication the resonance of the DBR is around 1510 nm.

Increasing photon absorption into a nanowire is important, and will hopefully prove useful throughout the field. However, for the high-efficiency SNSPDs that have been demonstrated elsewhere, there is already a high  $\eta_{absorption}$ . These high-efficiency detectors require a more demanding cooling regime, operating best at mK temperatures. This is relatively non-trivial, requiring complex refrigeration technology which is not practical in end-user applications, so there is still room for this work for systems operating in Gifford-McMahon (GM) and pulse tube cryostats at around 3 K.

The current generation of high-efficiency SNSPDs exploit cavity or reflector behaviour[9]. By adding a tunable parameter, as the system used in this experiment shows, a degree of control over the wavelength of the resonance is afforded. Both detectors tested in the experiment when tuned showed an increase in their SDE.

## 7.2 Parallel developments in group

The nano-optical system presented in this work has been employed in other studies by the research group, most notably by Dr Alessandro Casaburi for work on superconducting strip-line detectors (SSLDs)[139, 147, 148]. It would be imprudent to go into too much detail on this work in a thesis about SNSPDs, but the role of the nano-optical system developed for use with SNSPDs was a core component of the work.

In addition to this, the system is presently being used by group member Robert Kirkwood as a means of easily and efficiently coupling light into waveguide circuits.

## 7.3 Outlook

Taking the work presented herein forward, an obvious goal being pursued by the Quantum Sensors group as well as others worldwide is scaling up single-pixel detectors to multi-pixel arrays. There have been several key developments in this field[77–79] that will enable this.

Extending the use of SNSPDs into mid-IR is also of interest to the photon detection community. The operation of SNSPDs at these wavelengths has been demonstrated[48], but at relatively low efficiency. This could be enhanced by using nanoantennas resonant at the wavelength of interest to focus long-wavelength photons down to a nanowire, or by using a specially-designed tunable cavity. Any work at mid-IR would come with challenges in delivery of the light to the SNSPD however, as research into and commercial components for this wavelength band are relatively new in comparison with work at 1550 nm.

# Appendix A

## List of Publications

- R. M. Heath, M. G. Tanner, T. D. Drysdale, S. Miki, V. Giannini, S. A. Maier, and R. H. Hadfield. Nanoantenna enhancement for telecom-wavelength superconducting single photon detector. *Nano Letters*, 15(2):819–822, 2015
- R. M. Heath, M. G. Tanner, A. Casaburi, M. G. Webster, L. San Emeterio Alvarez, W. Jiang, Z. H. Barber, R. J. Warburton, and R. H. Hadfield. Nano-optical observation of cascade switching in a parallel superconducting nanowire single photon detector. *Applied Physics Letters*, 104(6):063503, 2014
- A. Casaburi, R. M. Heath, M. G. Tanner, R. Cristiano, M. Ejrnaes, C. Nappi, and R.H. Hadfield. Current distribution in a parallel configuration superconducting strip-line detector. *Applied Physics Letters*, 103(1):013503–013503, 2013
- A. Casaburi, R. M. Heath, M. G. Tanner, R. Cristiano, M. Ejrnaes, C. Nappi, and R. H. Hadfield. Parallel superconducting strip-line detectors: reset behaviour in the single-strip switch regime. *Superconductor Science and Technology*, 27(4):044029, 2014
- A. Casaburi, R. M. Heath, M. Ejrnaes, C. Nappi, R. Cristiano, and R. H. Hadfield. Non-uniform meta-stable current redistribution in parallel superconducting strips operating in the single strip switch regime after equilibrium perturbation. 2014. In preparation
- M. G. Tanner, R. M. Heath, S. Miki, R. J. Warburton, and R. H. Hadfield. A fibre coupled tuneable optical cavity at telecommunications wavelength for enhanced detector absorption. 2014. In preparation

# List of References

- [1] A. Einstein. On a heuristic point of view concerning the production and transformation of light. *Annalen der Physik*, 17:132–148, 1905.
- [2] S. Hecht, S. Shlaer, and M. H. Pirenne. Energy, quanta, and vision. *The Journal of General Physiology*, 25(6):819–840, 1942.
- [3] European Commission Directorate-General for Health and Consumers. Scientific Committee on Emerging and Newly Identified Health Risks: Light Sensitivity. [http://ec.europa.eu/health/ph\\_risk/committees/04\\_scenihr/docs/scenihr\\_o\\_019.pdf](http://ec.europa.eu/health/ph_risk/committees/04_scenihr/docs/scenihr_o_019.pdf), 2008. Date accessed 11 August 2014.
- [4] S. M. Matz, G. H. Share, M. D. Leising, E. L. Chupp, W. T. Vestrandt, W. R. Purcell, M. S. Strickman, and C. Reppin. Gamma-ray line emission from SN1987A. *Nature*, 331:416–318, 1988.
- [5] S. Fukuda, Y. Fukuda, M. Ishitsuka, Y. Itow, T. Kajita, J. Kameda, K. Kaneyuki, K. Kobayashi, Y. Koshio, M. Miura, et al. Constraints on neutrino oscillations using 1258 days of Super-Kamiokande solar neutrino data. *Physical Review Letters*, 86(25):5656, 2001.
- [6] G. Pajares. Advances in sensors applied to agriculture and forestry. *Sensors*, 11(9):8930–8932, 2011.
- [7] W. C. Röntgen. Über eine neue art von strahlen. *Annalen der Physik*, 300(1):1–11, 1898.
- [8] J. L. O’Brien. Optical quantum computing. *Science*, 318(5856):1567, 2007.
- [9] F. Marsili, V. B. Verma, J. A. Stern, S. Harrington, A. E. Lita, T. Gerrits, I. Vayshenker, B. Baek, M. D. Shaw, R. P. Mirin, and S. W. Nam. Detecting single infrared photons with 93% system efficiency. *Nature Photonics*, 7(3):210–214, 2013.
- [10] A. Verevkin, A. Pearlman, W. Slysz, J. Zhang, M. Currier, A. Korneev, G. Chulkova, O. Okunev, P. Kouminov, K. Smirnov, et al. Ultrafast superconducting single-photon detectors for near-infrared-wavelength quantum communications. *Journal of Modern Optics*, 51(9):1447–1458, 2004.

- [11] A. Korneev, P. Kouminov, V. Matvienko, G. Chulkova, K. Smirnov, B. Voronov, G. N. Gol'tsman, M. Currie, W. Lo, K. Wilsher, et al. Sensitivity and gigahertz counting performance of NbN superconducting single-photon detectors. *Applied Physics Letters*, 84:5338, 2004.
- [12] W. H. P. Pernice, C. Schuck, O. Minaeva, M. Li, G. N. Gol'tsman, A. V. Sergienko, and H. X. Tang. High-speed and high-efficiency travelling wave single-photon detectors embedded in nanophotonic circuits. *Nature Communications*, 3:1325, 2012.
- [13] N. R. Gemmell, A. McCarthy, B. Liu, M. G. Tanner, S. N. Dorenbos, V. Zwiller, M. S. Patterson, G. S. Buller, B. C. Wilson, and R. H. Hadfield. Singlet oxygen luminescence detection with a fiber-coupled superconducting nanowire single-photon detector. *Optics Express*, 21(4):5005–5013, 2013.
- [14] D. Bonneau, M. Lobino, P. Jiang, C. M. Natarajan, M. G. Tanner, R. H. Hadfield, S. N. Dorenbos, V. Zwiller, M. G. Thompson, and J. L. O'Brien. Fast path and polarization manipulation of telecom wavelength single photons in lithium niobate waveguide devices. *Physical Review Letters*, 108(5):053601, 2012.
- [15] M. Sasaki, M. Fujiwara, H. Ishizuka, W. Klaus, K. Wakui, M. Takeoka, S. Miki, T. Yamashita, Z. Wang, A. Tanaka, et al. Field test of quantum key distribution in the Tokyo QKD Network. *Optics Express*, 19(11):10387–10409, 2011.
- [16] A. McCarthy, N. J. Krichel, N. R. Gemmell, X. Ren, M. G. Tanner, S. N. Dorenbos, V. Zwiller, R. H. Hadfield, and G. S. Buller. Kilometer-range, high resolution depth imaging via 1560 nm wavelength single-photon detection. *Optics Express*, 21(7):8904–8915, 2013.
- [17] J. A. O'Connor, M. G. Tanner, C. M. Natarajan, G. S. Buller, R. J. Warburton, S. Miki, Z. Wang, S. W. Nam, and R. H. Hadfield. Spatial dependence of output pulse delay in a niobium nitride nanowire superconducting single-photon detector. *Applied Physics Letters*, 98(20):201116, 2011.
- [18] R. M. Heath, M. G. Tanner, A. Casaburi, M. G. Webster, L. San Emeterio Alvarez, W. Jiang, Z. H. Barber, R. J. Warburton, and R. H. Hadfield. Nano-optical observation of cascade switching in a parallel superconducting nanowire single photon detector. *Applied Physics Letters*, 104(6):063503, 2014.
- [19] R. M. Heath, M. G. Tanner, T. D. Drysdale, S. Miki, V. Giannini, S. A. Maier, and R. H. Hadfield. Nanoantenna enhancement for telecom-wavelength superconducting single photon detector. *Nano Letters*, 15(2):819–822, 2015.

- [20] M. G. Tanner, R. M. Heath, S. Miki, R. J. Warburton, and R. H. Hadfield. A fibre coupled tuneable optical cavity at telecommunications wavelength for enhanced detector absorption. 2014. In preparation.
- [21] R. H. Hadfield. Single-photon detectors for optical quantum information applications. *Nature Photonics*, 3(12):696–705, 2009.
- [22] H. Iams and B. Salzberg. The secondary emission phototube. *Proceedings of the Institute of Radio Engineers*, 23(1):55–64, 1935.
- [23] V. K. Zworykin, G. A. Morton, and L. Malter. The secondary emission multiplier—a new electronic device. *Proceedings of the Institute of Radio Engineers*, 24(3):351–375, 1936.
- [24] Y. Fukuda, T. Hayakawa, E. Ichihara, K. Inoue, K. Ishihara, H. Ishino, Y. Itow, T. Kajita, J. Kameda, S. Kasuga, et al. Measurements of the solar neutrino flux from Super-Kamiokande’s first 300 days. *Physical Review Letters*, 81(6):1158–1162, 1998.
- [25] R. Foord, R. Jones, C. J. Oliver, and E. R. Pike. The use of photomultiplier tubes for photon counting. *Applied Optics*, 8(10):1975–1989, 1969.
- [26] H. Kume, K. Koyama, K. Nakatsugawa, S. Suzuki, and D. Fatlowitz. Ultrafast microchannel plate photomultipliers. *Applied Optics*, 27(6):1170–1178, 1988.
- [27] V. V. Anashin, P. M. Beschastnov, V. B. Golubev, L. A. Mironenko, A. A. Salnikov, and S. I. Serednyakov. Photomultipliers with microchannel plates. *Nuclear Instruments and Methods in Physics Research A*, 357:103–109, 1995.
- [28] J. S. Milnes and J. Howorth. Picosecond time response characteristics of microchannel plate PMT detectors. In *26th International Congress on High-Speed Photography and Photonics*, pages 730–740. International Society for Optics and Photonics, 2005.
- [29] S. Cova, A. Longoni, and A. Andreoni. Towards picosecond resolution with single-photon avalanche diodes. *Review of Scientific Instruments*, 52(3):408–412, 1981.
- [30] M. D. Eisaman, J. Fan, A. Migdall, and S. V. Polyakov. Invited review article: Single-photon sources and detectors. *Review of Scientific Instruments*, 82(7):071101, 2011.
- [31] R. G. W. Brown, R. Jones, J. G. Rarity, and K. D. Ridley. Characterization of silicon avalanche photodiodes for photon correlation measurements. 2: Active quenching. *Applied Optics*, 26(12):2383–2389, 1987.

- [32] S. Cova, A. Lacaita, M. Ghioni, G. Ripamonti, and T. A. Louis. 20-ps timing resolution with single-photon avalanche diodes. *Review of Scientific Instruments*, 60(6):1104–1110, 1989.
- [33] R. Ramaswami. Optical fiber communication: from transmission to networking. *Communications Magazine, IEEE*, 40(5):138–147, 2002.
- [34] B. G. Streetman and S. Banerjee. *Solid State Electronic Devices*. Prentice Hall, 2000.
- [35] S. Cova, A. Lacaita, and G. Ripamonti. Trapping phenomena in avalanche photodiodes on nanosecond scale. *Electron Device Letters, IEEE*, 12(12):685–687, 1991.
- [36] H. K. Onnes. The superconductivity of mercury. *Comm. Phys. Lab. Univ. Leiden*, 122:124, 1911.
- [37] V. L. Ginzburg and L. D. Landau. On the theory of superconductivity. *Zhurnal Eksperimental'noi i Teoreticheskoi Fiziki*, 20:1064, 1950.
- [38] A. A. Abrikosov. Theoretical prediction of vortices in type-II superconductors. *Zhurnal Eksperimental'noi i Teoreticheskoi Fiziki*, 32:1442, 1957.
- [39] J. Bardeen, L. N. Cooper, and J. R. Schrieffer. Theory of superconductivity. *Physical Review*, 108(5):1175, 1957.
- [40] P. A. Tipler and G. Mosca. *Physics for Scientists and Engineers*. W.H. Freeman and Company, fifth edition, 2004.
- [41] C. P. Poole Jr, H. A. Farach, R. J. Creswick, and R. Prozorov. *Superconductivity*. Academic Press, 2007.
- [42] A. Peacock, P. Verhoeve, N. Rando, A. Van Dordrecht, B. G. Taylor, C. Erd, M. A. C. Perryman, R. Venn, J. Howlett, D. J. Goldie, et al. Single optical photon detection with a superconducting tunnel junction. *Nature*, 381:135, 1996.
- [43] B. Cabrera, R. M. Clarke, P. Colling, A. J. Miller, S. Nam, and R. W. Romani. Detection of single infrared, optical, and ultraviolet photons using superconducting transition edge sensors. *Applied Physics Letters*, 73:735, 1998.
- [44] A. J. Miller, S. W. Nam, J. M. Martinis, and A. V. Sergienko. Demonstration of a low-noise near-infrared photon counter with multiphoton discrimination. *Applied Physics Letters*, 83:791, 2003.
- [45] G. N. Gol'tsman, O. Okunev, G. Chulkova, A. Lipatov, A. Semenov, K. Smirnov, B. Voronov, A. Dzardanov, C. Williams, and R. Sobolewski. Picosecond superconducting single-photon optical detector. *Applied Physics Letters*, 79:705, 2001.

- [46] M. J. Stevens, R. H. Hadfield, R. E. Schwall, S. W. Nam, R. P. Mirin, and J. A. Gupta. Fast lifetime measurements of infrared emitters using a low-jitter superconducting single-photon detector. *Applied Physics Letters*, 89(3):031109–031109, 2006.
- [47] A. D. Semenov, G. N. Gol'tsman, and A. A. Korneev. Quantum detection by current carrying superconducting film. *Physica C: Superconductivity*, 351(4):349–356, 2001.
- [48] F. Marsili, F. Bellei, F. Najafi, A. E. Dane, E. A. Dauler, R. J. Molnar, and K. K. Berggren. Efficient single photon detection from 500 nm to 5  $\mu$ m wavelength. *Nano letters*, 12(9):4799–4804, 2012.
- [49] Hamamatsu Photonics. NIR-Photomultiplier Tubes And Their Applications. [http://www.hamamatsu.com/resources/pdf/etd/NIR-PMT\\_APPLI\\_TPM01040E.pdf](http://www.hamamatsu.com/resources/pdf/etd/NIR-PMT_APPLI_TPM01040E.pdf). Date accessed 6 February 2015.
- [50] M. Liu, C. Hu, . Bai, X. Guo, J. C. Campbell, Z. Pan, and M. M. Tashima. High-performance InGaAs/InP single-photon avalanche photodiode. *Selected Topics in Quantum Electronics, IEEE Journal of*, 13(4):887–894, 2007.
- [51] A. Restelli, J. C. Bienfang, and A. L. Migdall. Single-photon detection efficiency up to 50% at 1310 nm with an InGaAs/InP avalanche diode gated at 1.25 GHz. *Applied Physics Letters*, 102(14):141104, 2013.
- [52] J. C. Campbell, W. Sun, Z. Lu, M. A. Itzler, and X. Jiang. Common-mode cancellation in sinusoidal gating with balanced InGaAs/InP single photon avalanche diodes. *Quantum Electronics, IEEE Journal of*, 48(12):1505–1511, 2012.
- [53] A. E. Lita, A. J. Miller, and S. W. Nam. Counting near-infrared single-photons with 95% efficiency. *Optics Express*, 16(5):3032–3040, 2008.
- [54] D. Fukuda, G. Fujii, T. Numata, A. Yoshizawa, H. Tsuchida, S. Inoue, and T. Zama. Titanium TES based photon number resolving detectors with 1 MHz counting rate and 65% quantum efficiency. In *SPIE OPTO: Integrated Optoelectronic Devices*, pages 72360C–72360C. International Society for Optics and Photonics, 2009.
- [55] D. Fukuda, G. Fujii, T. Numata, A. Yoshizawa, H. Tsuchida, H. Fujino, H. Ishii, T. Itatani, S. Inoue, and T. Zama. Photon number resolving detection with high speed and high quantum efficiency. *Metrologia*, 46(4):S288, 2009.
- [56] A. Pearlman, A. Cross, W. Slysz, J. Zhang, A. Verevkin, M. Currie, A. Korneev, P. Kouminov, K. Smirnov, B. Voronov, G. Gol'tsman, and R. Sobolewski.

- Gigahertz counting rates of NbN single-photon detectors for quantum communications. *Applied Superconductivity, IEEE Transactions on*, 15(2):579–582, 2005.
- [57] J. K. W. Yang, A. J. Kerman, E. A. Dauler, V. Anant, K. M. Rosfjord, and K. K. Berggren. Modeling the electrical and thermal response of superconducting nanowire single-photon detectors. *Applied Superconductivity, IEEE Transactions on*, 17(2):581–585, 2007.
- [58] S. Miki, M. Fujiwara, M. Sasaki, B. Baek, A. J. Miller, R. H. Hadfield, S. W. Nam, and Z. Wang. Large sensitive-area NbN nanowire superconducting single-photon detectors fabricated on single-crystal MgO substrates. *Applied Physics Letters*, 92:061116, 2008.
- [59] F. Marsili, D. Bitauld, A. Fiore, A. Gaggero, F. Mattioli, R. Leoni, M. Benkhouh, and F. Lévy. High efficiency NbN nanowire superconducting single photon detectors fabricated on MgO substrates from a low temperature process. *Optics Express*, 16(5):3191–3196, 2008.
- [60] F. Marsili, A. Gaggero, L. H. Li, A. Surrente, R. Leoni, F. Lévy, and A. Fiore. High quality superconducting NbN thin films on GaAs. *Superconductor Science and Technology*, 22:095013, 2009.
- [61] J. A. Stern and W. H. Farr. Fabrication and characterization of superconducting NbN nanowire single photon detectors. *Applied Superconductivity, IEEE Transactions on*, 17(2):306–309, 2007.
- [62] M. G. Tanner, L. San Emeterio Alvarez, W. Jiang, R. J. Warburton, Z. H. Barber, and R. H. Hadfield. A superconducting nanowire single photon detector on lithium niobate. *Nanotechnology*, 23(50):505201, 2012.
- [63] S. N. Dorenbos, E. M. Reiger, U. Perinetti, V. Zwiller, T. Zijlstra, and T. M. Klapwijk. Low noise superconducting single photon detectors on silicon. *Applied Physics Letters*, 93(13):131101, 2008.
- [64] M. G. Tanner, C. M. Natarajan, V. K. Pottapenjana, J. A. O’Connor, R. J. Warburton, R. H. Hadfield, B. Baek, S. W. Nam, S. N. Dorenbos, E. B. Ureña, et al. Enhanced telecom wavelength single-photon detection with NbTiN superconducting nanowires on oxidized silicon. *Applied Physics Letters*, 96:221109, 2010.
- [65] A. Verevkin, J. Zhang, R. Sobolewski, A. Lipatov, O. Okunev, G. Chulkova, A. Korneev, K. Smirnov, G. N. Gol’tsman, and A. Semenov. Detection efficiency of large-active-area NbN single-photon superconducting detectors in the ultraviolet to near-infrared range. *Applied Physics Letters*, 80:4687, 2002.

- [66] K. M. Rosfjord, J. K. W. Yang, E. A. Dauler, A. J. Kerman, V. Anant, B. M. Voronov, G. N. Gol'tsman, and K. K. Berggren. Nanowire single-photon detector with an integrated optical cavity and anti-reflection coating. *Optics Express*, 14(2):527–534, 2006.
- [67] V. Anant, A. J. Kerman, E. A. Dauler, J. K. W. Yang, K. M. Rosfjord, and K. K. Berggren. Optical properties of superconducting nanowire single-photon detectors. *Optics Express*, 16:10750–10761, 2008.
- [68] S. N. Dorenbos, E. M. Reiger, N. Akopian, U. Perinetti, V. Zwiller, T. Zijlstra, and T. M. Klapwijk. Superconducting single photon detectors with minimized polarization dependence. *Applied Physics Letters*, 93:161102, 2008.
- [69] A. J. Kerman, E. A. Dauler, W. E. Keicher, J. K. W. Yang, K. K. Berggren, G. N. Gol'tsman, and B. Voronov. Kinetic-inductance-limited reset time of superconducting nanowire photon counters. *Applied Physics Letters*, 88:111116, 2006.
- [70] A. J. Kerman, E. A. Dauler, J. K. W. Yang, K. M. Rosfjord, V. Anant, K. K. Berggren, G. N. Gol'tsman, and B. M. Voronov. Constriction-limited detection efficiency of superconducting nanowire single-photon detectors. *Applied Physics Letters*, 90(10):101110–101110, 2007.
- [71] R. H. Hadfield, P. A. Dalgarno, J. A. O'Connor, E. Ramsay, R. J. Warburton, E. J. Gansen, B. Baek, M. J. Stevens, R. P. Mirin, and S. W. Nam. Submicrometer photoresponse mapping of nanowire superconducting single-photon detectors. *Applied Physics Letters*, 91:241108, 2007.
- [72] F. Marsili, F. Najafi, C. Herder, and K. K. Berggren. Electrothermal simulation of superconducting nanowire avalanche photodetectors. *Applied Physics Letters*, 98(9):093507–093507, 2011.
- [73] M. Ejrnaes, R. Cristiano, O. Quaranta, S. Pagano, A. Gaggero, F. Mattioli, R. Leoni, B. Voronov, and G. N. Gol'tsman. A cascade switching superconducting single photon detector. *Applied Physics Letters*, 91:262509, 2007.
- [74] F. Marsili, F. Najafi, E. Dauler, F. Bellei, X. Hu, M. Csete, R. J. Molnar, and K. K. Berggren. Single-photon detectors based on ultranarrow superconducting nanowires. *Nano Letters*, 11(5):2048–2053, 2010.
- [75] A. Divochiy, F. Marsili, D. Bitauld, A. Gaggero, R. Leoni, F. Mattioli, A. Korneev, V. Seleznev, N. Kaurova, O. Minaeva, G. N. Gol'tsman, K. G. Lagoudakis, M. Benkhaoul, F. Lévy, and A. Fiore. Superconducting nanowire photon-number-resolving detector at telecommunication wavelengths. *Nature Photonics*, 2(5):302–306, 2008.

- [76] E. A. Dauler, B. S. Robinson, A. J. Kerman, J. K. W. Yang, K. M. Rosfjord, V. Anant, B. Voronov, G. N. Gol'tsman, and K. K. Berggren. Multi-element superconducting nanowire single-photon detector. *Applied Superconductivity, IEEE Transactions on*, 17(2):279–284, 2007.
- [77] S. Miki, T. Yamashita, Z. Wang, and H. Terai. A 64-pixel NbTiN superconducting nanowire single-photon detector array for spatially resolved photon detection. *Optics Express*, 22(7):7811–7820, 2014.
- [78] V. B. Verma, R. Horansky, F. Marsili, J. A. Stern, M. D. Shaw, A. E. Lita, R. P. Mirin, and S. W. Nam. A four-pixel single-photon pulse-position array fabricated from wsi superconducting nanowire single-photon detectors. *Applied Physics Letters*, 104(5):051115, 2014.
- [79] T. Yamashita, S. Miki, H. Terai, K. Makise, and Z. Wang. Crosstalk-free operation of multielement superconducting nanowire single-photon detector array integrated with single-flux-quantum circuit in a 0.1 W Gifford–McMahon cryocooler. *Optics Letters*, 37(14):2982–2984, 2012.
- [80] J. Wilks. *The Third Law of Thermodynamics*. Oxford University Press, 1961.
- [81] W. M. Haynes. *CRC Handbook of Chemistry and Physics*. CRC Press, 2011.
- [82] Z. Wang, A. Kawakami, Y. Uzawa, and B. Komiyama. Superconducting properties and crystal structures of single-crystal niobium nitride thin films deposited at ambient substrate temperature. *Journal of Applied Physics*, 79(10):7837–7842, 1996.
- [83] J. A. O'Connor. *Nano-Optical Studies of Superconducting Nanowire Single Photon Detectors*. PhD thesis, Heriot-Watt University, 2011.
- [84] A. C. Kirk. On the mechanical production of cold. In *Minutes of the Proceedings*, volume 37, pages 244–282, 1874.
- [85] R. Radebaugh. Development of the pulse tube refrigerator as an efficient and reliable cryocooler. *Proc. Institute of Refrigeration, London*, 2000.
- [86] M. D. Atrey. IIT Bombay Department of Mechanical Engineering Cryogenic Engineering lecture notes L27 - Cryocoolers. [http://nptel.ac.in/courses/112101004/downloads/\(27-6-2\)%20NPTEL%20-%20Cryocoolers.pdf](http://nptel.ac.in/courses/112101004/downloads/(27-6-2)%20NPTEL%20-%20Cryocoolers.pdf). Date accessed 18 August 2014.
- [87] A. T. A. M. De Waele. Basic operation of cryocoolers and related thermal machines. *Journal of low temperature physics*, 164(5-6):179–236, 2011.
- [88] H. O. McMahon and W. E. Gifford. A new low-temperature gas expansion cycle. In *Advances in Cryogenic Engineering*, pages 354–367. Springer, 1960.

- [89] C. M. Natarajan. *Superconducting nanowire single-photon detectors for advanced photon-counting applications*. PhD thesis, Heriot-Watt University, 2011.
- [90] E. I. Mikulin, A. A. Tarasov, and M. P. Shkrebyonock. *Low-temperature expansion pulse tubes*, pages 629–637. Springer, 1984.
- [91] J. M. Pfotenhauer. University of Wisconsin Madison U.S. Particle Accelerator School Principles of Cryogenic Engineering lecture notes 2.2 - Cryocoolers. [http://uspas.fnal.gov/materials/10MIT/Lecture\\_2.2.pdf](http://uspas.fnal.gov/materials/10MIT/Lecture_2.2.pdf). Date accessed 19 August 2014.
- [92] CryoMech. PT403 data sheet. <http://www.cryomech.com/CRYOREFRIGERATORS/PT403/PT403%20Specification%20Sheet.pdf>. Date accessed 30 May 2011.
- [93] Cryomech. Cryogenic refrigerator installation, operation and routine maintenance manual. [http://www.qd-china.com/download/cryomech/PT403\\_Manual.pdf](http://www.qd-china.com/download/cryomech/PT403_Manual.pdf). Date accessed 18 August 2014.
- [94] Pfeiffer Vacuum. *The Vacuum Technology Book Volume II: Know-how Book*. Pfeiffer Vacuum GmbH, 2013.
- [95] Umrath, W. *Fundamentals of Vacuum Technology*. Leybold Vacuum, 2001.
- [96] Adixen. ATP series turbomolecular pump manual. [http://www.idealvac.com/files/manualsII/Alcatel\\_ATP\\_Turbo\\_Pumps\\_Users\\_Manual.pdf](http://www.idealvac.com/files/manualsII/Alcatel_ATP_Turbo_Pumps_Users_Manual.pdf). Date accessed 16 October 2014.
- [97] Adixen. ACP15/28/40 Series 2 primary dry pumps manual. [http://www.idealvac.com/files/brochures/AdixenACP\\_InstructionManual.pdf](http://www.idealvac.com/files/brochures/AdixenACP_InstructionManual.pdf). Date accessed 16 October 2014.
- [98] Oliver Benson. Elements of Nanophotonics lecture notes. <https://www.physik.hu-berlin.de/nano/lehre/Gastvorlesung%20Wien/plasmonics>. Date accessed 22 October 2014.
- [99] Maier, S. *Plasmonics: Fundamentals and Applications*. Springer, 2007.
- [100] P. Biagioni, J-S. Huang, and B. Hecht. Nanoantennas for visible and infrared radiation. *Reports on Progress in Physics*, 75(2):024402, 2012.
- [101] J. Aizpurua, G. W. Bryant, L. J. Richter, F. J. García de Abajo, B. K. Kelley, and T. Mallouk. Optical properties of coupled metallic nanorods for field-enhanced spectroscopy. *Physical Review B*, 71(23):235420, 2005.
- [102] L. Novotny and N. Van Hulst. Antennas for light. *Nature Photonics*, 5(2):83–90, 2011.

- [103] L. Tang, S. E. Kocabas, S. Latif, A. K. Okyay, D. S. Ly-Gagnon, K. C. Saraswat, and D. A. B. Miller. Nanometre-scale germanium photodetector enhanced by a near-infrared dipole antenna. *Nature Photonics*, 2(4):226–229, 2008.
- [104] X. Hu, E. A. Dauler, R. J. Molnar, and K. K. Berggren. Superconducting nanowire single-photon detectors integrated with optical nano-antennae. *Optics Express*, 19(1):17–31, 2011.
- [105] M. Csete, A. Sipos, A. Szalai, F. Najafi, G. Szabó, and K. K. Berggren. Improvement of infrared single-photon detectors absorptance by integrated plasmonic structures. *Scientific Reports*, 3, 2013.
- [106] R. Heeres. *Quantum Plasmonics*. PhD thesis, Technische Universiteit Delft, 2012.
- [107] J. B. Schneider. Understanding the Finite-Difference Time-Domain Method. [www.eecs.wsu.edu/~schneidj/ufdtd](http://www.eecs.wsu.edu/~schneidj/ufdtd), 2010. Date accessed 7 November 2014.
- [108] E. Hecht. *Optics*. Addison Wesley, 2002.
- [109] C. J. R. Sheppard. Approximate calculation of the reflection coefficient from a stratified medium. *Pure and Applied Optics: Journal of the European Optical Society Part A*, 4(5):665, 1995.
- [110] A. Gaggero, S. Jahanmiri Nejad, F. Marsili, F. Mattioli, R. Leoni, D. Bitauld, D. Sahin, G.J. Hamhuis, R. Nötzel, R. Sanjines, and A. Fiore. Nanowire superconducting single-photon detectors on GaAs for integrated quantum photonic applications. *Applied Physics Letters*, 97(15):151108, 2010.
- [111] S. Miki, M. Fujiwara, M. Sasaki, and Z. Wang. NbN superconducting single-photon detectors prepared on single-crystal MgO substrates. *IEEE Transactions on Applied Superconductivity*, 17(2):285–288, 2007.
- [112] S. K. Mehta, R. Muralidharan, G. D. Sharda, and R. K. Jain. Some investigations on oval defects in MBE-grown GaAs. *Semiconductor science and technology*, 7(5):635, 1992.
- [113] J. Sapriel, J. Chavignon, and F. Alexandre. Oval defects in  $\text{Ga}_{1-x}\text{Al}_x\text{As}$  molecular beam epitaxy layers: A Raman scattering and photoluminescence combined study. *Applied Physics Letters*, 52(23):1970–1972, 1988.
- [114] Harry Nyquist. Thermal agitation of electric charge in conductors. *Physical Review*, 32(1):110–113, 1928.
- [115] M. Härtig. Optical fibre alignment for superconducting nanowire single-photon detectors. Master’s thesis, Heriot-Watt University, 2008.

- [116] M. Ejrnaes, A. Casaburi, R. Cristiano, O. Quaranta, S. Marchetti, N. Martucciello, S. Pagano, A. Gaggero, F. Mattioli, R. Leoni, P. Cavalier, and J. C. Villégier. Timing jitter of cascade switch superconducting nanowire single photon detectors. *Applied Physics Letters*, 95(13):132503–132503, 2009.
- [117] F. Najafi, F. Marsili, E. Dauler, R. J. Molnar, and K. K. Berggren. Timing performance of 30-nm-wide superconducting nanowire avalanche photodetectors. *Applied Physics Letters*, 100(15):152602–152602, 2012.
- [118] PicoQuant. PicoHarp 300 data sheet. [http://www.picoquant.com/datasheets/photon\\_counting/PicoHarp300.pdf](http://www.picoquant.com/datasheets/photon_counting/PicoHarp300.pdf). Date accessed 30 May 2011.
- [119] PicoQuant. HydraHarp 400 data sheet. <http://www.picoquant.com/images/uploads/downloads/hydrharp400.pdf>. Date accessed 24 August 2014.
- [120] Kphotonics. Kphotonics CNT-1550-TK series datasheet. <http://www.kphotonics.com/turn-key-femtosecond-fiber-laser.html>. Date accessed 14 August 2014.
- [121] Attocube systems. ANSxy100 data sheet. [http://www.attocube.com/nanoPOSITIONING/ANSxy100/Specifications\\_ANSxy100.pdf](http://www.attocube.com/nanoPOSITIONING/ANSxy100/Specifications_ANSxy100.pdf). Date accessed 16 May 2011.
- [122] Thorlabs. Geltech 352280-C catalogue page. <http://www.thorlabs.de/catalogpages/V21/731.PDF>. Date accessed 15 August 2014.
- [123] Thorlabs. Geltech 352330-C catalogue page. <http://www.thorlabs.de/catalogpages/V21/720.PDF>. Date accessed 15 August 2014.
- [124] Epoxy Technology, Inc. EPO-TEK 301-2 technical data sheet. [http://www.epotek.com/site/administrator/components/com\\_products/assets/files/Style\\_Uploads/301-2.pdf](http://www.epotek.com/site/administrator/components/com_products/assets/files/Style_Uploads/301-2.pdf). Date accessed 25 July 2014.
- [125] Epoxy Technology, Inc. Understanding Optical Properties for Epoxy Applications. <http://www.epotek.com/site/files/Techtips/pdfs/tip18.pdf>. Date accessed 25 July 2014.
- [126] M. Bass, C. DeCusatis, J. Enoch, V. Lakshminarayanan, G. Li, C. MacDonald, V. Mahajan, and E. Van Stryland. *Handbook of Optics*, volume 4. McGraw Hill Professional, 3 edition, 2009.
- [127] B. Agdur, G. Böling, F. Sellberg, and Y. Öhman. Scattering, Absorption, and Emission of Light by Thin Metal Wires. *Physical Review*, 130(3):996, 1963.
- [128] Hewlett Packard. HP8167B/8D/8E/8F Tunable Laser Source User’s Guide. [http://www.equipland.com/objects/catalog/product/extras/1292\\_8167B%208D%208E%208F.pdf](http://www.equipland.com/objects/catalog/product/extras/1292_8167B%208D%208E%208F.pdf). Date accessed 15 August 2014.

- [129] Yenista. OSICS ECL - External Cavity Tunable Laser Source Module data sheet. [http://www.polytec.com/fileadmin/user\\_uploads/Products/LWL-Messgeraete/Optische\\_Telekommunikation/Documents/PH\\_FT\\_YEN\\_Osics%20ECL.pdf](http://www.polytec.com/fileadmin/user_uploads/Products/LWL-Messgeraete/Optische_Telekommunikation/Documents/PH_FT_YEN_Osics%20ECL.pdf). Date accessed 15 August 2014.
- [130] Yenista. OSICS T100 Tunable Laser Module data sheet. [http://yenista.com/IMG/pdf/OSICS-T100\\_DS\\_3-0v2-0.pdf](http://yenista.com/IMG/pdf/OSICS-T100_DS_3-0v2-0.pdf). Date accessed 15 August 2014.
- [131] Thorlabs. Single mode fiber SMF-28 specification sheet. <http://www.thorlabs.de/thorcat/2200/SMF-28-100-SpecSheet.pdf>. Date accessed 15 September 2014.
- [132] C. M. Natarajan, M. G. Tanner, and R. H. Hadfield. Superconducting nanowire single-photon detectors: physics and applications. *Superconductor Science and Technology*, 25(6):063001, 2012.
- [133] B. S. Robinson, A. J. Kerman, E. A. Dauler, R. J. Barron, D. O. Caplan, M. L. Stevens, J. J. Carney, S. A. Hamilton, J. K. Yang, and K. K. Berggren. 781 Mbit/s photon-counting optical communications using a superconducting nanowire detector. *Optics Letters*, 31(4):444–446, 2006.
- [134] M. G. Tanner, S. D. Dyer, B. Baek, R. H. Hadfield, and S. W. Nam. High-resolution single-mode fiber-optic distributed Raman sensor for absolute temperature measurement using superconducting nanowire single-photon detectors. *Applied Physics Letters*, 99(20):201110, 2011.
- [135] N. Gisin, G. Ribordy, W. Tittel, and H. Zbinden. Quantum cryptography. *Reviews of Modern Physics*, 74(1):145–195, 2002.
- [136] D. Sahin, A. Gaggero, Z. Zhou, S. Jahanmirinejad, F. Mattioli, R. Leoni, J. Beetz, M. Lermer, M. Kamp, S. Höfling, and A. Fiore. Waveguide photon-number-resolving detectors for quantum photonic integrated circuits. *Applied Physics Letters*, 103:111116, 2013.
- [137] M. Ejrnaes, A. Casaburi, R. Cristiano, N. Martucciello, F. Mattioli, A. Gaggero, R. Leoni, J. C. Villégier, and S. Pagano. Characterization of superconducting pulse discriminators based on parallel NbN nanostriplines. *Superconductor Science and Technology*, 24:035018, 2011.
- [138] D. Bitauld, F. Marsili, A. Gaggero, F. Mattioli, R. Leoni, S. J. Nejad, F. Lévy, and A. Fiore. Nanoscale optical detector with single-photon and multiphoton sensitivity. *Nano Letters*, 10(8):2977–2981, 2010.

- [139] A. Casaburi, R. M. Heath, M. G. Tanner, R. Cristiano, M. Ejrnaes, C. Nappi, and R.H. Hadfield. Current distribution in a parallel configuration superconducting strip-line detector. *Applied Physics Letters*, 103(1):013503–013503, 2013.
- [140] B. Baek, A. E. Lita, V. B. Verma, and S. W. Nam. Superconducting a-wxsi1- x nanowire single-photon detector with saturated internal quantum efficiency from visible to 1850 nm. *Applied Physics Letters*, 98(25):251105, 2011.
- [141] Y. Korneeva, I. Florya, A. Semenov, A. Korneev, and G. N. Gol'tsman. New generation of nanowire NbN superconducting single-photon detector for mid-infrared. *Applied Superconductivity, IEEE Transactions on*, 21(3):323–326, 2011.
- [142] S. Miki, T. Yamashita, H. Terai, and Z. Wang. High performance fiber-coupled NbTiN superconducting nanowire single photon detectors with gifford-mcmahon cryocooler. *Optics Express*, 21(8):10208–10214, 2013.
- [143] S. Miki, M. Takeda, M. Fujiwara, M. Sasaki, and Z. Wang. Compactly packaged superconducting nanowire single-photon detector with an optical cavity for multichannel system. *Optics Express*, 17(26):23557–23564, 2009.
- [144] S. N. Dorenbos, P. Forn-Diaz, T. Fuse, A. H. Verbruggen, T. Zijlstra, T. M. Klapwijk, and V. Zwiller. Low gap superconducting single photon detectors for infrared sensitivity. *Applied Physics Letters*, 98(25):251102, 2011.
- [145] M. K. Akhlaghi, H. Atikian, J. F. Young, M. Loncar, and A. H. Majedi. Efficient single photon absorption by optimized superconducting nanowire geometries. In *Proc. 13th Numerical Simulation of Optoelectronic Devices (NUSOD 2013)*. IEEE, 2013.
- [146] V. B. Verma, F. Marsili, S. Harrington, A. E. Lita, R. P. Mirin, and S. W. Nam. A three-dimensional, polarization-insensitive superconducting nanowire avalanche photodetector. *Applied Physics Letters*, 101(25):251114, 2012.
- [147] A. Casaburi, R. M. Heath, M. G. Tanner, R. Cristiano, M. Ejrnaes, C. Nappi, and R. H. Hadfield. Parallel superconducting strip-line detectors: reset behaviour in the single-strip switch regime. *Superconductor Science and Technology*, 27(4):044029, 2014.
- [148] A. Casaburi, R. M. Heath, M. Ejrnaes, C. Nappi, R. Cristiano, and R. H. Hadfield. Non-uniform meta-stable current redistribution in parallel superconducting strips operating in the single strip switch regime after equilibrium perturbation. 2014. In preparation.